Desiccation Cracking Behavior of Sustainable and Environmentally Friendly Reinforced Cohesive Soils

by

Michael Zachary Izzo

A thesis submitted to the Graduate Faculty of
Auburn University
in partial fulfillment of the
requirements for the Degree of
Master of Science

Auburn, Alabama
May 2, 2020

Keywords: desiccation cracking; cohesive soils; image processing; hydro-mechanical model

Approved by

Marta Miletić, Ph.D., Chair, Assistant Professor of Civil Engineering
Mark Barnett, Ph.D., Professor of Civil Engineering
Jack Montgomery, Ph.D., Assistant Professor of Civil Engineering

ABSTRACT

Desiccation cracking of cohesive soils is the development of cracks on the soil surface as a result of a reduction in soil water content. The decrease in soil surface area owing to the desiccation of cohesive soils has an undesirable impact on the mechanical, hydrological, thermal, and physio-chemical properties. Many efforts have been made to improve the desiccation crack resistance of cohesive soils, the most being chemical treatment using additives like cement and lime. Unfortunately, their use raises a number of environmental issues, so the demand for sustainable and environmentally friendly soil improvement alternatives is rapidly increasing. Therefore, the main objective of this study is to investigate eco-friendly soil improvement techniques and their effect on the desiccation cracking behavior of soils.

Improvement of soil crack resistance was studied by conducting desiccation cracking tests on two types of soils: Piedmont soil and white kaolin clay. Fly ash, recycled carpet fibers, bioplastic, and xanthan gum were all studied as potential sustainable soil improvement techniques. Unimproved and sustainably improved soils were compared by utilizing desiccation and mechanical tests. In addition, two types of image processing were conducted to quantitatively describe the effect of reinforcement on the geometrical characteristics of crack patterns. The experimental and image analysis results showed that soil improvement techniques generally enhanced the soil strength and reduced cracking.

The results from the physical tests were used along with data from other studies to calibrate a predictive hydro-mechanical numerical-analytical model. The model utilized soil-specific material properties in order to predict unsaturated water flow. This water flow was then used to model the strains and stresses that develop in the soil as a result which in turn predicted the initiation of desiccation crack behavior. Specific soil material properties were altered for the

various soil improvement techniques. The model predicted the development of stresses and radial

displacements as well time of crack initiation for untreated and improved specimens.

ACKNOWLEDEMENTS

While I would love to acknowledge everyone individually who has helped me throughout my time at Auburn, doing so would be practically impossible. I would, however, like to specifically thank a few people for their help on my path to obtaining a master's degree.

I would first like to thank my thesis advisor, Dr. Miletić. Even with the increased distance, you have been an outstanding mentor to me. No matter what has been going on, you have always been available to give advice and bounce ideas off of. I have enjoyed all of our talks, regardless of the topic. It has been a pleasure working under you for the past few years, both as a graduate student and as an undergrad, and I cannot thank you enough for providing me with the opportunity.

I would also like to thank the entire staff of the civil department. My time at Auburn allowed me to find something I was passionate about and that was only possible through your hard work and attitudes when teaching. I would also specifically like to thank the office staff for always helping me with whatever issues arose. I would also like to thank Dr. Barnett and Dr. Montgomery for agreeing to be on my committee and offering their thoughts on my work.

Next, I would like to thank my friends for the fun, laughs, and support over the last few years. Whether it was taking trips, hanging out on the weekend, or just listening to me vent, I could not have made it through this process without you. I also want to thank Antonio Soldo and Lydia Kennedy for their help in the lab. I especially want to thank Ross Ellis for helping me stay sane during the hours we were locked together in our office.

Finally, I must voice my profound gratitude to my family. To my brothers, Nicholas, Samuel, and Adam, thank you for all of the laughs throughout the years and always fostering a competitive spirit in me. You guys have always inspired me to always push myself to succeed. To my parents, Michael and Regena, thank you for the never-ending support and unfailing encouragement throughout my seemingly endless years of study and especially throughout the course of researching and authoring this thesis. From the driving me all over the place for soccer to always making time to listen when I call now, you guys have always done whatever you could for me. No matter what choices I have made throughout my life, I have always had you to fall back on. I love you all.

War Eagle!

TABLE OF CONTENTS

TABLE OF FIGURES

CHAPTER 1 INTRODUCTION

1.1 BACKGROUND

Desiccation cracking is the development of cracks at the soil surface and throughout the depth of a cohesive soil layer as a result of soil shrinkage due to the reduction of the water content through solar radiation or vegetation absorption. As the water content drops in the soil layer, the volume of cohesive soils begins to decrease. As the shrinkage occurs, tensile stress builds on the surface until that stress matches the tensile strength of the soil. At this point, a crack will occur in the soil face in order to release the stress that is being experienced. This process repeats until a complete crack network is formed.

The desiccation of cohesive soils leads to an undesirable impact on the mechanical, hydrological, thermal, and physio-chemical soil properties. For instance, desiccation cracking can lead to decreased soil strength, which in turn can cause uneven settlement and catastrophic failures in structures of all types. Structural damage is most prevalent in geotechnical structures such as flood dykes, dams, and slopes. As desiccation cracking decreases the strength of these structures, failure can become much more likely, potentially rendering the structures useless. In addition, this type of soil cracking results in a dramatic increase in the permeability of clayey soils. The increase in soil permeability is particularly problematic when the clay is used as a liner for both landfills and hazardous waste storage[1]. As a result, undesired paths for leachate and gas can form and affect the quality of the surrounding soil and perhaps most harmfully, the surrounding groundwater. Increased permeability can also have dramatic agricultural impact where water filters through soil far too quickly, vacating the root zone of vegetation before the required amount of hydration is

12

absorbed. Therefore, the prevention of desiccation cracking is of significant importance to safety, structural, and environmental issues.

While there are several methods for reducing desiccation cracking in soil, the most popular current methods possess a series of adverse effects on the environment. Cement and lime are the most common improvement techniques used for increasing a soil's tensile strength and crack resistance. Utilizing these methods comes with various negative side-effects. Both cement and lime can lead to increased carbon dioxide (CO_2) emissions, the reduction of vegetation growth, and groundwater contamination[2]. With this in mind, it is imperative to develop and validate alternative soil improvement techniques.

1.2 RESEARCH OBJECTIVES

This research was performed in order to examine sustainable and eco-friendly soil improvement techniques that could potentially reduce and/or prevent desiccation cracking from occurring in cohesive soils. An improvement technique was considered sustainable if it had originated and been refined from industrial waste, which remains toxic and hazardous to the environment when left unattended[3]. While this repurposing does not eliminate all negative side effects of the material as a waste product, it does prevent the adverse impacts of the use of alternative solutions[3]. An improvement technique was considered eco-friendly if it was not environmentally harmful[4]. This project also aimed to develop and analyze low-cost alternatives for image analysis of soil cracking behavior. A model was developed with the aim to predict cracking behavior in cohesive soils when subjected to soil improvement techniques.

This thesis details the process of analyzing desiccation cracking data, the use of image processing techniques, and the development and calibration of a numerical-analytical model. More detailed objectives of this project are:

• Gain the understanding of desiccation cracking processes and their mathematical description;

• Design and perform methods to measure cracking related physical properties;

• Develop and compare sustainable soil improvements under the same conditions;

• Compare soil improvement effectiveness when exposed to rewetting cycles;

• Develop low-cost image processing alternatives;

• Develop numerical-analytical model that is capable of capturing processes involved in unsaturated fluid flow in cohesive soils and, in turn, desiccation cracking;

• Conduct critical assessment of the modeling procedure and results;

• Provide recommendations of what techniques and results merit further discussion and research.

1.3 RESEARCH SCOPE

This study seeks to investigate novel eco-friendly soil improvement techniques and their effect on the desiccation cracking behavior of soils. The two types of cohesive soils that were used as part of this investigation were residual Piedmont soil and pure white kaolin clay. Four sustainable soil improvement techniques were tested, including fly ash, recycled carpet fibers, bioplastic, and xanthan gum. Both recycled carpet fibers and fly ash were considered sustainable materials under the idea that repurposed industrial waste is a sustainable material. Numerous studies have been conducted investigating the effects eco-friendly additives have on soil strength and swelling properties. Yet, their effect on the crack resistance of cohesive soils has been largely under-investigated. To date, neither recycled carpet fibers nor bioplastics have been examined as

a potential solution to desiccation cracking, and their effectiveness is presented in this research. This thesis is also the first study to compare these techniques at two different temperatures and to subject them to cyclic wetting and drying. Consequently, a comparative analysis of the mentioned improvement techniques' effectiveness has not been completed.

A qualitative analysis was conducted by analyzing the geometric characteristics of cracking patterns in the plain and improved soil samples. The quantitative analysis was completed using two different image processing techniques. The first was an original code powered by MATLAB's image analysis software before performing image matrix operations in a Visual Basic for Applications (VBA) program. The image analysis process is simple and inexpensive due to the widespread public familiarity and access to both VBA and MATLAB. The second technique was through the free use program GOM Correlate. A comparative analysis of the soil improvement techniques was completed using a combination of the area reduction factor (ARF), average crack width (w_{avg}), maximum crack width (w_{max}), maximum crack length (l_{max}), and maximum radial shrinkage (rs_{max}) of the treated and non-treated cohesive soil samples. To corroborate the results from the physical tests, an analytical model was developed with the goal to project the cracking behavior of cohesive soils subjected to different soil improvement techniques.

A predictive hydro-mechanical numerical-analytical model was developed in order to better analyze soil behavior as a function of improvement technique. The model created a field of water contents across both depth of the soil layer and time. These water contents were then used to determine shrinkage strain and then the stress conditions with time, depth, and radial distance changing. Two stress conditions were considered where the radial and hoop stress under a polar coordinate system were calculated based on whether the soil was still attached to the mold. The stresses were then used to predict the time of crack initiation as well as radial displacement of the

15

clay specimens for each improvement technique. The results of the hydro-mechanical model were then compared to the experimental results as a way to evaluate the model.

1.4 ORGANIZATION OF THESIS

This thesis was organized as follows:

Chapter 1 - Introduction provides background on the subject matter of this research project. The objectives for this research are also discussed. In addition, the scope of the research is addressed with a brief summary of the work completed. Finally, a brief outline of the overall organization of the thesis is given.

Chapter 2 – Literature Review details the mechanics of desiccation cracking and the processes involved in their initiation. Also included is an overview of the various physical tests that have been completed with the aim to measure and analyze cracking behavior. The myriad of image processing techniques that have been utilized is outlined in this chapter as well.

Chapter 2 also includes a summary of the different soil improvement techniques that have been used to reduce desiccation cracking, with a focus on those that are sustainable in nature. Finally, a breakdown of the different modeling methods that have been used to model cracking behavior is included.

The materials and methods utilized in this research are detailed in *Chapter 3 – Materials and Methods*. This includes the two different soil types that were studied as well as the five different materials that comprised the soil improvement techniques that were utilized. In-depth walkthroughs of each of the physical testing processes can also be found in this section. Finally, a comprehensive description of each of the image processing techniques is presented in this chapter.

In *Chapter 4 – Hydromechanical Model,* the background and process for developing the hydromechanical model is described. First, the numerical method utilized for creating the hydraulic portion of the model. Then, the method used for coupling the hydraulic model and the mechanical model is addressed. The analytical solution used to create the mechanical model is discussed afterwards. Finally, the procedure for obtaining each material property used in the model is addressed.

Chapter 5 – Results and Discussion of this thesis presents both the qualitative and quantitative results of the desiccation tests for both soil types. The results for the mechanical tests were also included. The results were used to compare the effectiveness of soil improvement techniques. Finally, the results from the hydro-mechanical model are detailed and compared to the experimental results.

Chapter 6 – Conclusions and Future Research Recommendations provides the general conclusions that were a result of the research completed in this project. Also included are proposals for future work based on the findings in this research.

CHAPTER 2 – LITERATURE REVIEW

2.1 INTRODUCTION

This chapter contains background information on desiccation cracking phenomena as well as the theory behind it. A review of the existing literature on the subsequent additional topics was conducted as well: physical tests for desiccation cracking, image processing techniques, sustainable soil improvement types, and numerical modeling of desiccation cracking. The following information based on previous work related to this research was crucial in the process of achieving a comprehensive understanding of the necessary information required to complete this project.

2.2 DESICCATION CRACKING BACKGROUND

In the most widely accepted explanation, desiccation cracks are formed as a result of soil volume shrinkage due to decreased water content, generally coming in the form of evaporation[5]. The shrinkage creates tensile stress within the soil and cracks develop when the tensile stresses experienced exceeds the tensile strength of the soil. However, the desiccation crack formation is a complicated process due to the link between the hydraulic and mechanical behavior of soils. Water loss during evaporation induces a rise in capillary forces, and the water transfer process in drying soils is basically controlled by the hydraulic properties of the soil mass. This, in turn, affects the mechanical behavior, because the soil tends to contract under increasing suction[6]. It has been stated that desiccation cracking is a coupled suction-contraction process. Suction and compressibility have been found to increase with the specific surface of the soil particles. Because clay particles are known to have the greatest specific surface of all soil particles, suction increases with clay content[7]. The increase in suction due to the water loss, decreases the volume of the voids in the

soil mass, introducing tensile stress. Another view on this process is that shrinkage strain is a function of water content loss[8,9]. As the water content in cohesive soils lessens, the shrinkage strain increases. The shrinkage strain increase will cause the soil to shrink globally, while being restricted by boundary conditions and material interfaces[9]. The restrictions on the shrinkage strain will cause the tensile stresses in the soil to increase, leading to desiccation cracking when the tensile strength of the soil is exceeded by tensile stresses in any horizontal direction.

A different approach to desiccation crack mechanics is centered on the air-water interface membrane. The belief is that the total tensile strength approach mentioned above disregards the frictional strength of uncemented soils. Initially, the air–water interface membrane resists entering pores, causing the capillary suction, or the difference between air pressure and water pressure in the voids of the soil, to increase, along with the effective stress. The soil then consolidates, and the skeletal stiffness of the soil mass increases. At a certain critical level, the air–water interface membrane enters the largest pores and causes particle displacement away from the entrance point. The void ratio increases at that point and facilitates further membrane invasion and crack growth. In the study exploring this approach, the effective stress at every point in the soil mass remained in compression[10].

Despite these approaches, crack initiation is also affected by the state of the soil surface.[8] Flaws in the soil surface can cause cracks to form in positions other than the location of the maximum tensile stress. Fracture mechanics dictate that the tensile stress required to initiate a flaw is inversely proportional to the flaw size. Therefore, a flaw large enough positioned away from the location of maximum stress could still be the location of the initial crack. This phenomenon is detailed in Figure 2.1, where Flaw 1 would most likely be activated first despite being located

away from the position of maximum tensile stress. Without any flaws, crack initiation would most likely occur at the center of the specimen, where the maximum tensile stress is located.
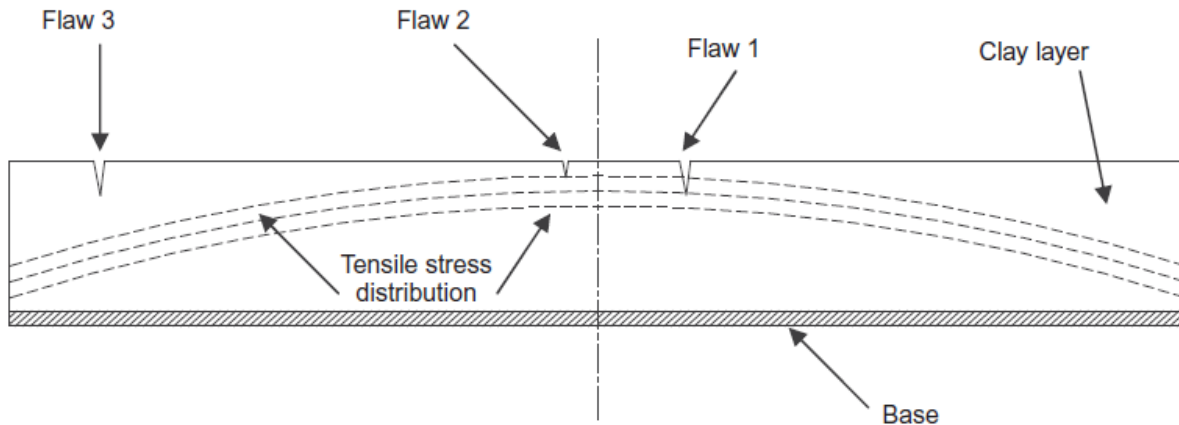
Figure 2.1 Tensile stress distribution with surface flaws considered[8]

2.3 PHYSICAL TESTS FOR DESICCATION CRACKING

Due to the lack of an accepted American Society for Testing and Materials (ASTM) standard, desiccation tests have been conducted in a variety of ways with different boundary conditions, specimen geometry, and properties measured[1,11–14]. Free desiccation tests have been used where wetted clay soil has been allowed to dry with the boundary conditions minimized. This is achieved by placing a demolded specimen on a surface that prevents adhesion. As a result, crack propagation does not initiate, and only volume loss due to evaporation occurs[1]. One dimensional (1D) desiccation testing places a constraint on the bottom of the clay sample[1,9]. This is often done by molding a bar of clay and placing it on a grooved plate. The grooved plate increases friction along the bottom of the sample and accelerates the cracking process while also producing cracks that only propagate in the same direction as the grooves.[1].An example of a 1D desiccation test can be

seen in Figure 2.2. The desiccation cracks are shown to propagate in the same direction as the grooves that can be seen underneath the samples.
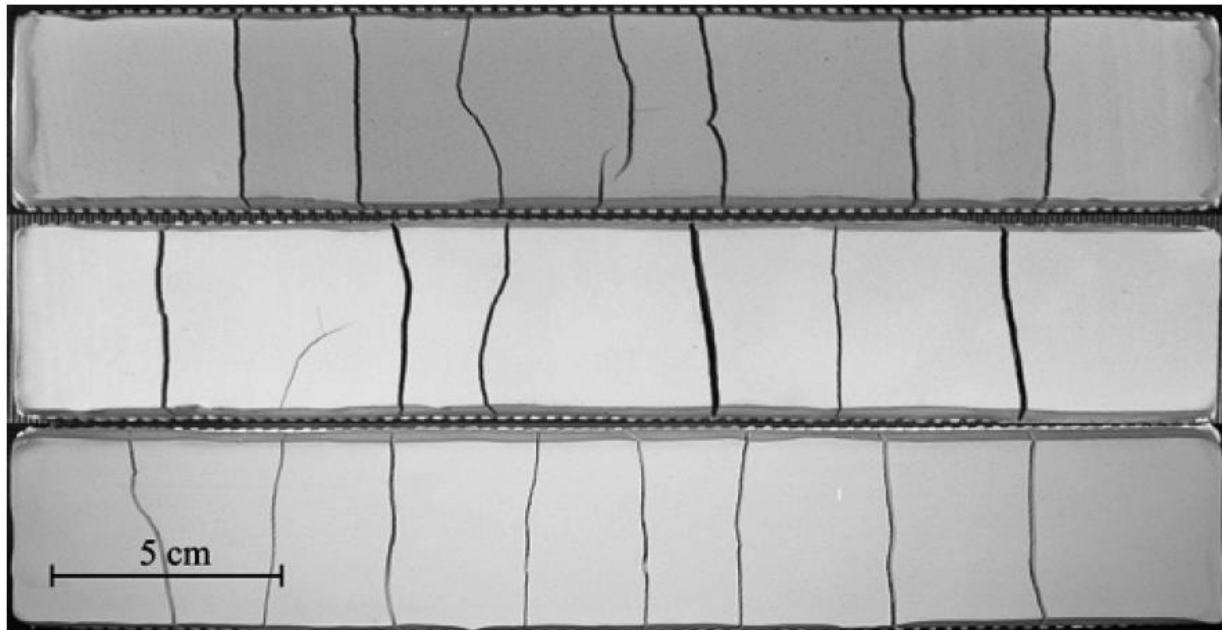
Figure 2.2 Crack patterns in 1D desiccation test[1]

Two (2D) and three-dimensional (3D) testing function in similar ways and can be considered simultaneously. The only difference between the two is that the thickness of the layer is such that crack depth can be variable in a 3D test, whereas in a 2D test, the soil layer is thin enough that all cracks are the depth of the entire layer. Two-dimensional cracking patterns can be obtained as a result of a complete horizontal constraint, allowing for crack intersections to be studied[8,11]. The results obtained from this type of desiccation test are more akin to those observed in nature and produce a more complicated cracking pattern. Figure 2.3 displays the complex crack pattern that occurs when more restraints are added in the 2D or 3D desiccation tests.
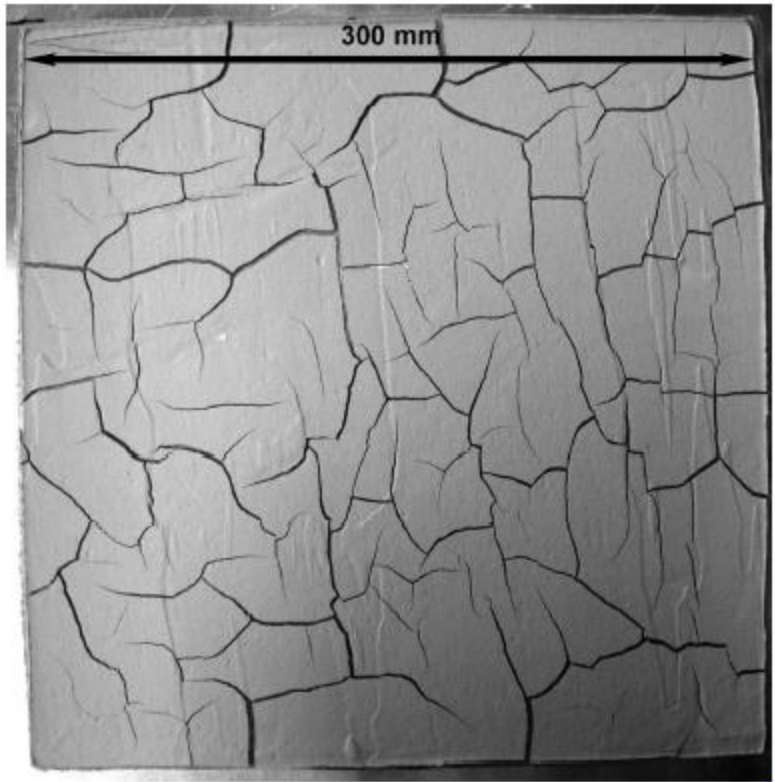
Figure 2.3 Crack patterns in 2D desiccation test[15]

Based on the analysis of the types of desiccation tests, a correlation can be seen between the type of test and crack propagation. Therefore, it can be deduced that the stresses that lead to cracking are a primary result of the applied restraining boundary conditions. Furthermore, the geometry of the crack pattern depends strongly on the nature of the boundary conditions and the sample geometry[1].

To quantitatively analyze desiccation and crack geometry, several parameters have been utilized. The water content is generally recorded over time as a way of measuring the amount of water loss due to evaporation. Suction is another variable often recorded during desiccation tests. The geometric characteristics of the cracks can be incredibly useful in evaluating the damage incurred by the soil. In 1D desiccation tests, the series of parallel cracks can be easily analyzed for

aperture and spacing[1]. Additionally, more complex variables have been developed to analyze the more complex crack patterns that develop in the 2D and 3D tests. A parameter called the crack distribution frequency (CDF) had been developed to evaluate the change in the area of a sample relative to a sample's original surface area[14]. A similar measurement, the crack intensity factor (CIF), has also been developed to analyze the ratio of the area of the cracks to the total specimen area[12]. In addition to the surface crack analysis, the crack depth can be analyzed using either manual means or more advanced image analysis techniques which will be detailed further in the following section.

2.4 IMAGE PROCESSING TECHNIQUES

Image analysis has proven to be an incredible tool to quantitatively analyze crack characteristics in natural and human made geomaterials. To this end, several experimental test methods have been suggested and developed to assess the desiccation crack initiation and propagation within the different geomaterials. These include an analysis of images acquired with a scanning electron microscope (SEM)[16,17], a 2D/3D profile laser[8,12], and different digital image acquisition systems[11,12,14]. An SEM has been extensively used to analyze micro-cracking in concrete and rocks[16] and to evaluate the effect of sodium chloride on the cracking of bentonite clay samples[11]. SEM has been utilized at the end of a desiccation test to assess the presence and pattern of desiccation cracking at a scale far smaller than the resolution provided by a digital camera. In addition, SEM allows the binding nature of different additives to be observed at a microscopic level. Despite the power of this technique, the main SEM drawback is its destructive nature. In particular, the specimen needs to be cut into thin slices, and the sample faces need to be polished to make cracks and material constituents visible before taking high-resolution 2D images.

Furthermore, due to the destructive and complex specimen preparation, the gradual propagation of a single crack cannot be studied by SEM alone.

The 2D laser profile imaging has been successfully utilized in studying the propagation and geometry of desiccation cracking in clay soils[13] and the soil curling as a result of soil dehydration[18]. The 2D laser scanner works using a triangulation principle for the 2D acquisition of a height profile along the line of the laser-generated by a special lens. This can be converted into a 3D image by affixing the laser to frame, which allows horizontal movement in the direction perpendicular to the length of the laser. The continuous height profile created by this setup allows for a complete profile of the sample. This setup also allows for tracking crack growth propagation across given cross-sections over time. Figure 2.4 shows the 3D model replication of samples received from the 2D laser affixed to a moving frame in comparison to a digital image. The model can then be analyzed for any cross-section to examine crack depth or crack width. The entire model surface can also be analyzed to determine surface area parameters.
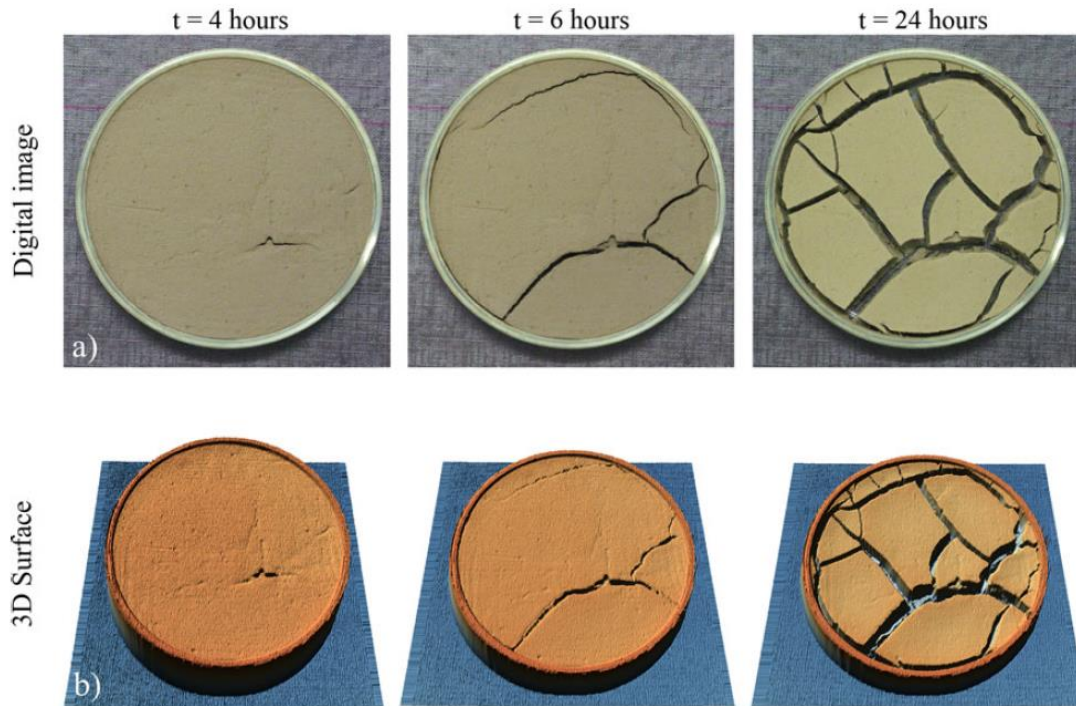
Figure 2.4 Soil sample replication using 2D profile laser on moving frame[13]

In addition, the 3D model allows for shrinkage to be tracked in terms of area for not just the entire surface but also each crack. While 2D profile lasers are powerful tools to study desiccation cracking, their initial high price creates a barrier to entry for the academic and industry communities. All of these shortcomings can be resolved by utilizing a user-friendly, inexpensive digital image acquisition system to analyze the cracking behavior of clay soils.

Utilizing a user-friendly, inexpensive digital image acquisition system to analyze the cracking behavior of clay soils can resolve some of the shortcomings of the aforementioned methods. Specifically, digital imaging methods can be a powerful alternative for analyzing the surficial features of cracks[12]. The image analysis process for desiccation cracking adheres to three main steps: image acquisition, image processing, and crack measurement. After taking photos with a digital camera, images are processed by adjusting the contrast and saturation to either greyscale or

binary images. Doing this allows for image analysis programs, like ImageJ, GOM, and VIC-2D, to determine crack measurements such as average crack width, crack spacing, and total cracked area[12].

2.5 SUSTAINABLE SOIL IMPROVEMENT TYPES

To resolve the safety, structural, and environmental issues caused by desiccation cracking, chemical additives, such as cement and lime, are used as binding agents to increase a clay's strength and resistance to cracking[19]. However, the current solutions have negative implications on the environment, such as CO_2 emissions, the prevention of vegetation growth, and the contamination of groundwater, among others[17]. To rectify this, several research studies have been conducted in order to determine the viability of different sustainable soil-strengthening additives. The soil additives are considered sustainable if they have originated and have been refined from the industrial waste, which remains toxic and hazardous to the environment when left unattended[3]. While this repurposing does not eliminate all negative side effects of the material as a waste product, it does prevent the adverse impacts of the use of alternative solutions[3]. The most commonly used sustainable soil additives are fly ash from thermal power plants[3,20,21], furnace slag from the steel industry[22,23], silica fume from the silicon and ferrosilicon industry[12,17,24,25], and carpet waste[26–28].

Chloride salts, such as ammonium chloride (NH_4Cl) and ferric chloride ($FeCl_3$), have demonstrated the ability to stabilize the volume of clays with high swelling potential[24]. The cations in the compounds reduce the swelling of montmorillonite minerals by replacing the interlayer metallic cations[25]. Furthermore, bentonite samples treated with sodium chloride (NaCl) developed cracks with greater lengths, but the overall crack density was significantly lower[17]. This was due

to the effect of salt on the bentonite colloidal interactions that alter the double layer and particle association in a clay slurry[17]. Meanwhile, the increased salt content can lead to a decrease in evaporation, which in turn, leads to decreased levels of tensile stress. The decrease in tensile stress and therefore less crack propagation[17]. Kalkan[24] used silica fume waste material as a sustainable alternative, and it was shown to significantly reduce desiccation cracking in clay liner systems. The silica fume works by decreasing the swelling capacity of cohesive soils. As a result, shrinkage strains are lessened in the soil layer and therefore tensile stresses are decreased[24].

The different types of fibers have also been examined as potential solutions to desiccation cracking[12,17,29]. Recycled carpet fibers have been lightly investigated as a potential soil improvement technique, with most studies being focused on the improvement of the strength properties of granular soil[27,28]. More recently, they have been examined as a potential method to reduce the swelling properties of cohesive soils[26]. It should be noted that the distribution of fibers is important to their effectiveness in strengthening soils[12]. If homogeneity is not maintained, cracks can initiate along the paths of least resistance. Shorter fibers have been shown to be more effective in establishing a uniform fiber distribution, while longer fibers are more likely to bunch, diminishing the effect of adding the fibers. Figure 2.5 shows the difference in fiber distribution for different lengths of fibers.
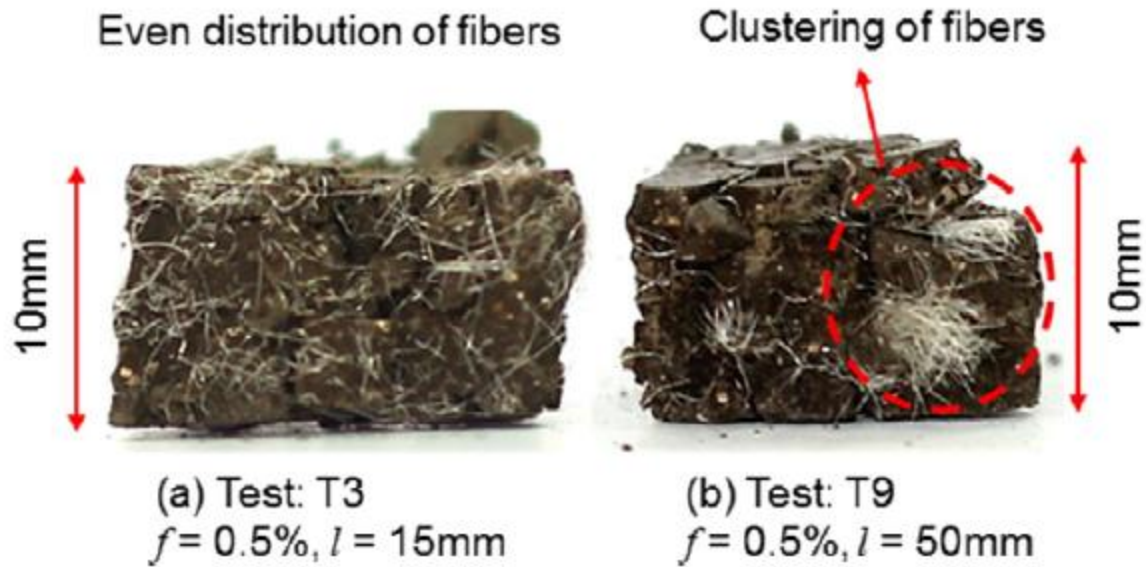
Figure 2.5 Fiber distribution when using fibers of different lengths[12]

Recycled carpet fibers were shown to decrease swelling pressure, with a 1% fiber content providing the most significant pressure drop[26]. Other unsustainable, fiber reinforcements have been shown to cause a substantial reduction of desiccation cracking in expanding clay, with crack width decreasing by 50%[29]. Polypropylene fiber reinforcement has been proven to prevent tension crack growth in soils and stabilize soils against shrinking by increasing the soil's tensile strength[17]. In addition, polypropylene fibers have been utilized to reinforce clay liners, leading the liners to be more rigid in compression and more ductile in tension[20]. The soils treated with fibers have also been shown to perform better than unreinforced soils when exposed to wetting and drying cycles[29].

Other forms of industrial waste have been examined as potential soil improvement techniques[20,21,30,31]. Fly ash has shown the ability to reduce plastic strain in clay soils when exposed to freeze-thaw cycles[21]. In addition, fly ash has been shown to increase compressive strength and produce similar behavioral trends to Portland cement[20]. The use of limestone waste has been shown to reduce the swelling properties of soil, producing a more compact microstructure when examined

using SEM imaging[30]. Milled brick debris has also been shown to improve the compressive strength of soils when tested using the unconfined compression test[31]. In recent years, biopolymers have been examined as an avenue for the strengthening of soils[32–36]. Xanthan gum has been shown to improve the shear strength and compressive strength of soil[32,33,35,36]. The increased strength is due to the bonding that occurs between particles as a result of the presence of the xanthan gum[32,34,35]. With the use of an SEM, this bonding can be seen at a microscopic level in Figure 2.6.
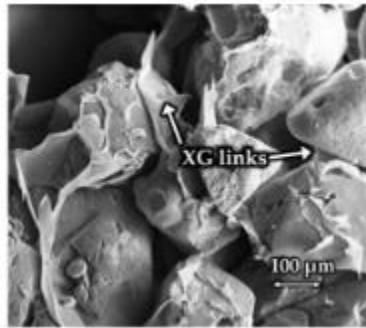
Figure 2.6 Soil bonding as a result of the addition of xanthan gum[34]

Along with xanthan gum, guar gum, beta 1,3/1,6 glucan, chitosan, and alginate have been compared in a study where the benefits of each were determined for four mechanical strength tests[34]. Xanthan gum, guar gum, and beta 1,3/1,6 glucan were all shown to be effective in increasing the strength of soil[34].

2.6 NUMERICAL MODELING OF DESICCATION CRACKING

Numerical models have been used as predictive tools for cracking in several different types of media. By inputting different materials qualities into the various commercially available software, models can be produced to predict cracking behavior under a variety of loads over time. One of the most popular methods is utilizing finite element software such as ABAQUS or ANSYS to create models to replicate cracking behavior. However, the finite element method, and by

extension, finite element software does not allow for discontinuities within the model, creating an additional obstacle when addressing cracking. To handle this issue, a couple of FEM variations exist in order to provide better modeling options. One of the most popular options is the extended finite element method or XFEM[37]. This procedure has emerged as a strong option for analyzing crack growth. Whereas FEM software forces discontinuities or cracks to follow the mesh, there is no need to track the crack path with a new mesh at each chronological stage. XFEM has been utilized on a variety of different research topics, including reinforced concrete cracking[37], thermal reflective cracking[38], and soil slope stability[39]. It remains a strong option for modeling the desiccation cracking that occurs in soils.

Another finite element approach is the mesh fragmentation approach[40]. This method was developed primarily to tackle the problem of desiccation cracking. To enact this procedure, elements with high aspect ratios are inserted between normal elements in a mesh. The new elements control the interactions between the original elements as well as introduce new nodes between the original mesh and new elements. With the model altered, the displacements of the new high aspect ratio elements can be considered the cracks undergone by the soil. After successfully modeling a soil sample, the model can be used to predict crack geometry as well as the strains and stresses that drying enacts on the soil[40]. Using this approach, crack geometry, as well as the stresses and strains experienced by the soil, can be determined. A set of heat maps of the tensile stresses developed in models utilizing the mesh fragmentation approach can be seen in Figure 2.7 for several soil layer depths. The first image for each sample is at the onset of cracking and the second displays the stresses at the end of the analysis period.
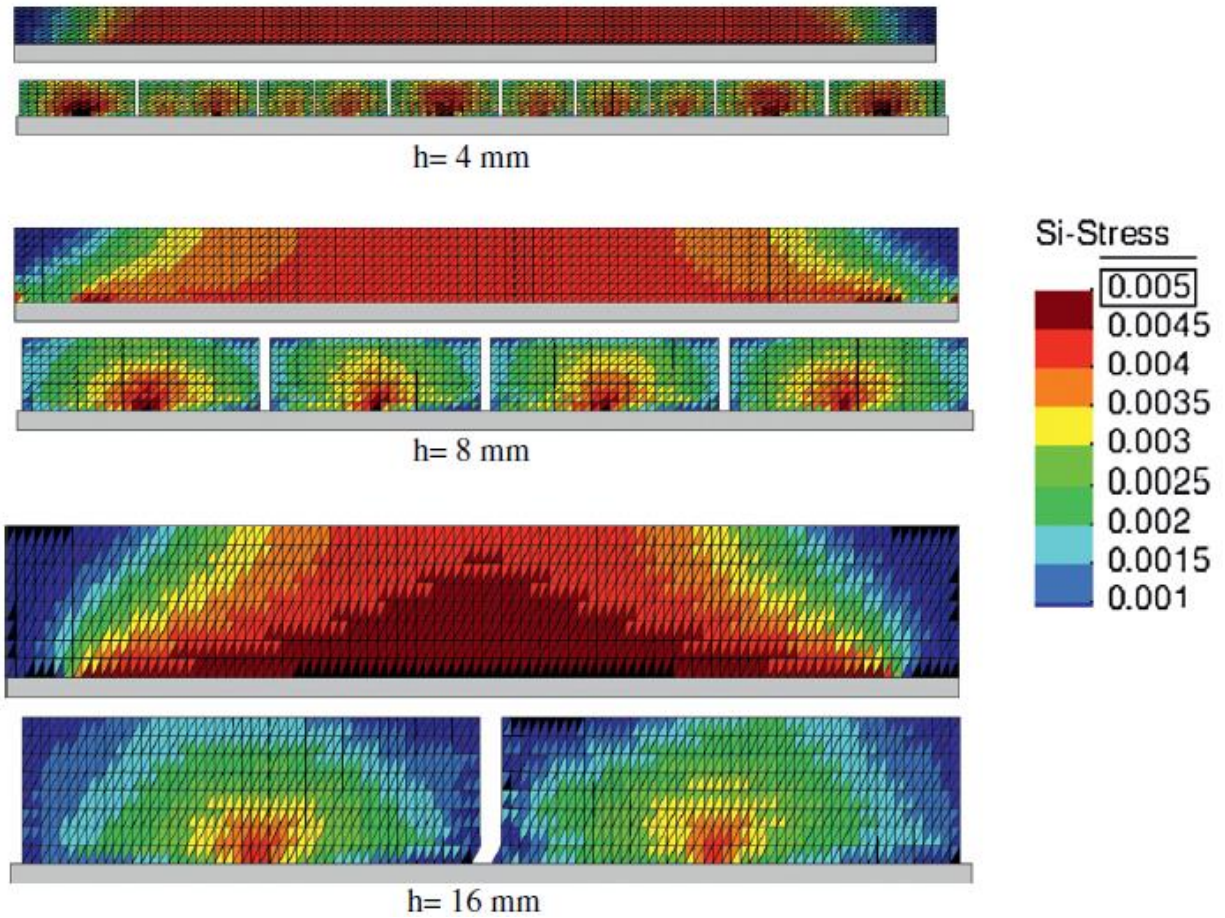
Figure 2.7 Tensile stresses at time of crack initiation and analysis end using mesh fragmentation approach[40]

A different modeling approach that still utilizes finite element software is the cohesive crack or cohesive segments approach[41]. This method inserts cohesive surfaces into finite elements, but only when the cohesive segments are necessary. The cracks are introduced to the model as jumps in the displacement field, effectively separating the media in the model. The size of the cracks is determined by material properties as well as load conditions. Because crack orientation is not constrained by the mesh, cracks can propagate in any direction.

Other modeling approaches have also been employed to handle cracking behavior. The distinct element method has been used to model cracking behavior in various materials, often with the software UDEC (Universal Distinct Element Code) which creates a continuum of finite difference elements[42,43]. The strength of distinct element programs lies in their ability to model the breaking up of material. However, fluid flow can only occur through joints in the model and not through the medium itself. Despite this issue, desiccation cracking can still be modeled if the progression of moisture content in the soil is known throughout the drying time. Perhaps most important for modeling the behavior of soil is the bond contact between elements. Because of the mechanical and physio-chemical interactions between clay particles, the elements are connected with cohesive bonds related to drying[43]. For desiccation cracking, this approach has been used to predict the number of cracks to propagate, the moisture content, crack width, crack length, and surface area shrinkage[44].

The discrete element method (DEM) has proven to be another alternative way to model desiccation cracking[43–46]. With DEM models, discrete particles are used to replicate soils on the aggregate scale. While this works well on smaller scale models, the computational power required to tackle larger problems provides a limit on its current viability[45]. In non-cohesive soils, DEM modeling is simplified, with soil considered to be a medium containing soil aggregates separated by pores that change in volume based on water content[49]. However, while cracking can be easily simulated at the aggregate scale, clay desiccation presents additional challenges when using DEM modeling. These issues can be overcome by making the assumption that shrinkage of clay occurs at the aggregate level and that mechanical properties of clay aggregate varies with water content[45]. The results of this approach can be seen in Figure 2.8, where the DEM model yields crack patterns similar in scale to the experimental results.
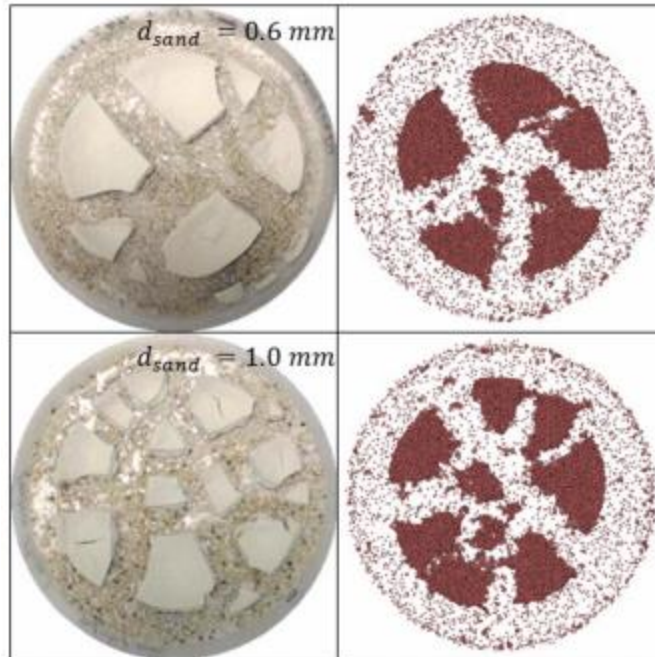
Figure 2.8 Comparison of experimental results and DEM model results[45]

2.7 ANALYTICAL MODELING OF DESICCATION CRACKING

Analytical models have also been used as predictive tools for cracking in soil[8,9,50,51]. For 1D desiccation tests, analytical models were capable of predicting not only initial cracking behavior but also additional cracking that occurred after[9]. The model treated the clay layer as an elastic material and shrinkage strains are applied to the clay as the soil dries. The strains are then converted into longitudinal tensile stresses, with maximum tensile stress occurring at the center of the specimen due to the boundary conditions associated with 1D desiccation tests. When the tensile stress exceeded the tensile strength of the soil, a crack would occur. After the crack initiated, the model would be split into essentially two specimens and the process is repeated until cracking transpires again. This will repeat itself until the maximum tensile stress between two cracks cannot

exceed the tensile strength of the soil regardless of the change in water content. The recursive process allows for crack spacing to be examined at the end of total crack propagation.

One desiccation theory of soft fine-grained soils creates a model that considers the growth of vertical cracks and desiccation under 3D shrinkage[50]. The key aspect in this model is the examination of the effective stress path of a soil layer while undergoing consolidation. Much like many other crack initiation determinations, cracking occurs when tensile stress surpasses the tensile strength of the media. In this case, crack propagation is determined with the cracking function approach where a crack will reach a certain depth when the void ratio at that point reaches a critical void ratio. While this process allows for the time of crack formation and the depth of cracking to be examined, crack spacing cannot be determined with this process.

A different model utilizes a similar approach yet provides a method for predicting the average spacing between primary cracks in conjunction with crack initiation and crack depth[51]. Linear elastic fracture mechanics and a stress superposition concept are used to add crack spacing as a prediction parameter. Initial cracking occurs when tensile stress is greater than the tensile strength of the soil. Crack depth is then determined using a trapezoidal stress distribution along with linear elastic fracture mechanics and an effective stress path which is dependent on soil type. Finally, a horizontal stress relief distribution is utilized to determine crack spacing with neighboring cracks existing when 95% of the tensile strength of the soil layer is exceeded. This model was compared against field observations for China clay with promising results.   While previous models examined 1D cracking, a 2D analytical model is also possible[8]. A polar coordinate system was adopted to handle the circular specimen shape of many desiccation tests. A segment of soil from the circular specimen (Figure 2.9) was analyzed in order to determine the functions for radial and angular stresses.
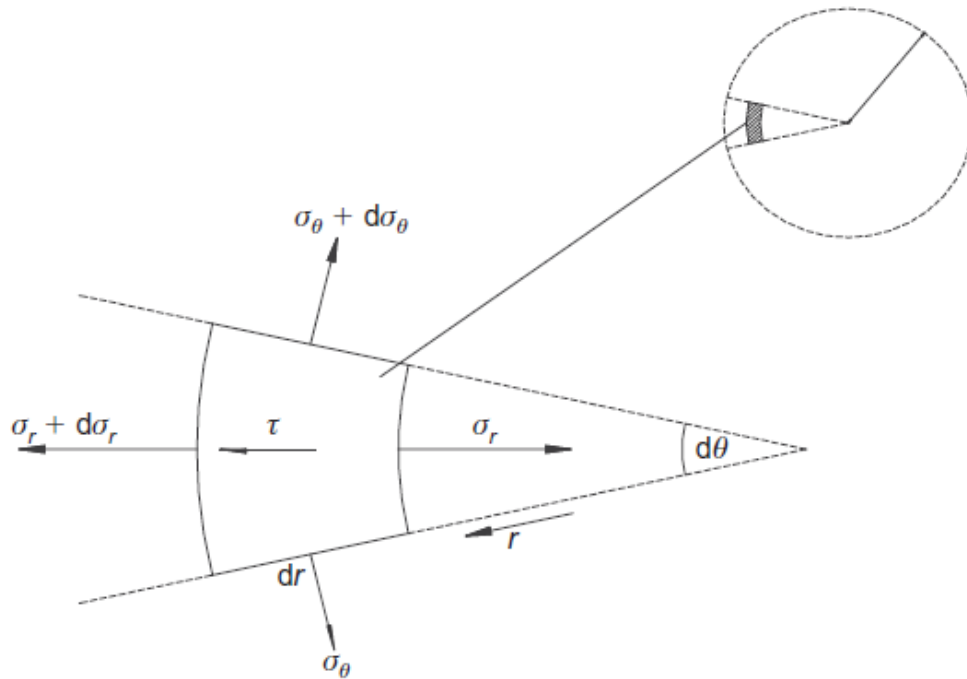
Figure 2.9 Polar coordinate system adopted in 2D analytical solution[8]

Using the change in water content as desiccation occurs, variable material properties, like Young's modulus and tensile strength, and potential shrinkage strain were determined. Stresses were calculated on the basis of two boundary conditions. The first boundary condition existed when the soil was still adhered to the mold wall. Here, no displacement occurred and both radial stress and angular stress were equal and functions of Young's modulus and potential shrinkage strain. The second boundary condition took place after soil detachment from the mold wall. In this case, radial displacement does occur and both stresses are governed inversely by radial distance along the clay segment, with angular stress always greater than radial stress. The model initiates in the first boundary condition and switches to the second only when the adhesion between the soil-mold interface is exceeded by the radial stress. Cracking can occur at any time when either stress is

greater than the tensile strength of the soil. Generally, the second boundary condition is reached before cracking occurs, so cracks initiate at the center of the specimen. While this model examines 2D horizontal cracking, it cannot predict crack spacing or crack depth.

CHAPTER 3 - MATERIALS AND EXPERIMENTAL PROCEDURE

3.1. INTRODUCTION

This chapter contains information on the materials and methods tested in this research project. Contained are both soil types as well as each of the soil improvement techniques that were evaluated. In addition, the procedures for each of the physical tests are stated, including each desiccation test and the two mechanical tests (unconfined compression and indirect tensile tests). Finally, the image acquisition, processing and analysis programs are described in detail.

3.2. MATERIALS

3.2.1. BASE SOIL

Two types of soil were used throughout the experimental program. The first base soil material used for experimentation was white kaolin clay. The soil was tested for its Atterberg Limits in accordance with ASTM D4318 [24], and the Liquid Limit and Plasticity Index were determined to be 45 and 13, respectively. As the soil is pure kaolinite, a sieve analysis was not performed as all particles would pass the #200 sieve (<0.075 mm). Therefore, according to the Unified Soil Classification System (USCS), the kaolin clay utilized in the study classified as CL, or lean clay. The specific gravity of the clay was assumed to be to be 2.4[52]. A photo of the dry kaolinite clay can be seen in Figure 3.1.

Figure 3.1 Dry kaolinite clay before alteration.

The second base soil material that was tested was residual Piedmont soil that had been sieved through the No. 40 sieve (0.420 mm). Piedmont soils have the reputation of not being particularly well categorized by the Unified Soil Classification System (USCS)[53]. An image of the dry soil can be found in Figure 3.2a. The soil behaves almost as a hybrid soil type, exhibiting characteristics of the fine-grained silt in undrained conditions, and the coarse-grained soil silty sand in drained conditions when loading is applied[53] [13]. Figure 3.2b depicts the grain size distribution curve for the base soil obtained using a wet sieve analysis. This soil was also tested for its Atterberg Limits in accordance with ASTM D4318[54], and the Liquid Limit and Plasticity Index were determined to be 49 and 20, respectively. Therefore, according to the USCS, the soil is classified as ML, or silt with low plasticity.
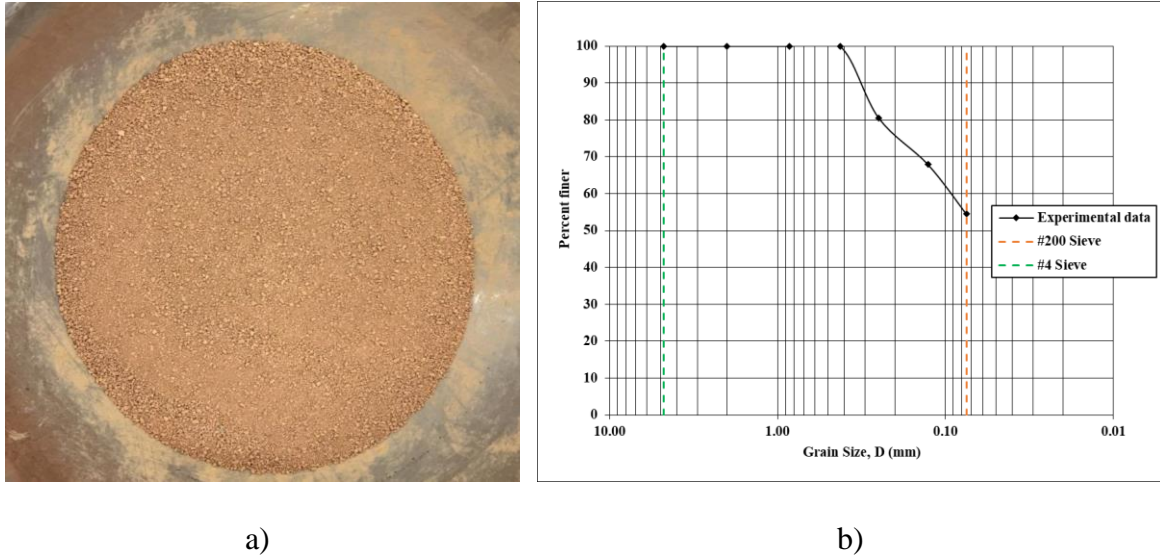
Figure 3.2 Dry Piedmont soil sieved through #40 sieve: a) image before alteration; b) gradation curve for soil before initial sieving.

3.2.2. SOIL IMPROVEMENT TYPES

In this study, the five additives investigated as strengthening agents were fly ash, recycled polyester carpet fibers, bioplastic, and xanthan gum, as well as a fly ash-fiber combination. The testing of the white kaolin clay included specimens improved with carpet fibers at two different volumetric fiber contents as well as xanthan gum. The improvement techniques tested with the Piedmont soil were fly ash, recycled carpet fibers, bioplastic as well as the fly ash-fiber combination.

The first tested improvement technique was Class C fly ash, which is the lightweight waste produced by burning pulverized coal. It has cementitious qualities and is often used as an additive during the concrete mixing procedure. Fly ash addition was 15% based on the dry weight of the soil. A photo of the Piedmont soil and fly ash can be found in Figure 3.3.

39

Figure 3.3 Dry Piedmont soil with fly ash.

The next soil improvement technique was introducing recycled polyester carpet fibers to the soil samples. The polyester fibers were short straight fibers manufactured by Beaulieu of America, USA. They had a length of 50 mm in the Piedmont soil tests and 10 mm in the kaolin clay tests with a consistent diameter of 0.3 mm (aspect ratio of 33). The density of the polyester fibers was 1.38 g/cm^3 (20 °C), and the volumetric fiber contents utilized included 0.5%, 1%, and 2% between the two soil types. A photo of the isolated recycled carpet fibers can be found in Figure 3.4.

Figure 3.4 Recycled carpet fibers cut to 10 mm.

A combination of Class C fly ash, and the carpet fibers was also tested as an improvement technique. The base material and fly ash were mixed first, where fly ash addition was 10% based on the dry weight of the soil. After the initial dry mixture was complete, polyester fiber was added until the sample contained 0.5% fibers by volume. A photo of the dry Piedmont soil with the combination improvement technique can be found in Figure 3.5.

Figure 3.5 Dry Piedmont soil with fly ash and carpet fibers.

Another improvement technique analyzed was a gelatin-based bioplastic. The gelatin-based bioplastic concentration was 8%. To achieve this, for every 500 grams of base material used, 44 grams of water, 30 grams of vinegar, 7.2 grams of gelatin, and three grams of glycerin were mixed together. To prepare the gelatin-based bioplastic, the water was boiled on a hot plate, with the gelatin being slowly added to prevent clumping. The vinegar and glycerin were then subsequently slowly mixed into the final blend. After thoroughly mixing all of the components, bioplastic was added to the base material sample soil and mixed again, until the homogenous soil-bioplastic mixture was achieved. A photo of the bioplastic-improved Piedmont soil before the additional water was added can be found in Figure 3.6.

Figure 3.6 Piedmont soil with bioplastic before additional water was added.

The final soil improvement technique analyzed was biopolymer xanthan gum. It is produced through the fermentation of glucose and sucrose[34]. Molecularly, xanthan gum is a polysaccharide or a long chain of carbohydrate molecules. Like many other polysaccharides, xanthan gum has

been used as a thickening agent for a variety of substances and has been used to increase the viscosity of liquids. In this study, samples with a mass concentration of 1% xanthan gum were tested. A photo of the isolated dry xanthan gum can be found in Figure 3.7.

Figure 3.7 Xanthan gum before being added to kaolinite clay.

3.3. METHODS

3.3.1. PIEDMONT SOIL DESICCATION TEST AND IMAGE ACQUISITION

To study the effect of temperature and wetting-drying cycles on each improvement techniques ability to reduce soil cracking behavior, two desiccation soil tests were performed on improved and non-improved Piedmont soil specimens. These were the standard desiccation test and oven desiccation test. The detailed procedure and accompanying image acquisition processes are described in the text below.

3.3.1.1 PIEDMONT SOIL STANDARD DESICCATION TEST

The standard desiccation crack test was performed on improved and non-improved Piedmont soil specimens. The purpose of the desiccation test was to study the cracking behavior of a soil sample as the sample reduces the moisture content and dehydrates due to extreme temperatures as well as the soil's response to a rewetting cycle. The samples were prepared by first collecting 800 grams of dry Piedmont soil in a mixing bowl. Next, the correct amount of dry improvement material was added to the dry clay. Afterward, all the dry materials were mixed thoroughly to ensure the distribution was as even as possible. In order to achieve the desired consistency, 200 grams of water were then added to bring the specimen's water content to 25%. The water content was based solely on the amount of dry soil and not additive. The soil was then spread in a lubricated, metal, cylindrical mold with a diameter of 230 mm and spread by spatula to achieve a uniform thickness of 20 mm.

A frame was used to place a digital camera at a height of 460 mm to ensure a consistent field of view. With the specimen prepared, an initial photo was taken of the soil before any desiccation could occur. Then, the specimen was placed at room temperature of approximately 20 °C for eight hours, with photos being taken every 30 minutes. The sample was then allowed to continue to dry overnight, and a final photo was taken at the 24-hour mark to determine the progression of desiccation cracking after one full day of drying.

3.3.1.2 PIEDMONT SOIL OVEN DESICCATION TEST

The oven desiccation crack test was performed on improved and non-improved Piedmont soil specimens. The purpose of the desiccation test was to study the cracking behavior of a soil sample as the sample reduces the moisture content and dehydrates due to extreme temperatures as

well as the soil's response to a rewetting cycle. The samples were prepared by first collecting 800 grams of dry Piedmont soil in a mixing bowl. Next, the correct amount of dry improvement material was added to the dry clay. Afterward, all the dry materials were mixed thoroughly to ensure the distribution was as even as possible. In order to achieve the desired consistency, 200 grams of water were then added to bring the specimen's water content to 25%. The water content was based solely on the amount of dry soil and not additive. The soil was then spread in a lubricated, metal, cylindrical mold with a diameter of 230 mm and spread by spatula to achieve a uniform thickness of 20 mm.

A frame was used to place a digital camera at a height of 460 mm to ensure a consistent perspective. With the specimen prepared, an initial photo was taken of the soil before any desiccation could occur. Then, the specimen was placed in an oven set at 105 °C for two hours, being removed every 15 minutes in order to take a photo to monitor crack propagation. At the two-hour mark, 200 grams of water were added to raise the water content back to 25%. The specimen was then tested for an additional 2 hours, with pictures continuing to be taken every 15 minutes.

3.3.2. KAOLIN CLAY DESICCATION TEST

The desiccation crack test was performed on improved and non-improved kaolin clay specimens. Like the Piedmont soil desiccation tests, the purpose of the kaolin clay desiccation test was to study the cracking behavior of a soil sample as the sample reduces the moisture content and dehydrates. The kaolin desiccation test was also designed with an eventual hydromechanical model in mind. The samples were prepared by first collecting 750 grams of dry kaolin clay in a mixing bowl. Next, the correct amount of dry improvement material was added to the dry clay. Afterwards, all the dry materials were mixed thoroughly to ensure the distribution was as even as possible.

Then 450 grams of water were added to raise the water content to the desired level of 60%. The water content was based solely on the amount of dry soil and not additive. This level was decided upon because it is above the liquid limit and allowed the samples to desiccate in a manageable timeframe. As a result, the soil was considered saturated. The water was added by slowly mixing the specimen while continuously adding water by spray bottle until all of the water has been added. Once thoroughly mixed, the soil specimens were manually placed into the cylindrically-shaped, transparent plastic molds and lightly smoothed to have a uniform clay thickness of approximately 30 mm. The inner diameter of the mold was 190 mm. After the sample was completely prepared, black pepper was sprinkled on the surface of the clay samples for the image analysis software. Black pepper was chosen because it would not affect the hydraulic properties of the clay while also maximizing the contrast for the image analysis process for the kaolin clay test. The speckle pattern was not necessary for the image analysis program utilized for the Piedmont soil desiccation tests.

Once the soil specimens and surface speckles were prepared, desiccation tests were performed to study cracking. The plain soil and each of the three additive configurations were tested under similar conditions. The entire experimental setup can be seen below. One trial for each improvement technique was also had the suction in the sample monitored and recorded. The entire experimental setup when testing for suction can be seen below (Figure 3.8). An electronic scale was set up to monitor the change in mass continuously over the duration of the experiment. Two electric heaters, set to 30°C, were placed on the left and right sides of the specimen in order to accelerate the drying process of the clay and to keep temperatures as consistent as possible. The plastic mold was placed upon a metal collar to allow for the tensiometers to be input at the bottom of the sample without disrupting the surface level cracking.

When testing for suction, a plastic disk with three holes in the walls was placed underneath the metal collar in order to allow for the tensiometer's cords to run to their corresponding data readers. The METER UMS Miniature-Tensiometer T5 tensiometers was used in these experiments. These tensiometers are capable of recording suctions in a range of 100 to -85 kPa which can be done in under five seconds. They can also be installed at any position and orientation, an imperative quality when being used in conjunction with digital image acquisition

The tensiometers were placed in three consistent locations. The first location was dead in the center of the sample, the second and third were 10 mm away from the edge, each creating perpendicular lines with the first tensiometer. This was done to monitor the suction at different locations in the clay and to see if the distance from the heaters played a substantial role in the suction developed. A schematic of the tensiometer alignment can be seen in Figure 3.8.

Figure 3.8 Tensiometer schematic

A dual thermometer/hygrometer was placed next to the sample to monitor both the temperature and humidity during the experiment. A 25.4 mm thick Styrofoam box was built in order to insulate the experiment and regulate the environment as much as possible. Finally, a Canon Powershot ELPH 360 HS digital camera was set up on a tripod to provide an aerial view of the crack propagation throughout the test. The tripod was set up at a constant height of 900 mm for each test. A photo of the experimental setup can be found in Figure 3.9.

The sample was allowed to dry under the same constant heating conditions for six hours. The samples were consistently monitored for the whole six-hour testing period. Every thirty minutes, the mass, temperature, and humidity were recorded, and a digital photograph was taken. In addition, the suction level was recorded at the same time increments for the tests where suction was being monitored. Finally, the height of the samples at the start and the end of the experiments were recorded in order to determine the height loss due to evaporation.

Figure 3.9 Setup for desiccation test of kaolinite clay.

3.3.3. UNCONFINED COMPRESSION TEST

The unconfined compression test is the laboratory test used to determine the compressive strength of a cohesive soil specimen. This test can be performed on untreated soil as well as a soil with a multitude of improvement techniques applied, including those tested in this project. Thus, the test was completed on the treated and untreated kaolinite clay with the ASTM standards (ASTM D2166/D2166M) in mind. The soil was prepared in the same way as the kaolinite desiccation test, except with a water content of 30% in order for the sample to maintain the integrity of its shape for testing. After completing the mixing process, the sample was placed into a mold with a diameter of 33 mm and a height of 71 mm. The specimen was then placed in an oven for 24 hours, heated at 105 °C. The next day, the sample was removed from the oven and was placed

into a loading device. In order to determine the compressive strength, an axial load was applied with a strain rate of 1.5%/min, complying with ASTM standards. The compressive strength was calculated by dividing the maximum load applied in the test by the cross-sectional area of the cylinder. To obtain Young's modulus of the sample, the applied load and an axial displacement were recorded. The increase in compressive stresses of the specimen was computed by dividing the load recorded during the test by the average cross-sectional area of the specimen. The increase in the axial strain was calculated as the change in height and the original specimen height. Finally, Young's modulus was determined to be the slope of the initial linear potion of the stress-strain curve that was obtained through this test. A photo of the experimental setup can be found in Figure 3.10.
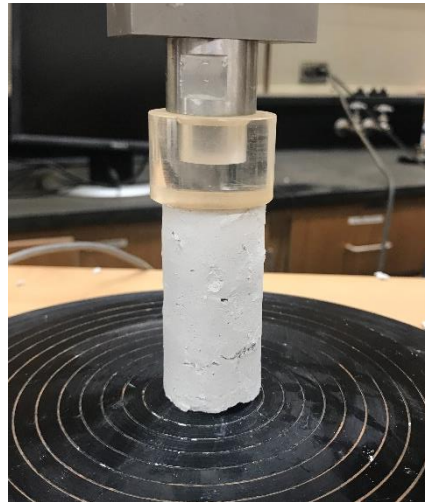
Figure 3.10 Setup for unconfined compression test of kaolinite clay.

3.3.4. SPLITTING TENSILE TEST

The splitting tensile test, also known as the Brazilian tensile test, is one of the indirect ways to determine the tensile strength of cohesive soil. The test can be done on an untreated soil as well as a soil with a multitude of improvement techniques applied, including those tested in this project.

The test was completed on the treated and untreated kaolinite clay with the ASTM standards (ASTM D3967-16) in mind. The soil was prepared in the same way as the kaolinite desiccation test, except with a water content of 30% in order for the sample to maintain its shape for testing. After completing the mixing process, the sample was loaded into a mold with a diameter of 35 mm. The mold was loaded in three, even lifts, with 25 compaction blows being administered for each lift. After the last lift was compacted, the collar of the mold was removed and the excess soil was evenly removed, leaving a cylinder of soil with a height of 18 mm. The specimen was then placed in an oven for 24 hours, heated at 105 °C. The next day, the sample was removed from the oven and was placed into a loading device with the lateral, rounded face down for testing. In order to determine the tensile strength, an axial load was applied with a strain rate of 1.5%/min, complying with ASTM standards. The tensile strength was calculated by utilizing the maximum compressive load and the geometric properties of the cylinder:

$$\sigma_t = \frac{2P\pi}{LD} \hspace{4cm} \text{Equation 3-1}$$

Equation where σ_t is the tensile strength of the soil; P is the maximum compressive load at failure; D is the diameter of the cylinder; L is specimen height. A photo of the experimental setup can be found in Figure 3.11.
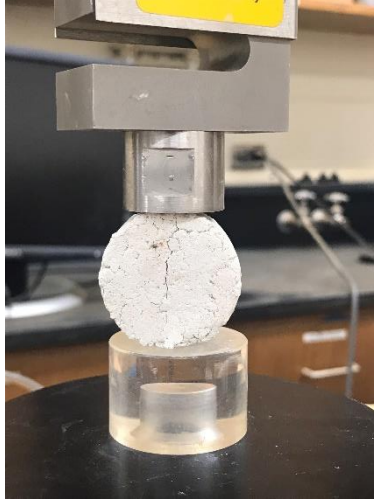
Figure 3.11 Setup for splitting tensile test of kaolinite clay.

3.3.5. DIGITAL IMAGE ANALYSIS PROCESS

Digital image analysis was completed for each of the specimens that were tested in the desiccation experiment. The series of nine photos corresponding to each data point were uploaded in chronological order to the image processing software GOM Correlate[55]. GOM Correlate functions by reading a dense speckle pattern on either a video file or a series of photos. Due to the duration of the time period, it was determined that a series of thirteen photographs would be better suited than a video of that extensive length. The program tracks the displacement of the speckles as time passes either by frame in the video or chronological digital still. An example of this process can be seen in Figure 3.12:
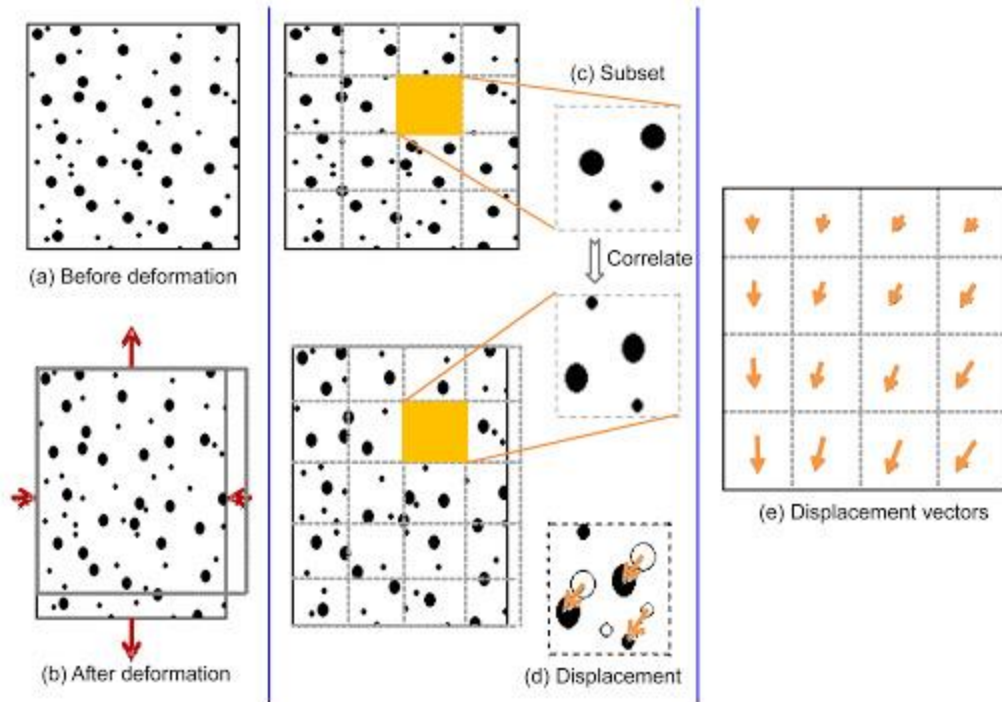
Figure 3.12 Determining displacement using image correlation[56]

Before tracking the displacement, the scale for the photos was determined by measuring an element

of known length and applying that distance to all the photos in the sequence. Then a surface

component is set, which essentially selects the region of importance in all of the images. For this

procedure, this means choosing the clay surface. The sensitivity of the surface component is

determined by adjusting the facet size and point distance with lower levels of increasing sensitivity.

However, if the levels are decreased too much, the entire surface component would not be readable.

With this in mind, for each set of photos, the surface component attributes were set to the lowest

possible level while maintaining the integrity of the overall surface component. When set correctly,

the only discontinuities in the component would be where cracking occurs. At this point, the

overall displacement was mapped on the images as a heat map on each image. The location with

the greatest displacement away from the component edge was used to identify the maximum crack

width. The maximum crack width was then determined using the measure tool within the software. The maximum crack length was determined by locating the longest continuous crack path on each image and measuring it with the measuring tool. Similarly to the maximum crack width, the radial shrinkage was determined by using the heat map. However, the radial shrinkage was viewed as an average value and the average of the values found on the edge of the surface component was recorded. The general process for the GOM Correlate image analysis can be seen in Figure 3.13.
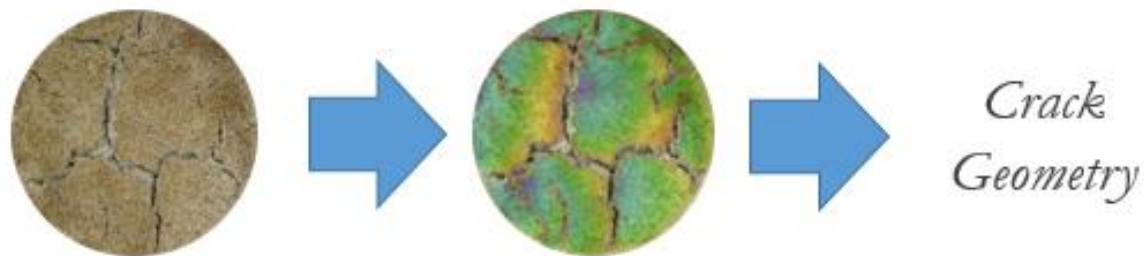
Figure 3.13 Image processing using GOM Correlate.

3.3.6. PIEDMONT SOIL IMAGE ACQUISITION AND PROCESSING

Digital images of the soil samples were taken at fixed time increments using a stand held at a constant position for image consistency and uniformity. Figure 3.14 provides the schematics of the experimental setup and soil arrangement. The image acquisition time frame increments were 15 and 30 minutes for the accelerated tests and standard test, respectively. For each image, the number of cracks in the specimen with a length of at least one centimeter was counted and recorded.
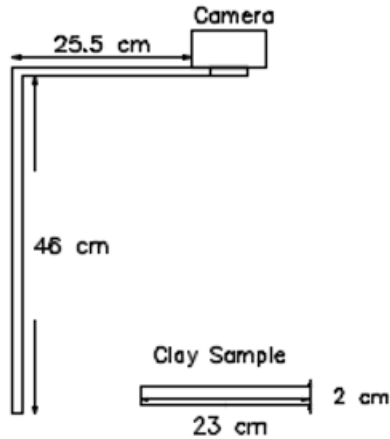
Figure 3.14 Experimental setup with a schematic of the camera and sample arrangement for the Piedmont soil desiccation test.

The digital image acquisition was followed by image processing to identify each constitutive component (cracks, fibers, and soil matrix) and, finally, quantitative analysis of crack geometric properties within the sample. In order to do so, the original MATLAB code was developed in this study using the MATLAB Image Processing Toolbox[57]. The image processing steps are described in more detail in the text below.

3.3.6.1 IMAGE CONVERSION

The extraction of desired information such as crack size, shape, and distribution from the acquired color digital image (Figure 3.15a) requires reading each color image and scaling it with the *imadjust* MATLAB function. The scaled image was further converted to a grayscale image with the *rgb2gray* function. Finally, with a sensitivity level set between .65 and .8 depending on the image, the grayscale image was then further transformed into a binary image with the *imbinarize* function (Figure 3.15b).

| a) | b) | c) | d) |
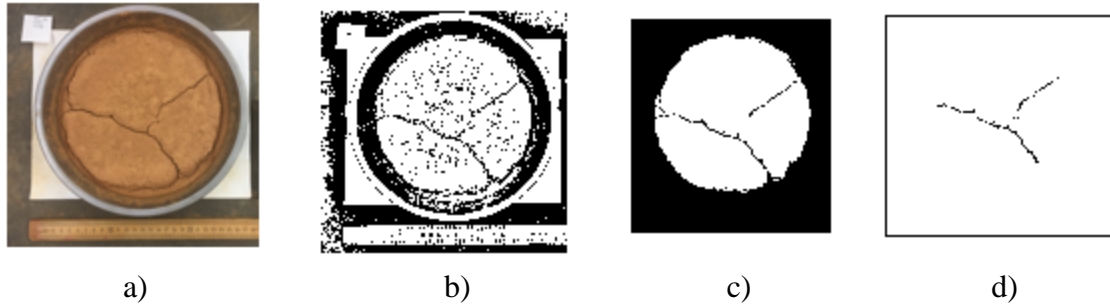
Figure 3.15 Image processing using the original MATLAB code: a) original sample photo; b) original binary image; c) clay surface binary image; d) isolated crack binary image.

3.3.6.2 SEGMENTATION

The binary images were analyzed to identify the cracked regions from the surrounding soil matrix in an image processing step called segmentation. In order to isolate the clay surfaces, the *bwselect* function was utilized to select areas of the image to remain white while the rest of the image was turned black. This was followed by removing blemishes from the image that developed as a result of uneven drying or divots in the specimen's surface with the *imfill* function (Figure 3.15c).

3.3.6.3 CALIBRATION

To convert all the data derived from the code into realistic values, a calibration factor was developed for each image. The *imdistance* line function was used to measure the diameter of the specimen's mold in linear pixels. Because the mold had a known diameter of 200 mm, a calibration factor was established by dividing 20 by the number of linear pixels recorded. This was done for each image to eliminate the effects of any slight fluctuations in the perspective of the original images.

3.3.6.4 ARF DETERMINATION

The surface area of each specimen was collected using the *bwarea* function and multiplying it by the calibration factor squared. The initial area ($Area_i$) for each specimen was stored using an

if-then statement and remained a constant for each chronological digital image for that specific soil improvement technique. Finally, the change in the area at each stage (*ΔArea*) in comparison with the initial area (*Area$_i$*) was used to determine the *ARF*:

$$ARF = \frac{\Delta Area}{Area_i}$$ Equation 3-2

3.3.6.5 CRACK MATRIX DEVELOPMENT

To accurately analyze crack width, the binary image of the crack needed to be isolated (Figure 3.15d). To do this, a circle the size of the specimen mold was overlaid onto the binary image in MATLAB, meaning the desiccation crack was the only black portion of the image remaining from Figure 3.15c. Then the *bwdistance* function was used to determine the minimum distance between each individual pixel and a pixel that was white. Effectively, this displayed the distance from each pixel inside a crack to the edge of a crack.

3.3.5.6 CRACK PARAMETERS

To quantitatively analyze the cracks, the crack matrix was exported into a VBA (Visual Basic for Applications) program. The information of every single cell in the crack matrix was checked. The maximum crack width (*w$_{max}$*) was determined by finding the cell representing the pixel that had the greatest distance to the desiccation crack edge. This was the maximum value in the entire matrix and represented the maximum crack width.

The average crack width (*w$_{avg}$*) was determined in a similar manner. The information of each cell in the matrix was checked to determine if it was the maximum value between itself and all adjacent cells. If it was a maximum value, the cell retained its value and if not, the cell's value was wiped. The average of the remaining nonzero values was found and used as the average crack

width of each sample. This approach was validated by matching code-calculated crack geometry with manual measurements.

CHAPTER 4 – HYDROMECHANICAL MODEL

4.1. INTRODUCTION

This chapter describes the predictive model for the moisture transfer and desiccation behavior of kaolin clay. First, the hydraulic modeling was discussed, primarily the modeling of moisture transfer process in a homogenous saturated and unsaturated material representing soil. Second, the coupling process between the hydraulic modeling and the mechanical modeling was explained. To complete the modeling process, the mechanical behavior and analytical approach in identifying the crack initiation criteria were discussed. Finally, the results of the combined analytical-numerical hydro-mechanical model are shown and compared to the experimental results for the kaolin clay physical test results.

4.2. SOIL WATER FLOW MODELING

4.2.1. SOIL WATER FLOW EQUATIONS

The movement of water in saturated and unsaturated soils can be represented with the Richard's equation[58]. It is a nonlinear partial differential equation, which is often challenging to approximate since it does not have a closed-form analytical solution. The main objective of the hydraulic modeling process was to develop a numerical solution to head-based Richard's equation, which can be seen in Equation 4-1:

$$C(h)\frac{\partial h}{\partial t} = \frac{\partial}{\partial z}\left[K(h)\frac{\partial h}{\partial z}\right] - \frac{\partial K(h)}{\partial z}, 0 \leq z < L, t > 0 \qquad \text{Equation 4-1}$$

where h is pressure head, t is time, z is depth, $K(h)$ is unsaturated hydraulic conductivity, and L is the soil layer depth. The $C(h)$ is a function describing the rate of change of saturation with respect the pressure head further and defined as follows:

$$C(h) = \frac{d\theta}{dh}$$

Equation 4-2

where θ is the volumetric water content.

The van Genuchten[59] model which defines the hydraulic conductivity as a function of the pressure head:

$$K(h) = K_s \frac{[1 - |\alpha h|^{n_G-1}(1 + |\alpha h|^{n_G})^{-m_G}]^2}{(1 + |\alpha h|^{n_G})^{\frac{m_G}{2}}}$$

Equation 4-3

and describes the SWCC curve:

$$\theta = \frac{\theta_s - \theta_r}{(1 + |\alpha h|^{n_G})^{m_G}} + \theta_r$$

Equation 4-4

was used in this study. In the above equations, K_s is the saturated hydraulic conductivity, α is an empirical constant with units in cm^{-1}, θ_s is the saturated water content, θ_r is the residual water content, and m_G and n_G are dimensionless empirical constants where the relationship between the two must be defined by:

$$m_G = 1 - \frac{1}{n_G}$$

Equation 4-5

Specific water capacity can then be defined by differentiating Equation 4-3 to yield to:

$$C(h) = \frac{n_G m_G \alpha (\theta_s - \theta_r)}{(1 + |\alpha h|^{n_G})^{m_G+1}} |\alpha h|^{n_G-1} \qquad \text{Equation 4-6}$$

Because the desiccation phenomena can be simplified as the vertical evaporation of water from soil with an initially uniform pressure head and a constant flux at the surface throughout the time of analysis, the initial and boundary conditions are defined as follows:

$$q(0,t) = \left[-K(h)\frac{dh}{dz} + K(h) \right]_{z=0} = q_a; t > 0 \qquad \text{Equation 4-7}$$

and

$$\left[\frac{\partial h}{\partial z} \right]_{z=L} = 0; t > 0 \qquad \text{Equation 4-8}$$

and

$$h(z,0) = h_b; 0 < z < L \qquad \text{Equation 4-9}$$

where h_b is the initial uniform pressure head and q_a is the constant evaporation flux.

4.2.2. DIFFERENCE APPROXIMATIONS PROCEDURE

Ultimately, the Crank-Nicholson finite difference method[60] was selected as an approximation approach to derive water content as a function of time, pressure head, and depth.

For this approximation, the source term was assumed to be zero. The first term of the right side of Equation 4-1 can be approximated by:

$$\frac{\partial}{\partial z}\left[K(h)\frac{\partial h}{\partial z}\right]_i = \frac{K_{i+\frac{1}{2}}(h_{i+1} - h_i) - K_{i-\frac{1}{2}}(h_i - h_{i-1})}{\Delta z^2} \qquad \text{Equation 4-10}$$

Likewise, the second term of the right side of Equation 4-1 can be approximated by:

$$\frac{\partial K}{\partial z}\Big|_i = \frac{K_{i+\frac{1}{2}} - K_{i-\frac{1}{2}}}{\Delta z} \qquad \text{Equation 4-11}$$

Furthermore, for the Crack-Nicolson approximation of the Richard's equation, the time derivative was replaced by a central difference approach centered at $(z_i, t_{n+1/2})$. This is achieved by taking the average of Equation 4-8 and Equation 4-9 at (z_i, t_n) and (z_i, t_{n+1}), respectively. Combining the averages for both terms with Equation 4-1 yields:

$$
\begin{aligned}
C_i^{n+\frac{1}{2}}\left(\frac{h_i^{n+1} - h_i^n}{\Delta t}\right) &= \frac{1}{2}\frac{\left[K_{i+\frac{1}{2}}^{n+\frac{1}{2}}(h_{i+1}^n - h_i^n) - K_{i-\frac{1}{2}}^{n+\frac{1}{2}}(h_i^n - h_{i-1}^n)\right]}{(\Delta z)^2} \\
&+ \frac{1}{2}\frac{\left[K_{i+\frac{1}{2}}^{n+\frac{1}{2}}(h_{i+1}^{n+1} - h_i^{n+1}) - K_{i-\frac{1}{2}}^{n+\frac{1}{2}}(h_i^{n+1} - h_{i-1}^{n+1})\right]}{(\Delta z)^2} - \frac{K_{i+\frac{1}{2}}^{n+\frac{1}{2}} - K_{i-\frac{1}{2}}^{n+\frac{1}{2}}}{\Delta z}
\end{aligned}
$$

Equation 4-12

Because the coefficients of the equation above $(C_i^{n+\frac{1}{2}}, K_{i+\frac{1}{2}}^{n+\frac{1}{2}}, K_{i-\frac{1}{2}}^{n+\frac{1}{2}})$ are dependent on h^{n+1}, the Crank-Nicholson approximation is considered nonlinear. To linearize a non-linear equation, a two-step implicit linearization procedure was used.

The initial step of this process requires the use of explicit linearization to get estimates of h^{n+1}, identified here as h^*. The linearization is completed by replacing C_i^{n+1}, $K_{i-1/2}^{n+1}$, and $K_{i+1/2}^{n+1}$ with C_i^n, $K_{i-1/2}^n$, and $K_{i+1/2}^n$ in Equation 4-12, respectively. This leads to the following equation:

$$C_i^n \left(\frac{h_i^* - h_i^n}{\Delta t}\right) = \frac{1}{2} \frac{\left[K_{i+\frac{1}{2}}^n(h_{i+1}^n - h_i^n) - K_{i-\frac{1}{2}}^n(h_i^n - h_{i-1}^n)\right]}{(\Delta z)^2}$$

$$+ \frac{1}{2} \frac{\left[K_{i+\frac{1}{2}}^n(h_{i+1}^* - h_i^*) - K_{i-\frac{1}{2}}^n(h_i^* - h_{i-1}^*)\right]}{(\Delta z)^2} - \frac{K_{i+\frac{1}{2}}^n - K_{i-\frac{1}{2}}^n}{\Delta z}$$

Equation 4-13

For the computational purposes, the above equation can be written in the following computational form:

$$-a_i^* h_{i-1}^* + (2 + b_i^* + a_i^*)h_i^* - b_i^* h_{i+1}^*$$

$$= (2 - a_i^* - b_i^*)h_i^n + a_i^* h_{i-1}^n + b_i^* h_{i+1}^n + 2\Delta z(a_i^* - b_i^*)$$

Equation 4-14

where:

$$a_i^* = \frac{(\Delta t)K_{i-\frac{1}{2}}^n}{(\Delta z)^2 C_i^n}, b_i^* = \frac{(\Delta t)K_{i+\frac{1}{2}}^n}{(\Delta z)^2 C_i^n}$$

Equation 4-15

The second step requires that Equation 4-12 is evaluated as:

$$C_i^{n+\frac{1}{2}}\left(\frac{h_i^{n+1} - h_i^n}{\Delta t}\right) = \frac{K_{i+\frac{1}{2}}^{n+\frac{1}{2}}}{\Delta z}\left[\frac{(h_{i+1}^n - h_i^n) + (h_{i+1}^{n+1} - h_i^{n+1})}{2\Delta z} - 1\right]$$

$$- \frac{K_{i-\frac{1}{2}}^{n+\frac{1}{2}}}{\Delta z}\left[\frac{(h_i^n - h_{i-1}^n) + (h_i^{n+1} - h_{i-1}^{n+1})}{2\Delta z} - 1\right]$$

Equation 4-16

63

The computational form for the second step is given by:

$$-a_i^{n+1}h_{i-1}^{n+1} + (2 + b_i^{n+1} + a_i^{n+1})h_i^{n+1} - b_i^{n+1}h_{i+1}^{n+1}$$

$$= (2 - a_i^{n+1} - b_i^{n+1})h_i^n + a_i^{n+1}h_{i-1}^n + b_i^* h_{i+1}^n + 2\Delta z(a_i^{n+1} - b_i^{n+1})$$

Equation 4-17

where:

$$a_i^* = \frac{(\Delta t)K_{i-\frac{1}{2}}^{n+\frac{1}{2}}}{(\Delta z)^2 C_i^{n+\frac{1}{2}}} , b_i^* = \frac{(\Delta t)K_{i+\frac{1}{2}}^{n+\frac{1}{2}}}{(\Delta z)^2 C_i^{n+\frac{1}{2}}}$$

Equation 4-18

The coefficients in Equation 4-18 are determined by making use of the equations below:

$$K_{i-\frac{1}{2}}^{n+\frac{1}{2}} = \frac{K_{i-\frac{1}{2}}^n + K_{i-\frac{1}{2}}^*}{2}$$

Equation 4-19

and

$$K_{i+\frac{1}{2}}^{n+\frac{1}{2}} = \frac{K_{i+\frac{1}{2}}^n + K_{i+\frac{1}{2}}^*}{2}$$

Equation 4-20

and

$$C_i^{n+\frac{1}{2}} = \frac{C_i^n + C_i^*}{2}$$

Equation 4-21

After the two-step linearization process was completed, the time iteration was advanced by the time step, and the procedure was repeated.

The internodal conductivities and specific water capacities were calculated using a simple arithmetic mean. While the actual code to achieve the Crank-Nicholson approximation utilizes Equation 4-14 and Equation 4-17, it is more convenient to address the boundary conditions of the problem using the theoretical versions found in Equation 4-13 and Equation 4-16.

While addressing the depth iterations, both the initial and final depth discretization step must be tackled. Therefore, Equation 4-13 must be evaluated when $i = 1$ and $i = m$ where m is the total number of distance steps. Doing so yields:

$$C_1^n \left(\frac{h_1^* - h_1^n}{\Delta t} \right) = \frac{K_{\frac{3}{2}}^n}{\Delta z} \left[\frac{(h_2^n - h_1^n) + (h_2^* - h_1^*)}{2\Delta z} - 1 \right]$$

$$- \frac{K_{\frac{1}{2}}^n}{\Delta z} \left[\frac{(h_1^n - h_0^n) + (h_1^* - h_0^*)}{2\Delta z} - 1 \right]$$

Equation 4-22

and

$$C_m^n \left(\frac{h_m^* - h_i^n}{\Delta t} \right) = \frac{K_{m+\frac{1}{2}}^n}{\Delta z} \left[\frac{(h_{m+1}^n - h_m^n) + (h_{m+1}^* - h_m^*)}{2\Delta z} - 1 \right]$$

$$- \frac{K_{m-\frac{1}{2}}^n}{\Delta z} \left[\frac{(h_m^n - h_{m-1}^n) + (h_m^* - h_{m-1}^*)}{2\Delta z} - 1 \right]$$

Equation 4-23

Therefore, it follows that the boundary condition at the soil surface (i.e., $z = 0$) is satisfied by rewriting Equation 4-22:

$$C_1^n \left(\frac{h_1^* - h_1^n}{\Delta t} \right) = \frac{K_{\frac{3}{2}}^n}{\Delta z} \left[\frac{(h_2^n - h_1^n) + (h_2^* - h_1^*)}{2\Delta z} - 1 \right] + \frac{q_a}{\Delta z} \qquad \text{Equation 4-24}$$

or in its computational form:

$$(2 + b_1^*)h_1^* - b_1^* h_2^* = (2 - b_1^*)h_1^n + b_1^* h_2^n - 2\Delta z b_1^* + \left(\frac{2\Delta q_a}{\Delta z C_1^n}\right) \qquad \text{Equation 4-25}$$

Similarly, the boundary condition at the bottom of soil layer (i.e., $z = L$) is satisfied by rewriting Equation 4-23 and by setting $h_{m+1}^* = h_m^*$ and $h_{m+1}^n = h_m^n$:

$$C_i^n \left(\frac{h_m^* - h_i^n}{\Delta t} \right) = -\frac{K_{m+\frac{1}{2}}^n}{\Delta z} - \frac{K_{m-\frac{1}{2}}^n}{\Delta z} \left[\frac{(h_m^n - h_{m-1}^n) + (h_m^* - h_{m-1}^*)}{2\Delta z} - 1 \right] \qquad \text{Equation 4-26}$$

or converted to its computational form:

$$-a_m^* h_{m-1}^* + (2 + a_m^*)h_m^* = (2 - a_m^*)h_m^n + a_m^* h_{m-1}^n + 2\Delta z(a_m^* - b_m^*) \qquad \text{Equation 4-27}$$

Utilizing the same process outlined in Equation 4-21 through Equation 4-27 but for the second step in the linearization process produces Equation 4-28 and Equation 4-29 to satisfy the boundary conditions where $i = 1$ and $i = m$ respectively in the computational form.

$$(2 + b_1^{n+1})h_1^{n+1} - b_1^{n+1}h_2^{n+1} = (2 - b_1^{n+1})h_1^{n+1} +$$
$$b_1^{n+1}h_2^{n+1} - 2\Delta z b_1^{n+1} + \left(\frac{2\Delta q_a}{\Delta z C_1^{n+\frac{1}{2}}}\right) \qquad \text{Equation 4-28}$$

$$-a_m^{n+1}h_{m-1}^{n+1} + (2 + a_m^{n+1})h_m^{n+1} = (2 - a_m^{n+1})h_m^n$$

$$+a_m^{n+1}h_{m-1}^n + 2\Delta z(a_m^{n+1} - b_m^{n+1})$$

<div align="right">Equation 4-29</div>

From here, Equation 4-14, Equation 4-25, and Equation 4-27 can be combined to form an m-number of linear equations to represent the first step of the two-step explicit linearization process. In a similar fashion, Equation 4-17, Equation 4-28, and Equation 4-29 can be combined to form an m-number of linear equations to represent the second step of the two-step explicit linearization process. The formulation of the set linear equations used to address the above process can be found in Appendix C.

Finally, Equation 4-3 and Equation 4-6 are then applied to the Crack-Nicholson approximation to return a field of pressure head results for depth and time. Those results are then input into Equation 4-4 to create a field of volumetric water contents for the same dimensions. The volumetric water contents were then converted into gravimetric water contents before being used as an input in the mechanical model. The collection of MATLAB codes used to perform these operations can be found in the Appendix B.

4.3. HYDROMECHANICAL COUPLING

To fully model the desiccation cracking process, the hydraulic and mechanical behavior need to be coupled. The one-way coupling was achieved through the use of the hydric constant (α_w)[8,9]. The hydric constant assumes a linear relationship between gravimetric water content loss (positive during drying) and shrinkage strain (ϵ_{sh}) as a percentage, which can be seen in the following equation:

$$\epsilon_{sh} = \alpha_w \Delta\theta \qquad\qquad \text{Equation 4-30}$$

The value of the hydric constant was obtained by quantifying the relationship between the two variables from the experimental data. For each time increment, the hydraulic problem is calculated as described in Section 4.2, and the output corresponding to the water content values were converted into shrinkage strains to be utilized as an input for the in the mechanical problem. The hydrological parameters are assumed to be independent of strain. The corresponding results from the mechanical model are not input into the hydraulic model and therefore model cracking behavior is only until the time of initial crack formation. One-way coupling is usually sufficient if the hydrological parameters are not expected to have a large impact on soil mechanical behavior.

4.4. MECHANICAL BEHAVIOR

In order to complete the hydromechanical model and to help with the interpretation of the experimental results, the following approximate analytical solution was developed and implemented for desiccation cracking in circular soil layers. During the desiccation and soil moisture evaporation, material properties and mechanical boundary effects will change[8,9]. Up to the onset of desiccation cracking, the soil was assumed as a macroscopically homogenous elastic continuum exhibiting axisymmetry. In this study, the desiccation crack initiation was based on a simple tensile failure criterion of tensile stress exceeding the material's tensile strength. All stresses in the vertical direction due to the self-weight are neglected. In addition, the soil layer is assumed to be in the plane-stress condition, because it is thin and is subjected to uniform stress with a stress-free surface at the top. In the analytical procedure described below, absolute stresses

and strains are used, but all of the equations could be written in incremental form for the non-linear analysis.

Combining together the equations of equilibrium, compatibility, and linear elastic constitutive law in plane stress the following boundary value problem of linear elasticity in two-dimensions can be formulated in polar coordinates[8] like in Figure 2.9:

$$(\sigma_r + d\sigma_r)(r + dr)hd\Theta - \sigma_r(rd\Theta)h + \tau rd\Theta dr$$
$$- \frac{\sigma_\Theta d\Theta}{2}hdr - \frac{(\sigma_\Theta + d\sigma_\Theta)d\Theta}{2}hdr = 0$$

Equation 4-31

where σ_r is the radial shrinkage stress; σ_Θ is the hoop shrinkage stress; r is the length along the radius of the clay specimen, from the center out; h is the specimen thickness; τ is the shear strength at the base of the sample due to the soil-mold interface; and $d\Theta$ is angle differential.

Through rearranging terms in Equation 4-31, the following differential equations of stress equilibrium can be achieved:

$$\frac{d\sigma_r}{dr} + \frac{\sigma_r - \sigma_\Theta}{r} = -\frac{\tau}{h}$$

Equation 4-32

It is well-known that water content has significant effects on soil mechanical behavior and properties. Similarly to the theoretical treatment of thermal stresses in solids[61], some authors have suggested that the shrinkage in soil layers can be proportional to the change in moisture content[8,9,62]. In this approach, soil suction is not required for the stress–strain constitutive equations, which is an advantage due to the difficulty and complexity of experimentally measuring soil suction. In contrast, the evolution of water content with time can be obtained easily in practical engineering.

However, if needed, the material properties can still depend on the soil suction, as the desiccation progresses.

Using elastic theory, the radial and hoop stresses can be defined as:

$$\sigma_r = \frac{E}{1-v^2}(\epsilon_r^T + v\epsilon_\Theta^T) \qquad \text{Equation 4-33}$$

$$\sigma_\Theta = \frac{E}{1-v^2}(\epsilon_\Theta^T + v\epsilon_r^T) \qquad \text{Equation 4-34}$$

where E is Young's Modulus, v is Poisson's ratio, ϵ_r^T is a total radial strain, and ϵ_Θ^T is total strain in the circumferential direction.

Total radial and total circumferential strains are defined as the sum of the actual (or mechanical) strain (ϵ_r and ϵ_Θ), and the shrinkage strain (ϵ_{sh}):

$$\epsilon_r^T = \epsilon_r + \epsilon_{sh} \qquad \text{Equation 4-35}$$

$$\epsilon_\Theta^T = \epsilon_\Theta + \epsilon_{sh} \qquad \text{Equation 4-36}$$

where ϵ_{sh} is shrinkage strain defined in Section 4.3. Furthermore, ϵ_r and ϵ_Θ are actual radial and circumferential strains, respectively given as:

$$\epsilon_r = \frac{dU_r}{dr} \qquad \text{Equation 4-37}$$

$$\epsilon_\Theta = \frac{U_r}{r} \qquad\qquad \text{Equation 4-38}$$

where U_r is the displacement in the radial direction.

Substituting Equation 4-35 through Equation 4-38 into Equation 4-33 and Equation 4-34 yield to the following expressions for the radial and hoop stresses:

$$\sigma_r = \frac{E}{1-v^2}\left[\frac{dU_r}{dr} + v\frac{U_r}{r} + (1+v)\epsilon_{sh}\right] \qquad\qquad \text{Equation 4-39}$$

$$\sigma_\Theta = \frac{E}{1-v^2}\left[\frac{U_r}{r} + v\frac{dU_r}{dr} + (1+v)\epsilon_{sh}\right] \qquad\qquad \text{Equation 4-40}$$

Furthermore, substituting Equation 4-33 through Equation 4-38 into Equation 4-32 gives:

$$\frac{d^2U_r}{dr^2} + \frac{1}{r}\frac{dU_r}{dr} - (1+v)\frac{d\epsilon_{sh}}{dr} = -\frac{\tau(1-v^2)}{Eh} \qquad\qquad \text{Equation 4-41}$$

Because of the assumed isotropic conditions in the clay specimen, $\frac{d\epsilon_{sh}}{dr}$ can be assumed to be zero. Therefore, Equation 4-41 reduces to the equation below:

$$\frac{d}{dr}\left[\frac{1}{r}\frac{d(rU_r)}{dr}\right] = -\frac{\tau(1-v^2)}{Eh} \qquad\qquad \text{Equation 4-42}$$

As will be detailed later on in Section 4.5, interface shear stress is a function of water content. Since the water content is a function only of depth and time, the interface shear stress is

71

constant in the radial direction. Integrating Equation 4-42 and then differentiating the result yield Equation 4-43 and Equation 4-44, respectively:

$$U_r = -= -\frac{\tau(1-v^2)}{Eh}\frac{r^2}{3} + \frac{Ar}{2} + \frac{B}{2} \qquad \text{Equation 4-43}$$

$$\frac{dU_r}{dr} = -= -\frac{\tau(1-v^2)}{Eh}\frac{2r}{3} + \frac{A}{2} \qquad \text{Equation 4-44}$$

In the above equations, both A and B are integration constants. From here, two mechanical boundary condition scenarios are analyzed.

4.5.1 PRE-WALL CRACK STRESS DERIVATION

The first scenario is when the clay specimen is still attached to the vertical wall of the mold. At this point, the radial stress is less than the interface adhesion between the sample and the mold. This adhesion value will be further explained in Section 5.5. Therefore, in this circumstance, $U_r = 0$ when $r = 0$ and when $r = r_0$ or the maximum radial distance. Because no radial displacement occurs in this environment, τ can be assumed to be zero as well. With the above information, Equation 4-43 and Equation 4-44 are solved for constants A and B and then plugged into Equation 4-39 and Equation 4-40 to obtain the radial and hoop stresses for the attached wall scenario. The equations for each stress can be seen below:

$$\sigma_r = \frac{E}{1-v}\epsilon_{sh} \qquad \text{Equation 4-45}$$

$$\sigma_\Theta = \frac{E}{1 - v} \epsilon_{sh}$$

Equation 4-46

4.5.2 POST-WALL CRACK STRESS DERIVATION

Once the radial stress evaluated under the previous conditions exceeds the adhesion value between the mold and clay, the second scenario is evaluated. In this environment, the specimen edge is free to be displaced in the negative radial direction. This yields new boundary conditions where $U_r = 0$ when $r = 0$ and $\sigma_r = 0$ when $r = r_0$. With these new boundary conditions, Equation 4-43 and Equation 4-44 are solved for constants A and B and then plugged into Equation 4-39 and Equation 4-40 to obtain the radial stress, hoop stress, and radial displacement for the free movement scenario. The equations for each can be seen below:

$$\sigma_r = \frac{\tau(2 + v)}{3h}(r_0 - r)$$

Equation 4-47

$$\sigma_\Theta = \frac{\tau}{3h}[(2 + v)r_0 - (1 + v)r]$$

Equation 4-48

$$U_r = \frac{\tau(1 - v)r}{3Eh}[(2 + v)r_0 - (1 + v)r] - r\epsilon_{sh}$$

Equation 4-49

4.5.3 STRESS STATE DISCUSSION

The equations above provide a reliable avenue for analysis of the stress field under both sets of boundary conditions. Equation 4-45 and Equation 4-46 show that the radial stress and hoop

stress are equal at all points, meaning a uniform tensile stress field exists under ideal conditions. This creates a situation where the first crack will most likely occur along the soil-mold interface as the tensile strength of the soil is generally higher than the adhesion of soil to the mold. In the rarer scenario where the tensile strength of the soil is less than the adhesion value, a crack would be equally likely to occur anywhere in the soil surface.

Once the wall crack has formed, the new stress and displacement distributions are based on Equation 4-47, Equation 4-48, and Equation 4-49. At this point, the radial and hoop stress possess an inverse linear correlation along the radius with the max stress occurring at the center of the specimen. However, they do not decrease at the same rate. Whereas the radial stress will decrease to zero at the edge of the specimen, the hoop stress will maintain a residual value at the edge. As a result, the hoop stress is greater than the radial stress at all points in the specimen, aside from the center. This results in cracks initiating at the center and radiating out to the edge, perpendicular to the greater hoop stress. Real-life crack patterns, however, will diverge from this pattern and will be governed by flaws in the soil surface, specifically their size and orientation[8].

CHAPTER 5 – RESULTS AND DISCUSSION

5.1 INTRODUCTION

This chapter contains the data from each of the desiccation tests performed for both soil types. Also included in this section are the results of the two unique image processing techniques for both soil types. The results from the mechanical tests performed on the plain and reinforced kaolinite clay soil are contained within this section as well. Then, a discussion of the results has been completed. Finally, the results of the combined analytical-numerical hydro-mechanical model are shown and compared to the experimental results for the kaolin clay physical test results.

5.2 PIEDMONT SOIL RESULTS

Using the data obtained from the MATLAB image analysis process, the performance of each of the selected improvement methods for the Piedmont soil was examined. The final crack segment count, w_{avg}, and w_{max} were logged at each time frame during the oven desiccation test. Generally, the cracks propagated quickly, with the specimens often progressing from no cracks to a complete crack geometry in one testing interval (15-minute time frame). The progression of the cracking throughout the primary drying cycle of the oven test can be seen in Figure 5.1.
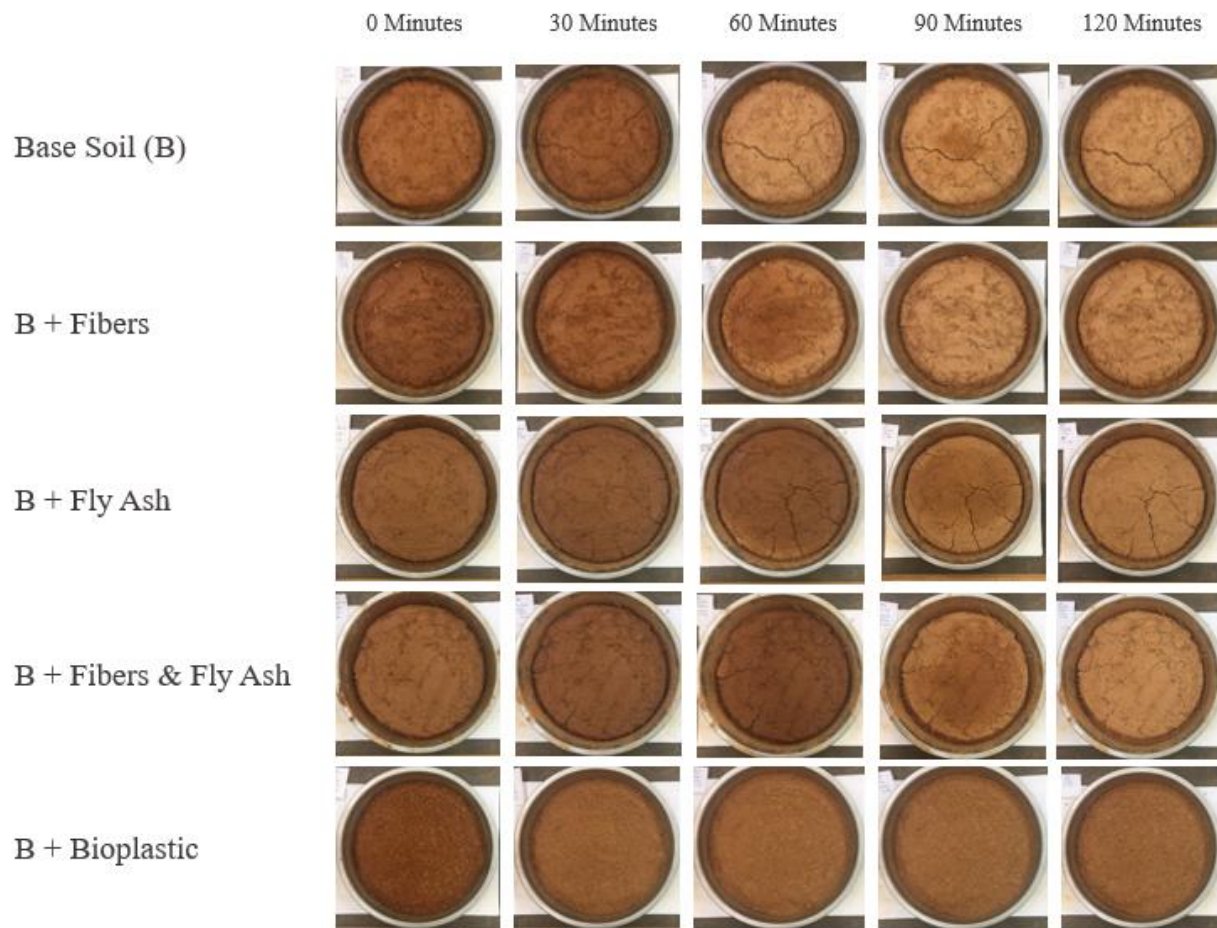
Figure 5.1 Desiccation crack test results for accelerated test after two hours of drying.

Figure 5.1 and Figure 5.2 show that the cracking pattern of the untreated, Piedmont soil sample spread in a three-pronged, letter Y-like pattern.
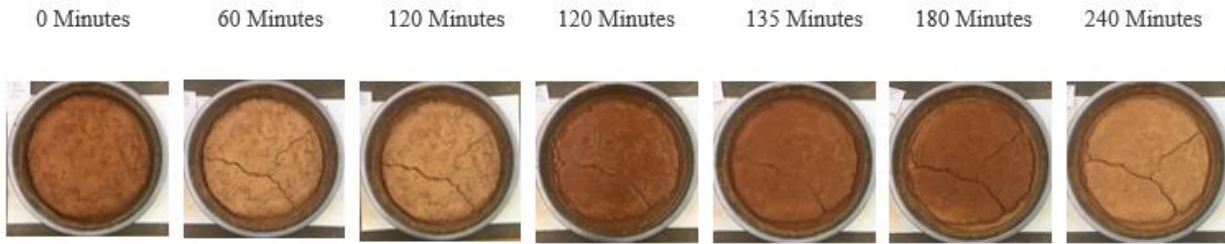
Figure 5.2 Desiccation crack test results for accelerated oven desiccation test for untreated soil. The two 120 minute stages show before and after shots of the rewetting process.

However, the samples altered with the fly ash and carpet fibers would deviate from this geometry sometimes. Once the soil specimen with the added fiber cracked in the second drying cycle, the specimen's crack pattern had a more circular shape, much like the letter C with smaller branches radiating out to the edge of the soil (Figure 5.3). The reason for this was most likely due to the fibers' transverse isotropic distribution, a potential consequence of the soil mixing process. Because the soil was prepared by mixing in a circular motion, the majority of the fibers likely became orientated in the same direction. The likelihood of this was increased by the relation between the length of the fibers and the depth of the clay layer. The clay layer was approximately 20 mm thick and the 50 mm fibers could not be orientated in a vertical direction. As a result, cracks formed parallel to the carpet fiber alignment due to the absence of reinforcement oriented across the cracks. The samples improved with fly ash tended to possess a more unbalanced pattern and spread in a more concentrated manner.

Figure 5.3 Accelerated test final crack distribution for fiber-aided soil

For the room temperature desiccation test, only the *ARF* results were documented for each chronologic digital photograph because the crack progression did not initiate at standard temperatures during the first eight hours of the testing period. Along with the ARF, w_{avg}, w_{max}, and the final crack count were recorded the next day after a full 24 hours of desiccation.

The number of cracks was documented so that the crack network morphology could be quantitatively evaluated. The findings from the standard test can be found in Figure 5.4. The graph reveals that the improvement techniques did not substantially alter the overall number of crack segments after a full day of dehydrating at standard room temperature, with the exception of the gelatin-based bioplastic. Both the sample with fly ash and the sample with the fly ash-fiber combination developed an extra crack segment over the unimproved soil.
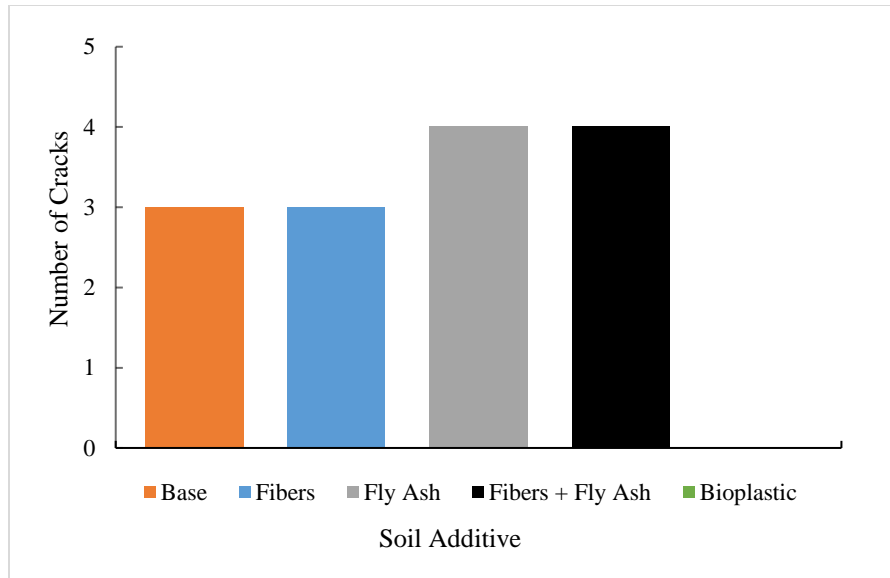
Figure 5.4 Number of cracks developed in standard desiccation test after 24 hours at room temperature

The crack count data for the oven desiccation test can be observed in Figure 5.5. The graph indicates that in the initial drying cycle (Figure 5.5a), no cracks propagated in the samples improved with the bioplastic or with the carpet fibers by themselves. Interestingly, the additional fly ash in the specimen improved by the combination treatment did not compensate for the reduction in fiber content. When cracks did develop, they usually emerged after the first 15-minute heating period. During the second drying cycle and after the rewetting process (Figure 5.5b), only the bioplastic-improved soil specimen did not develop any cracks. For each of the other improvement techniques, cracks propagated at a higher number than the untreated soil at the end of the entire test. After rewetting, crack formation initiation varied to a much greater extent with the untreated soil cracking after 15 minutes, the fiber-improved soil cracking after 30 minutes, the fly ash specimen developing cracks at the 45-minute mark, and the hybrid improvement method counteracting cracking until 75 minutes after rewetting transpired.

a)   b)
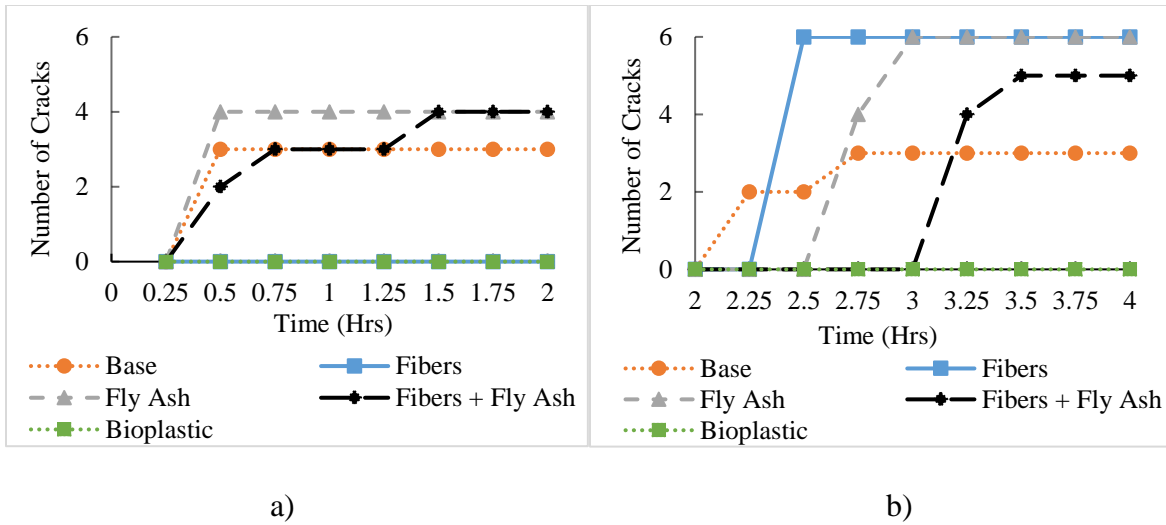
Figure 5.5 Development of the desiccation cracks in the accelerated test: a) first drying cycle; b) second drying cycle

The w_{avg} was computed so that each soil additive's aptitude in exclusively decreasing crack progression could be observed. The effect of the different soil improvement techniques on the w_{avg} for the room temperature desiccation test was recorded in Figure 5.6. The average crack width after a full day of drying for the untreated soil was found to be 1.59 mm. The sample enhanced with fly ash displayed almost no improvement over the untreated specimen. Both samples that included carpet fibers in their method developed cracks with reduced average widths of about 0.9 mm after testing was complete. The sample with the bioplastic had an average crack width of zero as cracks did not propagate during the standard desiccation test.
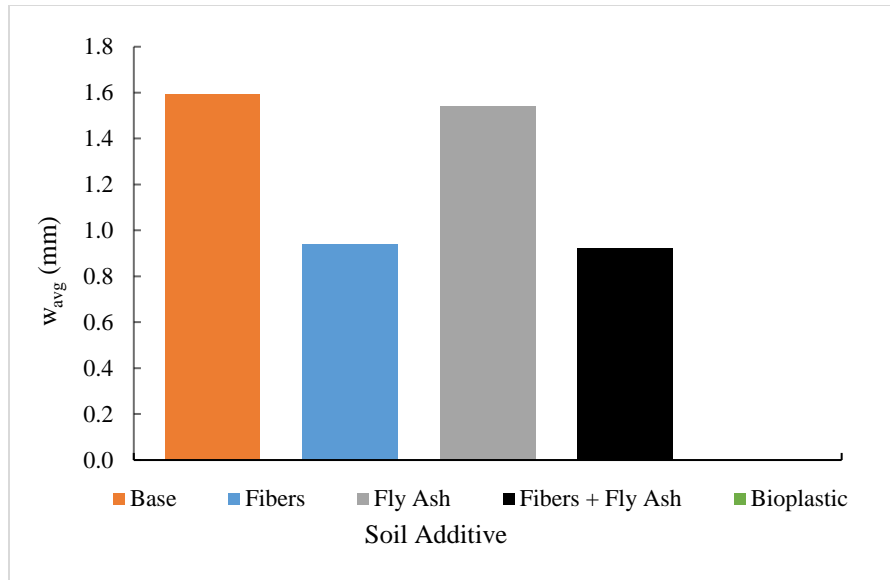
Figure 5.6 Average crack width of soils under standard desiccation test at the 24-hour mark

The influence of different soil improvement techniques on the w_{avg} for the oven desiccation test is shown in Figure 5.7. The average crack width at the conclusion of the rewetting cycle for the untreated soil was discovered to be 1.54 mm (Figure 5.7b). The samples with solely fly ash and carpet fibers respectively showed minimal improvement over the plain Piedmont soil. The specimen with the carpet fibers-fly ash hybrid treatment method developed cracks with reduced average widths at the conclusion of testing. The specimen with bioplastic added did not develop cracks during this test either and, therefore, average crack width of zero. It should be noted that the crack width after the rewetting process was taken to be zero. Though some soil damage can be detected, fully realized cracks were not existing at that stage. This can be observed by referring to Figure 5.2, where the second 120-minute mark displays an outline of a crack that has been filled in by the rewetting process. In addition, in some intervals, the average crack width was shown to reduce, imitating the soil repairing itself. In fact, this was not due to the cracks lessening, but as a consequence of slight image processing inconsistencies where the software reads darker, wet spots

in the soil adjacent to the cracks as a portion of the actual crack. As the soil desiccated more, the wet spots vanished, causing the software to process the change as cracks narrowing.
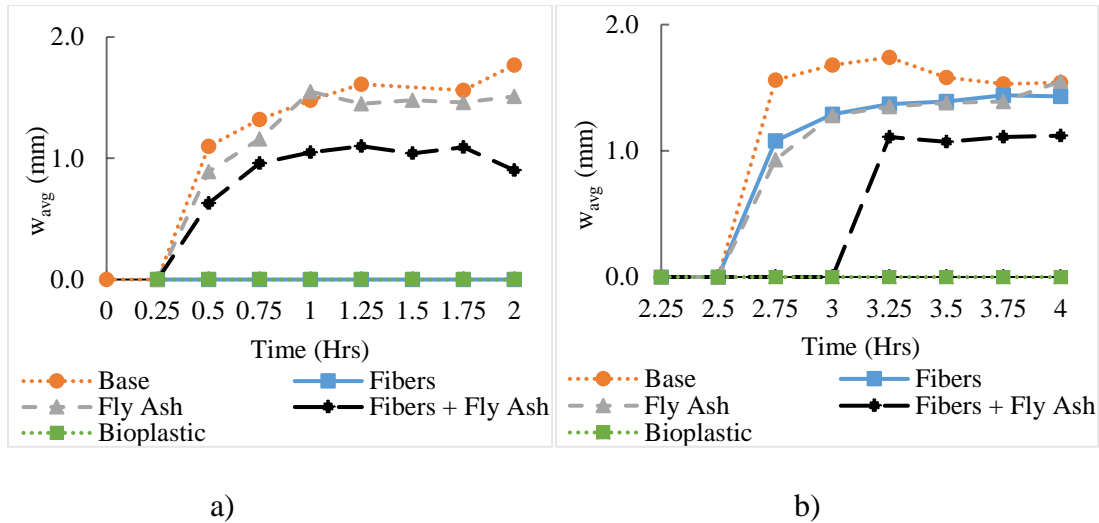
Figure 5.7 The effect of the soil improvement type on the development of the average crack width, w_{avg} in the accelerated test: a) first drying cycle; b) second drying cycle

The effect of the tested soil improvement techniques on the maximum crack width, w_{max} for the room temperature desiccation test can be observed in Figure 5.8. The motives for obtaining the maximum crack width in each specimen were twofold. First, broader cracks have a superior capacity to cause structural damage, indicating the maximum crack width represents the most significant potential for failure. Second, it provides a framework for the average crack data. For example, the fly ash sample had a w_{avg} comparable to that of the base soil. Conversely, the w_{max} of the fly ash treated sample was about 2 mm larger than the untreated soil. This implies that the fly ash treated sample most likely had a section with an unusually large crack with the rest of the cracks being thinner than the cracks in the untreated soil. The maximum crack width at the conclusion of the test for the untreated soil was 4.11 mm. The specimen treated with fly ash developed a crack geometry with a broader maximum crack width than the base soil (6.32 mm). The samples with solely carpet fibers and the carpet fibers plus fly ash hybrid technique developed

82

cracks with considerably reduced maximum widths of about 2.08 mm and 2.38 mm, respectively, at the conclusion of the testing period. Again, the specimen improved with the gelatin-based bioplastic never cracked during the entirety of the desiccation test.
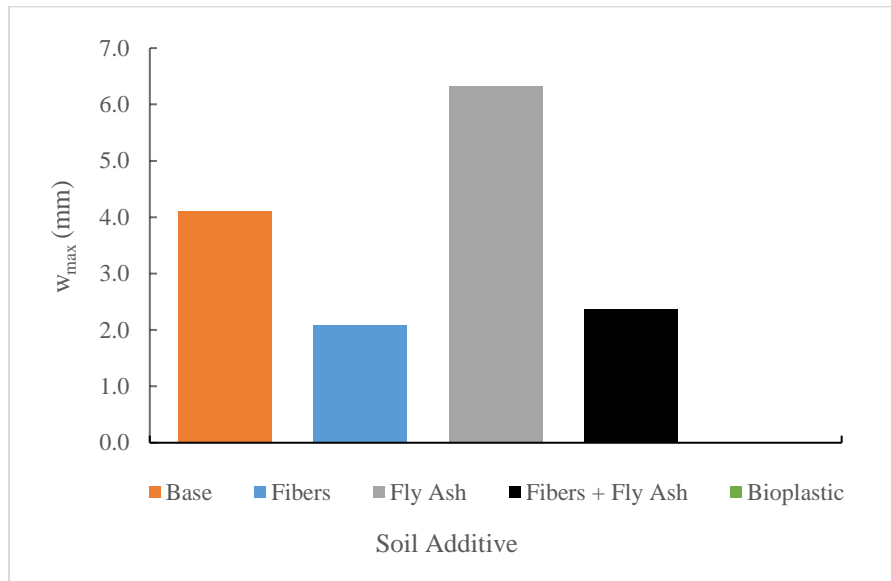
Figure 5.8 The effect of different soil improvement types on the maximum crack width, w_{max} at the 24-hour mark

The maximum crack widths over the two drying cycles in the oven desiccation test for each soil improvement method can be found in Figure 5.9. Each of the techniques lessened the maximum crack width at the completion of the testing procedure in comparison to the untreated soil but to differing degrees. Once more, the specimen with the gelatin-based bioplastic showed no changes, and no cracking of any kind occurred. The samples with both the fly ash only as well as the recycled carpet fiber showed roughly the same amount of maximum crack width reduction. Meanwhile, the specimen with the hybrid improvement technique provided additional crack reduction. In the second drying cycle, the untreated soil's maximum crack width displayed the

same soil drying phenomenon that influenced the average crack width results and gave the appearance of crack narrowing.

a)   b)
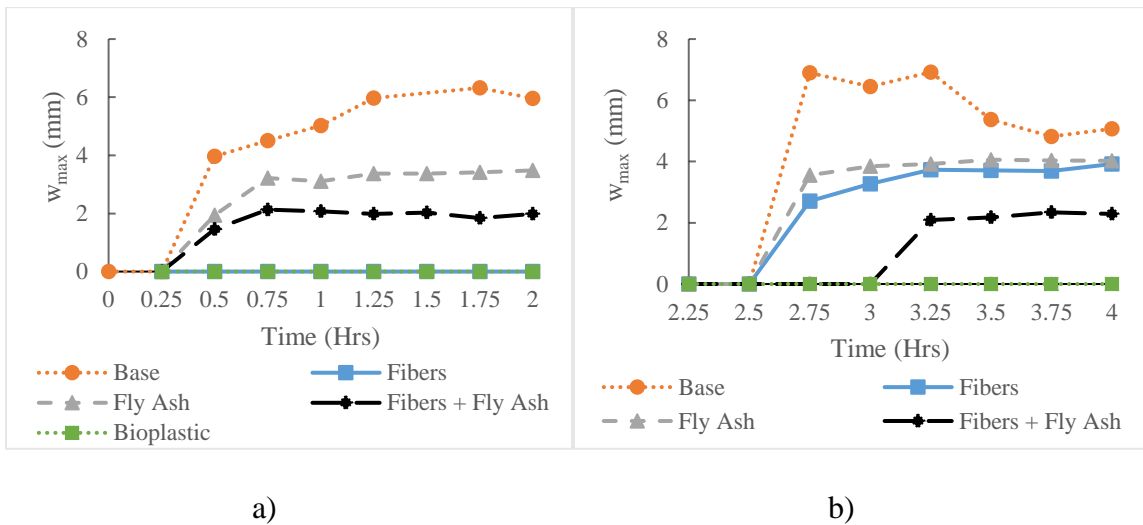
Figure 5.9 The effect of the soil improvement type on the development of the maximum crack width, w_{max} in the accelerated test: a) first drying cycle; b) second drying cycle

The *ARF* parameter was presented to quantitatively determine the effectiveness of each soil improvement method in reducing desiccation cracking in addition to the overall soil shrinkage. The effectiveness of the respective improvement techniques for the room temperature desiccation test can be found in Figure 5.10. The graph demonstrates that the untreated soil displays the largest *ARF,* and the bioplastic shows no measurable shrinkage and does not crack at all, including after 24 hours. Despite the fact that no cracks propagated in any tested samples until the 24-hour mark, the specimens still had *ARF* nonzero values as a result of lateral shrinkage of the soil before any cracking occurred. By examining the digital images, the variations in the short term were determined to be caused by discoloration in the soil surface as a result of irregular drying patterns.
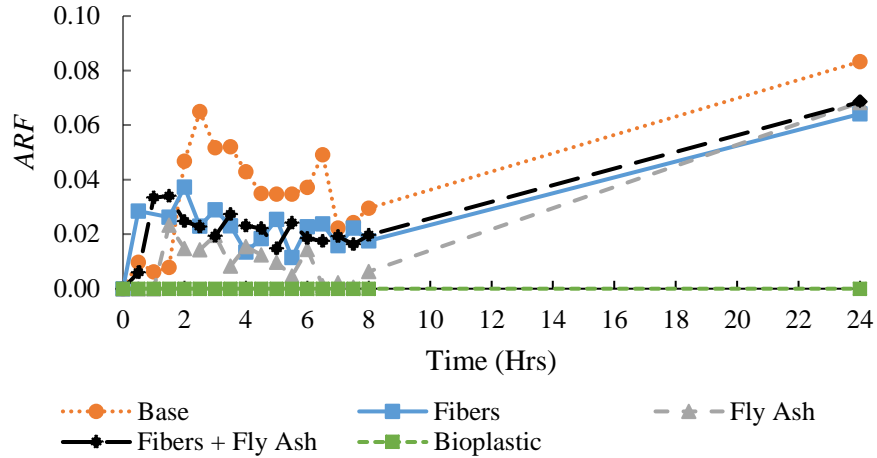
Figure 5.10 The effect of the different soil improvement type on the development of the *ARF* in the standard desiccation test.

For the oven desiccation test, data from both drying cycles in relation to the rewetting process was studied. The *ARF* results for the initial drying cycle and the second cycle after rewetting are shown in Figure 5.11 a and b, respectively. The figures demonstrate that both specimens comprising the fly ash provided minor enhancement when exposed to increased temperatures. Once more, the specimen enhanced with the gelatin-based bioplastic exhibited no alteration in the surface area even when exposed to increased temperatures.
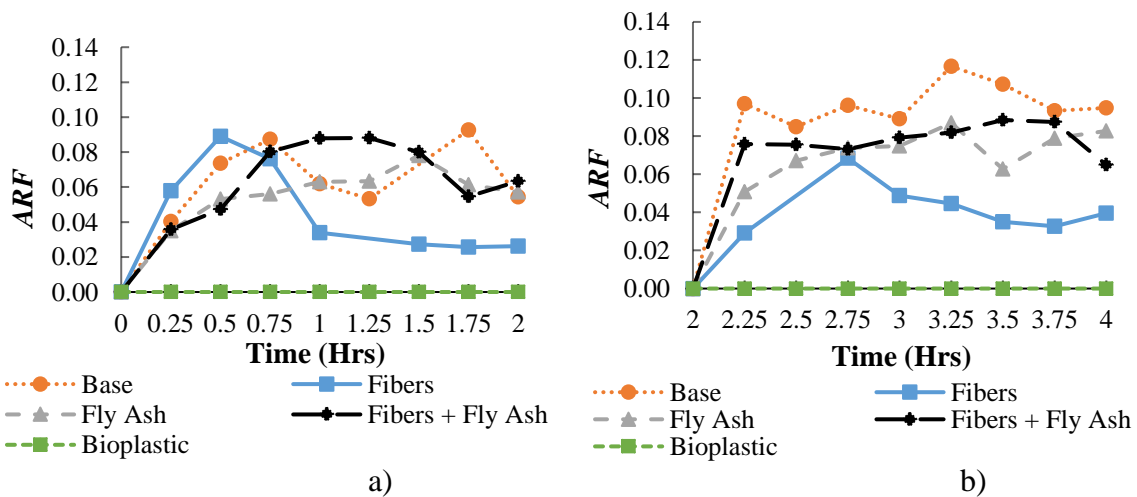
Figure 5.11 The effect of the soil improvement type on the *ARF* in the accelerated test: a) first drying cycle; b) second drying cycle

85

5.3 KAOLINITE TEST RESULTS

5.3.1 KAOLINITE DESICCATION TEST RESULTS

Using the data obtained from the GOM image analysis process, the performance of each of the selected improvement methods for the kaolinite clay was studied. The w_{max}, l_{max}, and rs_{max} were obtained for each time frame during the kaolinite desiccation test. In addition, the water content was recorded at each stage for every sample, while the suction was recorded at each stage for the first specimen tested for the untreated soil and each improvement technique. The progression of the cracking throughout the kaolinite desiccation test can be seen in Figure 5.12.
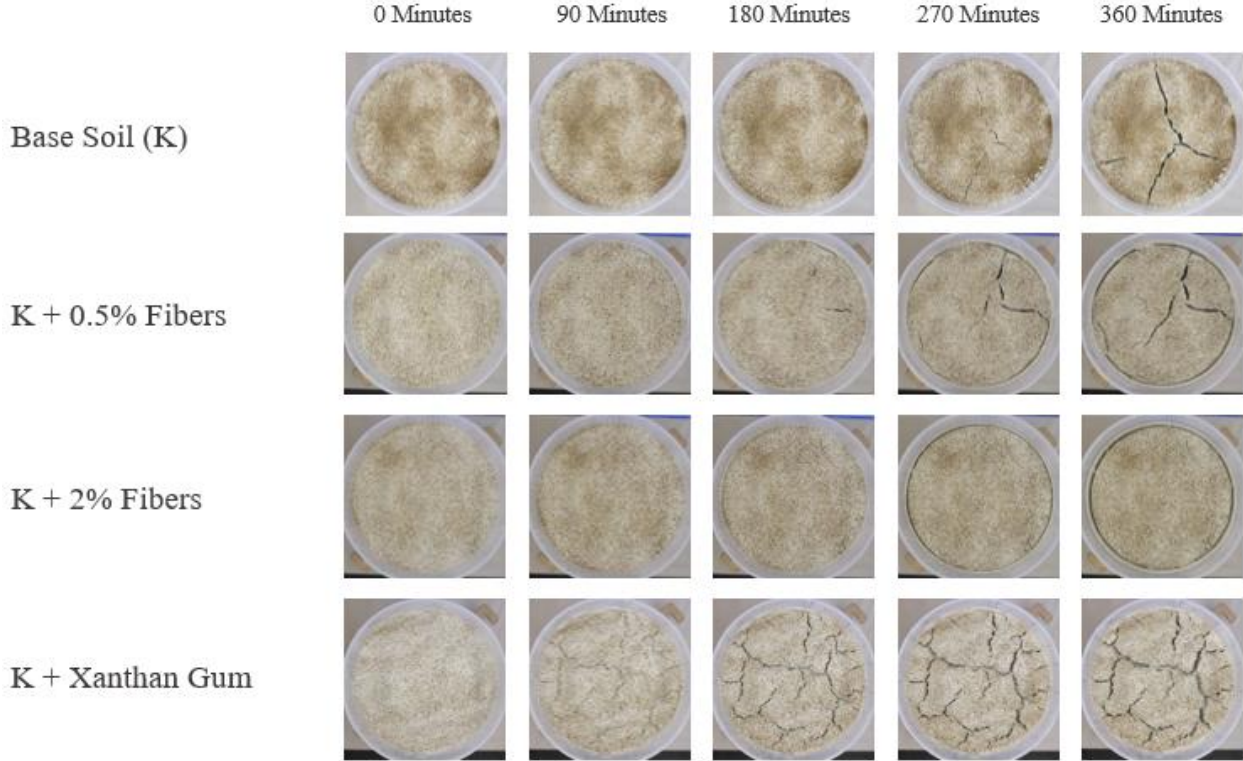
Figure 5.12 Desiccation crack test results for kaolinite test after six hours of drying

Generally, the cracks appeared at the same time with the exception of the xanthan gum aided specimens where crack initiation occurred much earlier. Each of the fiber-aided specimens first began to crack in the 4th testing period or between the 90 and 120-minute marks, the same as the untreated kaolinite clay. This suggests that the recycled fibers do not alter the crack formation process but rather retard the propagation portion of the entire desiccation cracking phenomenon. Meanwhile, the samples treated with xanthan gum cracked immediately, with each sample cracking in the first 30-minute heating interval, suggesting that the addition of the xanthan gum affected the crack formation mechanism of the clay. In general, the xanthan gum aided samples behaved in a much different fashion than each of the other kaolinite samples. Aside from cracking at an earlier time, the xanthan gum samples adhered to the sides of the mold to a much greater degree. This occurred due to the sides of the molds being heavily exposed to the heat source and the xanthan gum melting to a degree and behaving like a glue between the clay specimen and the mold.

Furthermore, the cracks themselves developed to possess very different characteristics. Whereas the untreated kaolinite samples and the fiber-treated samples cracked in similar ways, albeit with differing magnitudes, the xanthan gum-aided samples cracked in an altogether different manner. The two pictures in Figure 5.13 contrast the difference between the cracks that formed. The general form of cracking in plain and fiber-aided clay can be seen in Figure 5.13a. Here, the cracks have clearly defined edges, with mostly vertical walls. In Figure 5.13b, the cracks for the xanthan gum samples can be observed. In these samples, the cracks seem to almost have a shallow shelf and a narrow deeper second phase. Also, the edges of these cracks are not nearly as well defined and seem to have almost crumbled to some degree.

a)   b)

Figure 5.13 Comparison of cracks in kaolinite soil in: a) untreated samples b) xanthan gum aided samples

The water content was determined at time step for each specimen by recording the mass at every 30 minutes. The change in mass was considered to be the mass of water that was evaporated, causing a drop in water content. The water content generally decreased to about 40% for each improvement technique. The average water content for each improvement method can be seen in Figure 5.14.
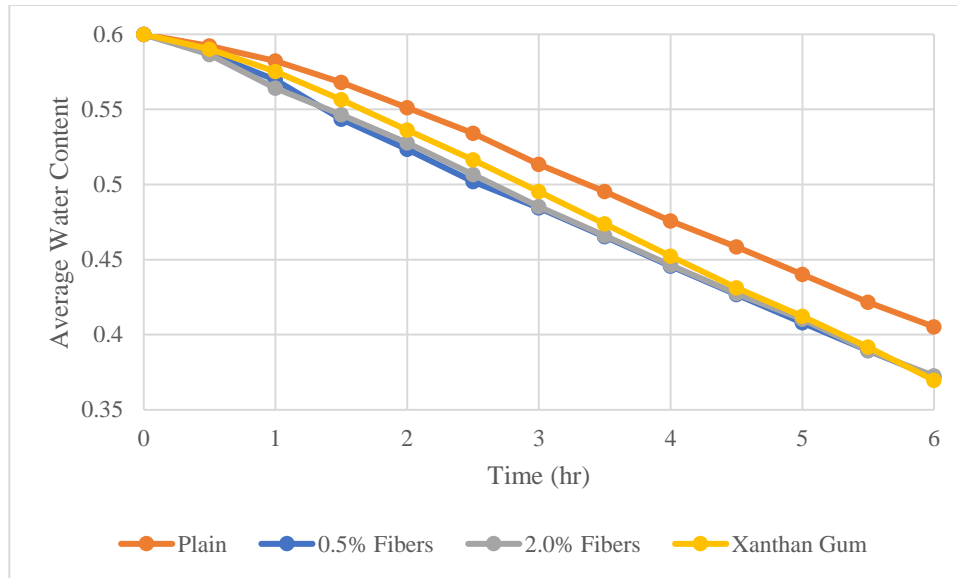
Figure 5.14 Change in the average water content during the kaolinite desiccation test

The suction was measured at each time step at three separate places for the one specimen tested for each improvement type and plain kaolinite. The change in suction versus time for each of the techniques and plain soil can be seen below (Figure 5.15 a-d). It should be noted that the improvement type had a very little if any effect on the development of suction in the samples. Notably, the placement of the tensiometers had a more significant impact on the suction measured in the specimens than the improvement technique utilized. The tensiometer in the center position (T2) generally developed the least amount of suction while the two locations on the outside of the samples generated suction of a greater magnitude.
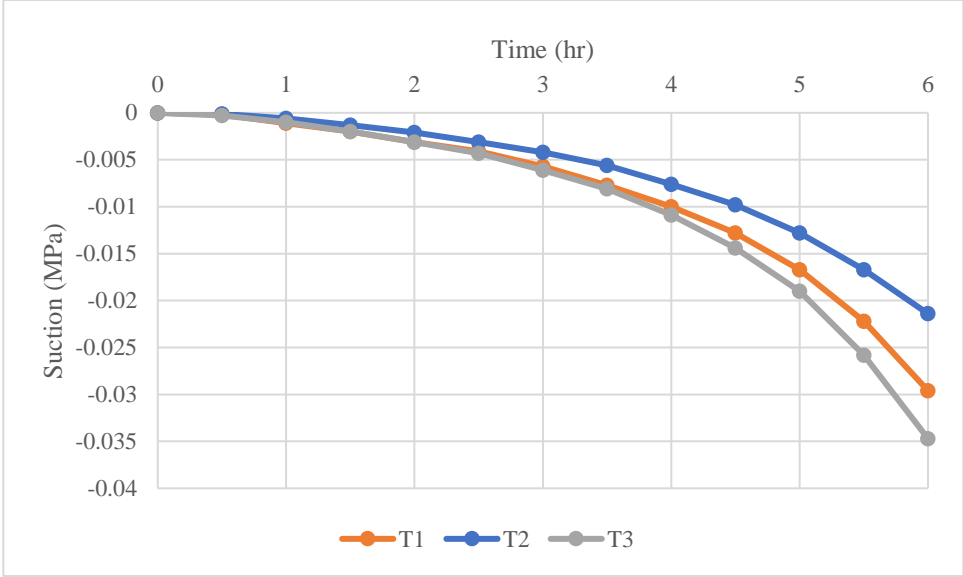
a)
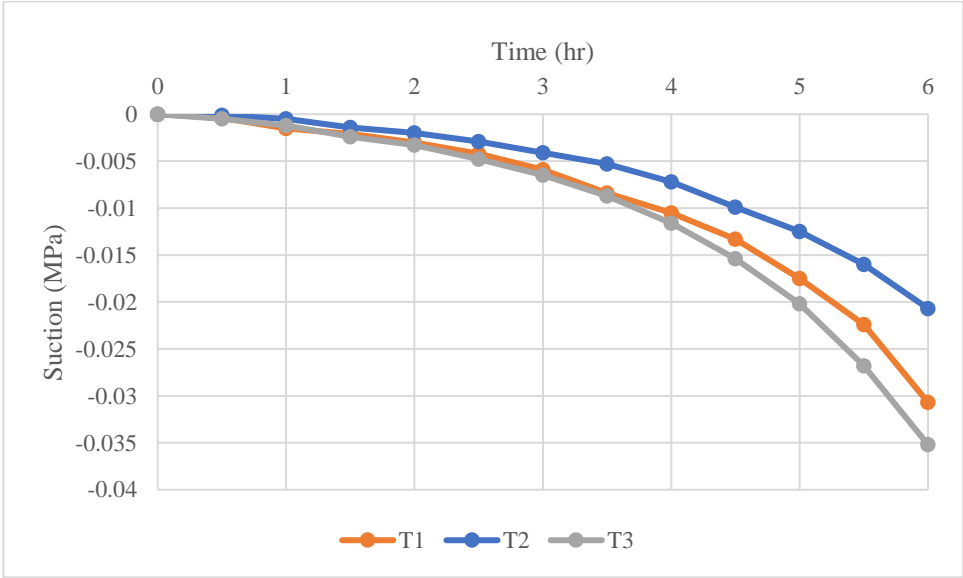
b)
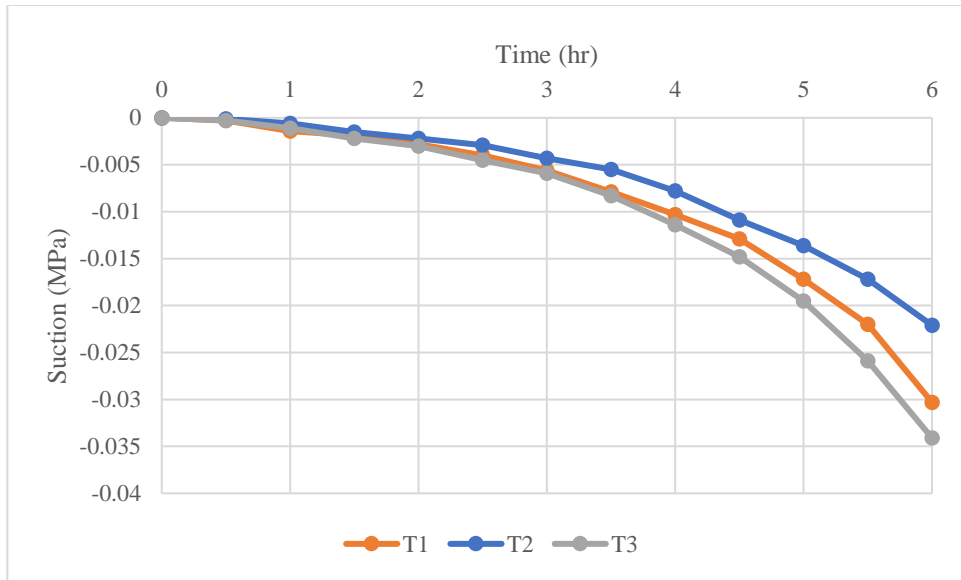
c)
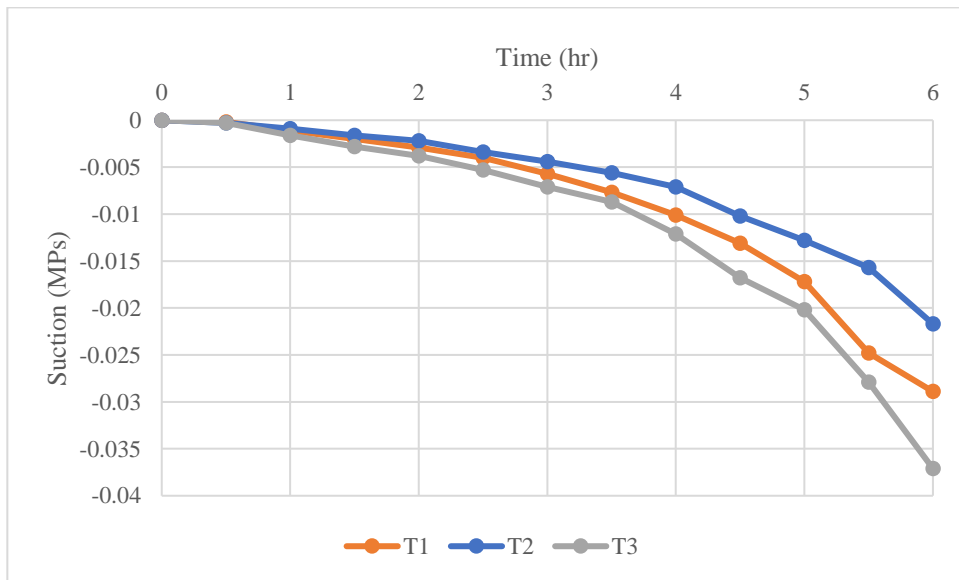
d)

Figure 5.15 Change of suction during the kaolinite desiccation test for: a) untreated soil; b) 0.5% fiber content; c) 2.0% fiber content; d) xanthan gum

The suction and water content results were used to develop a soil-water characteristic curve (SWCC). This plot can be found in Figure 5.16. Because the water contents and suction levels were fairly identical throughout the testing process, only the results from the pure kaolinite clay

were plotted for each position of the tensiometers. The SWCCs from other research projects on kaolinite clay were plotted as well. Figure 5.16 shows that while the experimental results from this research produced suction levels slightly lower than other projects[63,64], a general trend can easily be observed.
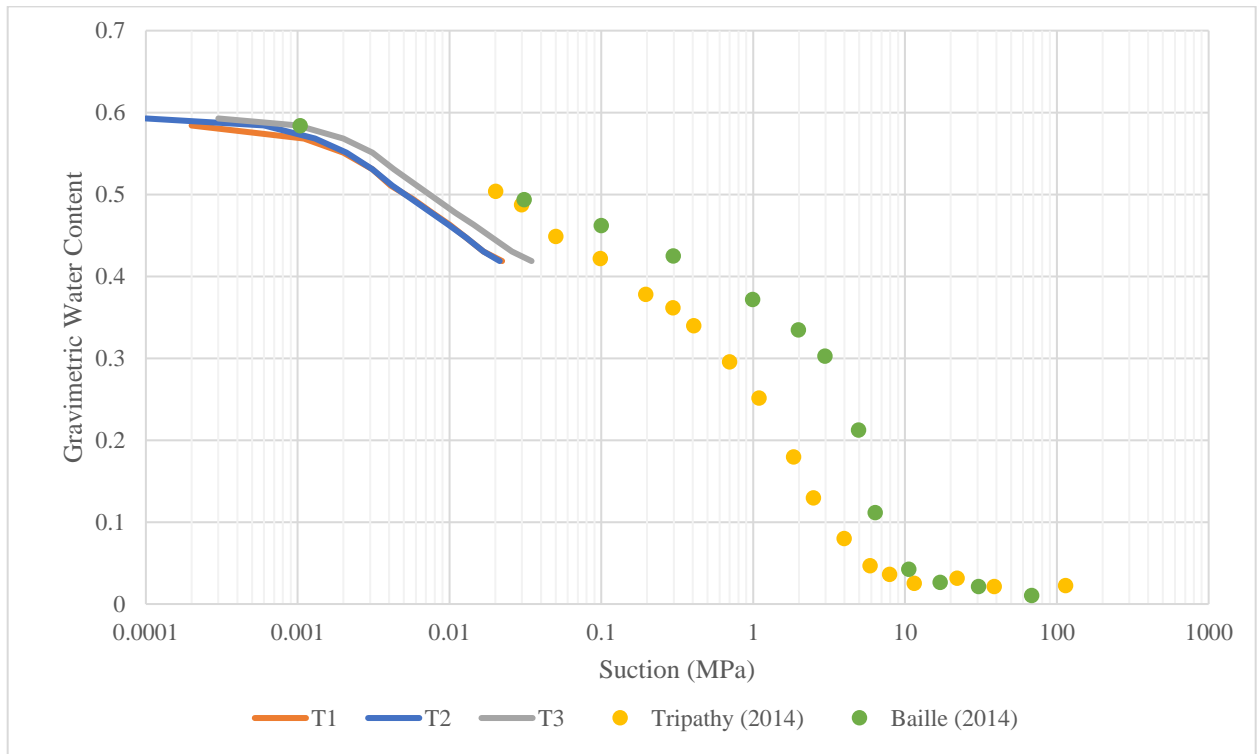
Figure 5.16 Soil Water Characteristic Curve for plain kaolinite. Other data shown for comparison[63,64]

The effect of the tested soil improvement techniques on the maximum crack width, w_{max} for the kaolinite desiccation test can be seen in Figure 5.17. The motive for obtaining the maximum crack width in each specimen remained the same as for the Piedmont soil, with broader cracks being the most significant concern due to their superior capacity to cause structural damage. Because three trials were completed, the average maximum crack width was utilized in order to minimize the effect of an outlying behavior. The maximum crack width at the end of the test for the untreated soil was 6.83 mm. The specimen treated with 0.5% fiber content developed a crack

geometry with a slightly smaller maximum crack width than the plain kaolinite clay (6.53 mm). In other words, the progression between the untreated kaolinite and the samples treated with a fiber content of 0.5% was nearly identical, suggesting that the fiber content was not sufficient to alter the crack width behavior of the kaolinite significantly. Increasing the fiber content added to 2% had a much more significant effect as the maximum crack width achieved was only .65 mm. Crack growth in those samples effectively stopped after the four-hour mark, increasing by only .05 mm after that point. On the other hand, the samples treated with xanthan gum performed far worse than the untreated soil, with the cracks growing to a maximum width of 10.89 mm. In fact, at the three-hour mark, the maximum crack width exceeded the final maximum crack width for the other improvement techniques and the untreated clay.
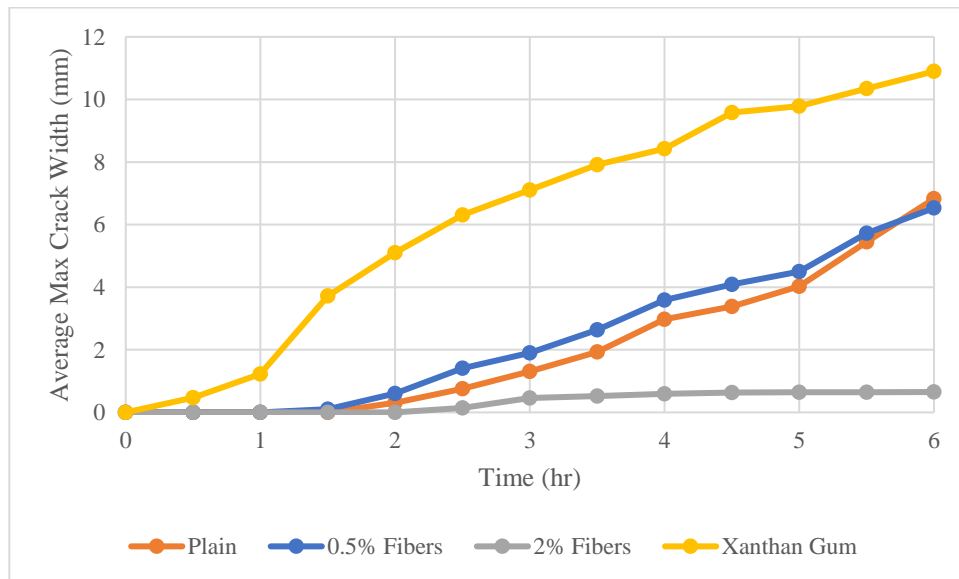
Figure 5.17 The effect of different improvement techniques on w_{max}

The effect of the tested soil improvement techniques on the average maximum crack width, l_{max} for the kaolinite desiccation test can be seen in Figure 5.18. Initially, the maximum crack length was taken to be the most prolonged individual crack, but once the crack patterns became

93

more complex, the longest continuous path in the crack network without intersecting itself was used to define the l_{max}. The reason for studying the maximum crack length in each specimen was to examine the desiccation crack network and each improvement techniques' aptitude for preventing new crack initiation. The maximum crack length at the conclusion of the desiccation test for the untreated soil was 149 mm.

The specimen treated with 0.5% fiber content developed a crack geometry with a slightly higher maximum crack length (203 mm) than the untreated kaolinite clay. While the addition of the fibers did not dramatically change the crack width growth, the soils treated with the 0.5% fiber content promoted a more extensive crack network as seen in Figure 5.12.

Boosting the fiber content added to 2% had a more dramatic effect on the soil's performance than the maximum crack width. The introduction of more fibers led to a decrease in maximum crack width by a factor of nearly 15, i.e., to 13.6 mm. Again, crack growth in those samples essentially ended after the three-hour mark, increasing by approximately .5 mm after that point.

On the other end of the spectrum, the samples treated with xanthan gum performed perhaps even worse than it did when considering maximum crack width. With a maximum crack length of 374 mm, an increase of nearly 250% over the untreated soil, the samples treated with xanthan gum created a far more extensive crack network. Moreover, after two hours, the l_{max} for the xanthan gum treated clay was more than double the final maximum crack length of the untreated kaolinite clay.
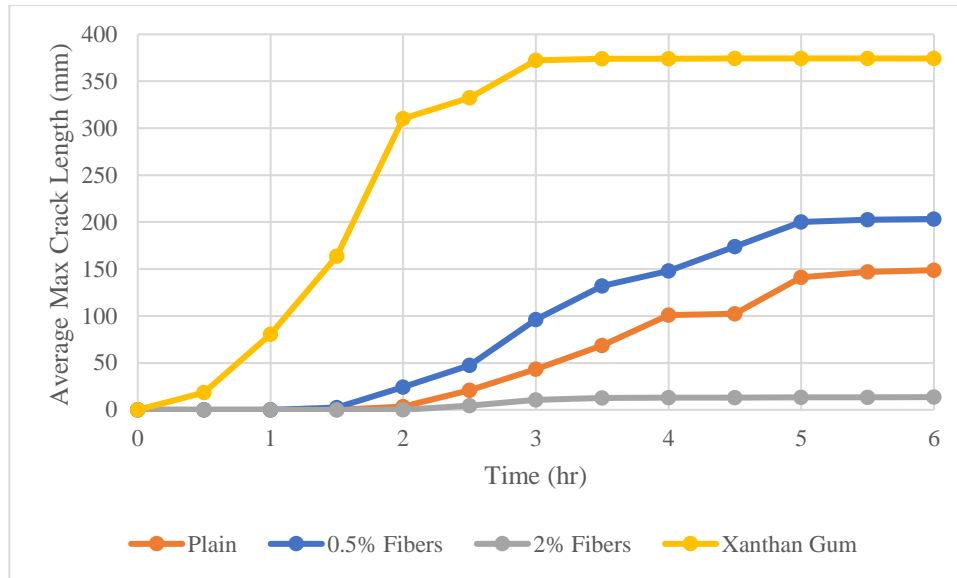
Figure 5.18 The effect of different improvement techniques on l_{max}

In addition to the cracking characteristics, GOM image processing was used to determine the effect of the different soil improvement techniques on the maximum radial shrinkage displacement, rs_{max} on the clay specimens. The results for the kaolinite desiccation test can be seen in Figure 5.19. The impetus for studying the maximum radial shrinkage in each specimen was to contrast how the specimens reacted to a loss in water content between global surface area loss and cracking behavior.

The maximum radial shrinkage at the conclusion of the desiccation test for the untreated soil was 2.25 mm. The specimen treated with 0.5% fiber content decreased in radius length at a slightly greater rate with a final maximum radial shrinkage of 3.18 mm. This shows that the inclusion of a small amount of fibers leads to a more extensive crack network and more significant radial shrinkage. While the addition of the fibers did not dramatically change the crack width growth, the soils treated with the 0.5% fiber content promoted a more extensive crack network.

Notably, utilizing the 2% fiber content method and the xanthan gum method yielded opposite results to the crack geometry results. The addition of the recycled fibers at a rate of 2% increased

the radial shrinkage of the clay to 4.10 mm. These results, combined with the minimal crack propagation of the 2% fiber specimens, suggests that the fibers were able to increase the soil's tensile strength to overcome the frictional stress on the bottom of the sample and the adhesion of the sample to the side of the molds, leading to global shrinkage instead of cracking.

Conversely, while the xanthan gum enhanced samples displayed the most expansive crack network, no radial shrinkage occurred within those specimens. Essentially, the clay in these test runs maintained contact with the plastic mold at all times and points. Further examination of the behavior of the xanthan gum-treated samples will occur in Section 5.3.4.
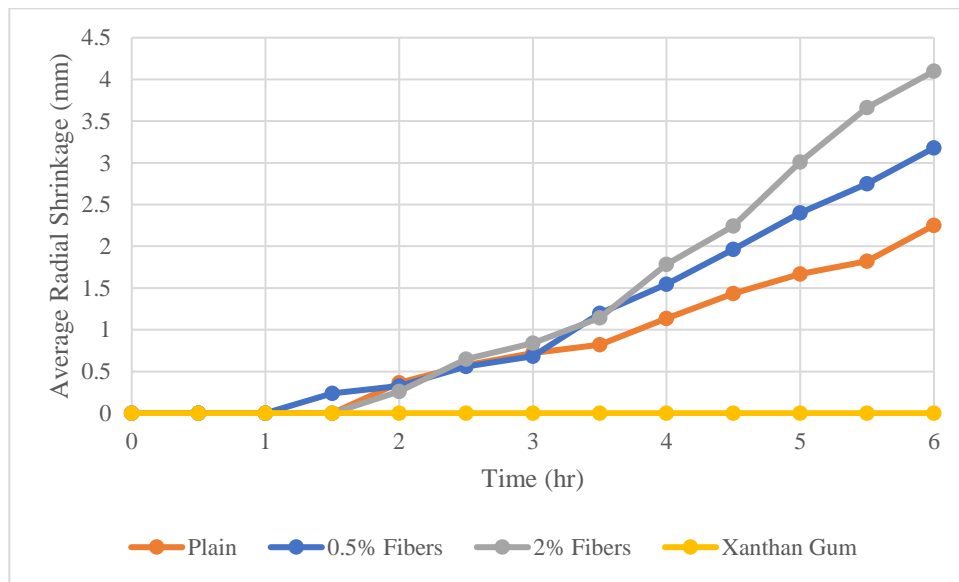
Figure 5.19 The effect of different improvement techniques on rs_{max}

5.3.2 KAOLINITE UNCONFINED COMPRESSION TEST RESULTS

In addition to desiccation tests, mechanical tests were performed to determine how the various soil improvement techniques impacted the tensile and compressive strengths of the kaolinite soil. The unconfined compression test was performed to analyze the compressive strength of the altered soil, and the results can be found in Figure 5.20. The untreated soil possessed a compressive

strength of 239 kPa. The xanthan gum aided samples yielded by far the greatest compressive strength at 937 kPa. Meanwhile, both improvement techniques containing the recycled carpet fibers only marginally improved the compressive strength with the 0.5% fiber content yielding a compressive strength of 324 kPa and the 2% fiber content producing a compressive strength of 255 kPa.

The results of the unconfined compressive test were also used to determine the elastic modulus for the soil's improved by each technique. The Young's modulus for the untreated kaolinite clay was found to be 32.4 MPa. When adding 0.5% fiber content, the elastic modulus was virtually unchanged at 31.8 MPa. Adding additional fibers actually lowered the elastic modulus considerably, with the soil containing 2% fiber content possessing a value of 16.3 MPa. On the other end of the spectrum, adding xanthan gum dramatically increased the Young's modulus to 61.4 MPa.
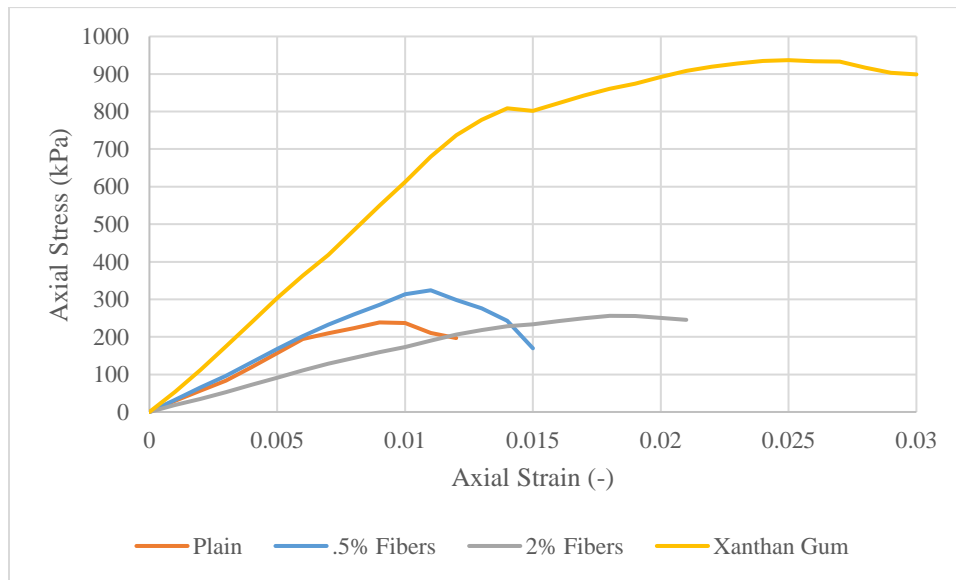
Figure 5.20 The effect of different improvement techniques on compressive strength for kaolinite soil

5.3.3 KAOLINITE INDIRECT TENSILE TEST RESULTS

In addition to the unconfined compression test, the splitting tensile test was performed, with its aim being to determine the tensile strength of the soil with the various improvement techniques. The results of this test can be seen in Figure 5.21. The untreated soil possessed a tensile strength of 123 kPa. The xanthan gum improved samples possessed by far the greatest tensile strength at 275 kPa. Meanwhile, the two improvement techniques, including the recycled carpet fibers, significantly reduced the tensile strength with the specimens with 0.5% fiber content yielding an average tensile strength of 47 kPa and the 2% fiber content specimens producing a tensile strength of 76 kPa.
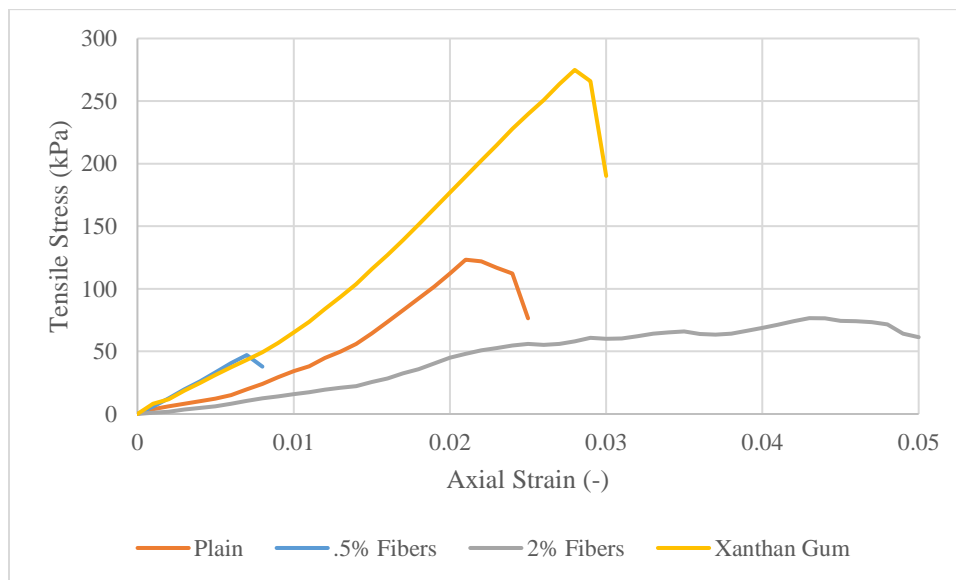
Figure 5.21 The effect of different improvement techniques on tensile strength for kaolinite soil

5.3.4 KAOLINITE TEST DISCUSSION

Two specific results from the kaolinite soil testing process are worth closer examination considering their deviation from their expected outcomes. First, the addition of the xanthan gum increasing the cracking behavior of the soil was quite unexpected. This is especially true when

considering the result from the mechanical testing, where the addition more than doubled the tensile and compressive strengths of the untreated soil. The reason for this most likely resides in the residual shrinkage data. While every other soil tested shrunk away from the mold, the specimens with xanthan gum did not experience any movement away from the mold at any point along their contact faces. This suggests that the xanthan gum potentially increased the adhesion between the mold and the soil to the point where the soil cracked rather than moved away from the mold.

The second set of results worth further analysis is the behavior of the fiber aided samples in the mechanical tests. While the fibers were expected to increase both compressive and tensile strength, they yielded little impact on compressive strength and dramatically decreased tensile strength. When observing the specimens that were tested, it was clear that the fibers actually created discontinuities in the specimens due to their size in relation to the size of the soil cylinders. Whereas the fiber's length was 1/23 of the diameter of the specimen in the desiccation test, the length of the fibers was closer to 1/3 of the diameter of the mechanical specimens. In addition, the compaction method could often leave fibers exposed on the outside of the specimen, as seen in Figure 5.22. This effectively created a failure path in these specimens and pre-existing damage on the face of the soil. Because of these issues, the results from the mechanical tests for the fiber-aided specimens were not taken into account when determining the material properties used in the modeling process.
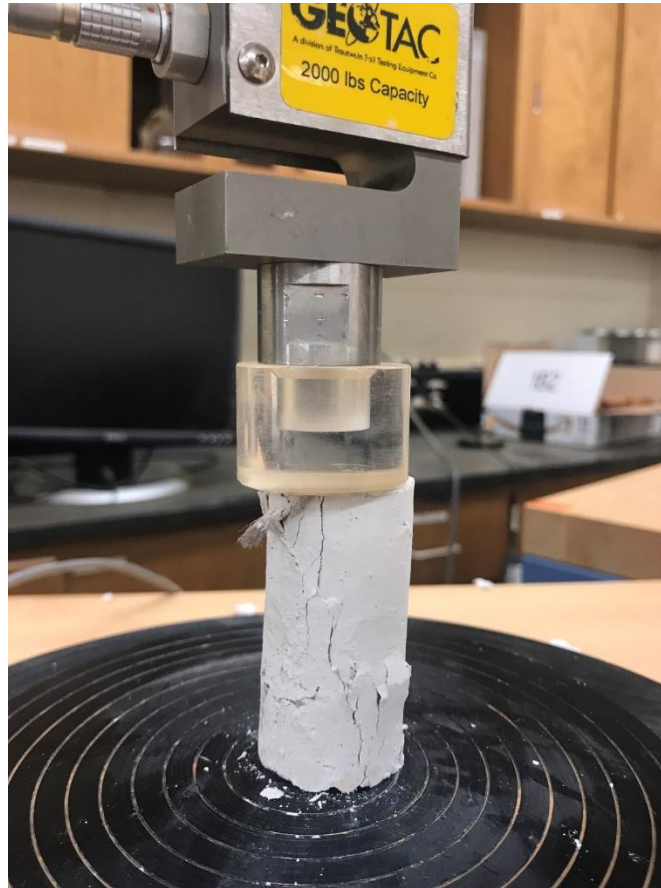
Figure 5.22 Example of fiber affecting the structural integrity of the specimen during the unconfined compression test

5.4. MODEL MATERIAL PROPERTIES AND INPUT PARAMETERS

In order to employ the combined analytical-numerical hydromechanical model detailed above, several kaolin clay material properties and environmental factors were required. The following is a description of how these values were obtained for the untreated soil and each improvement technique. Several of the untreated soil material property relationships were obtained from the work of Stirling on clay with similar plastic and liquid limits[65].

5.4.1 SOIL SURFACE FLUX CONDITION

The soil surface evaporation flux was assumed to be constant based on the linear results from Figure 5.14 across all tests. It was determined by:

$$q_a = \frac{\Delta V_w}{A_s t_d}$$

Equation 5-1

where ΔV_w is the change in water volume in the soil, A_s is the surface area of the soil specimen face, and t_d is the test duration in hours. The change in the water volume, ΔV_w was determined by taking the average mass water loss across all the specimens and averaging it. Doing so returned a soil surface flux condition of 0.0925 cm/hr.

5.4.2 VAN GENUCHTEN SHAPING CONSTANTS

The van Genuchten empirical constants were determined to be constant for all soil improvement techniques. The saturated volumetric water content, θ_s was determined to be 0.77 from the initial water content in the physical desiccation tests. The residual volumetric water content, θ_r was determined by experimental data on similar soils[63,64] and was found to be zero. The remaining parameters were determined based on the by taking the SWCC curve returned from the physical experiments and fitting the van Genuchten water content equation to the data. This yielded a value for α of 0.008478 cm^{-1}, n_G being 1.4228, and a corresponding m_G of 0.29716. The SWCC curve based on these fitted constants can be seen in Figure 5.23 Fitted SWCC with experimental data and other research. The fitted curve was converted to gravimetric water content to match both the experimental data and other research.
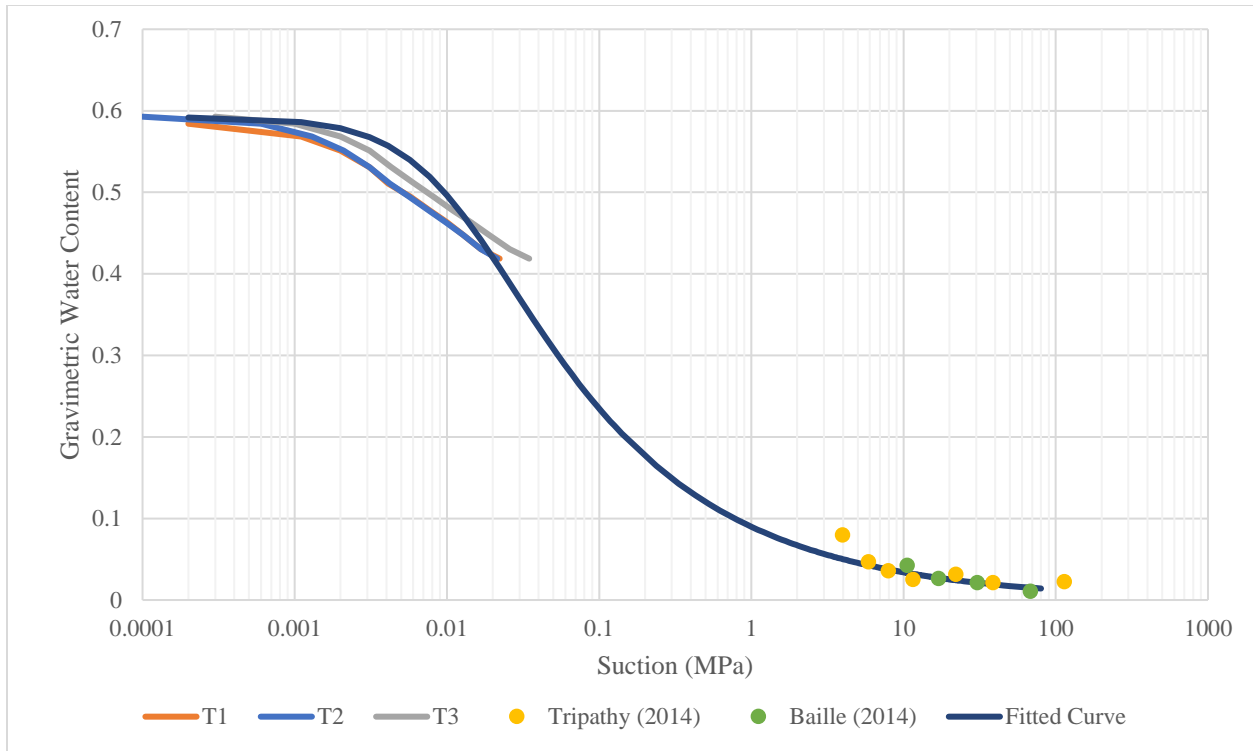
Figure 5.23 Fitted SWCC with experimental data and other research used for regression[63,64]

5.4.3. HYDRIC CONSTANT

The hydric constant is the ratio of radial shrinkage strain and water content loss (Equation 4-30) and was determined by calculating the slope of the experimental data of the radial shrinkage strain and water content loss relationship. Since the soil additives affect the radial shrinkage, the hydric constant was different based on the additive. Because the xanthan gum sample did not separate from the mold wall, a hydric constant for xanthan gum could not be determined and was assumed to be the same as the untreated soil. The hydric constant for untreated soil was found to be .1774 (Figure 5.24). Only results for two tests could be used because one trial never separated from the wall.
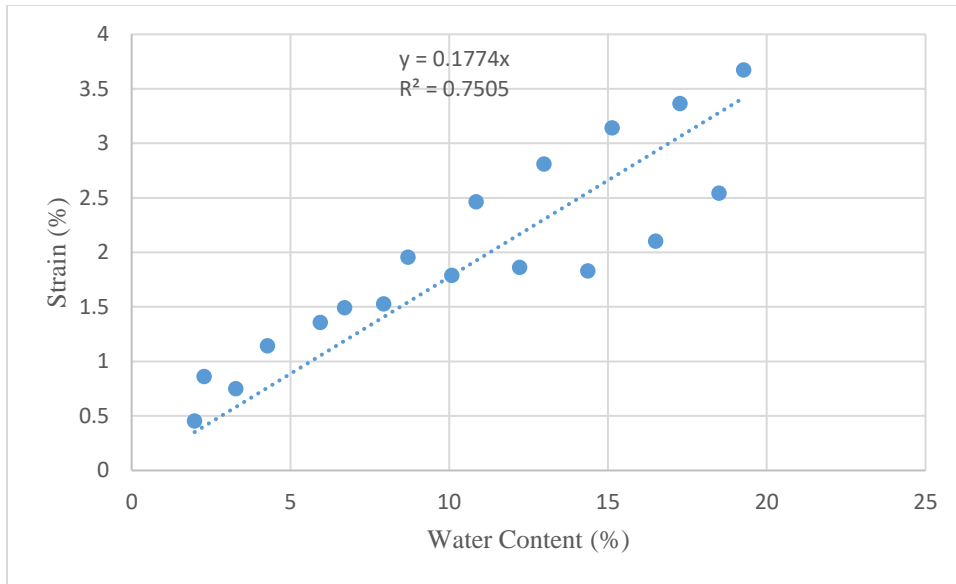
Figure 5.24 Hydric constant derivation for untreated soil

The hydric constants for the 0.5% fiber-aided soil was found to be .1934 (Figure 5.25).
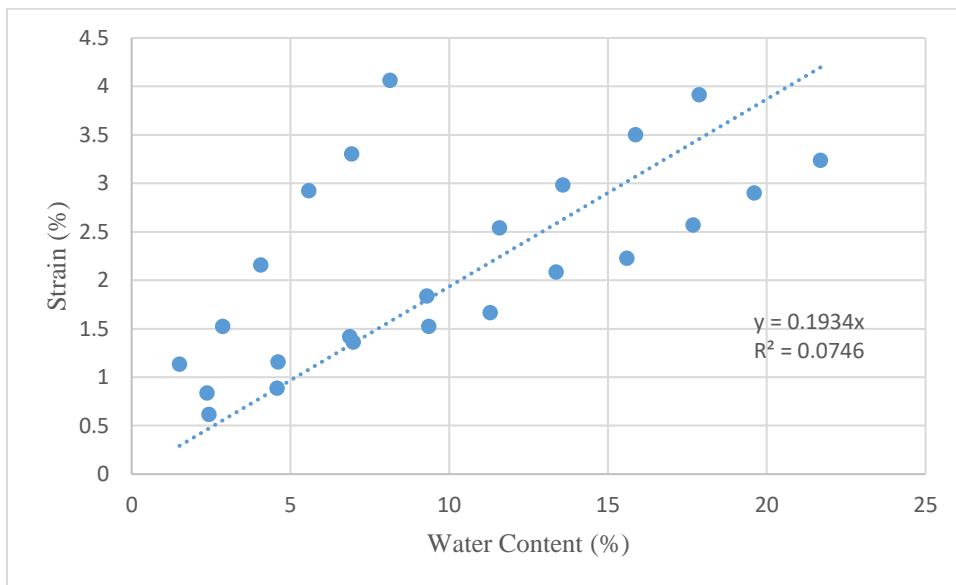
Figure 5.25 Hydric constant derivation for 0.5% fiber treated soil

The hydric constants for the 2.0% fiber-aided soil was found to be .2665 (Figure 5.26).
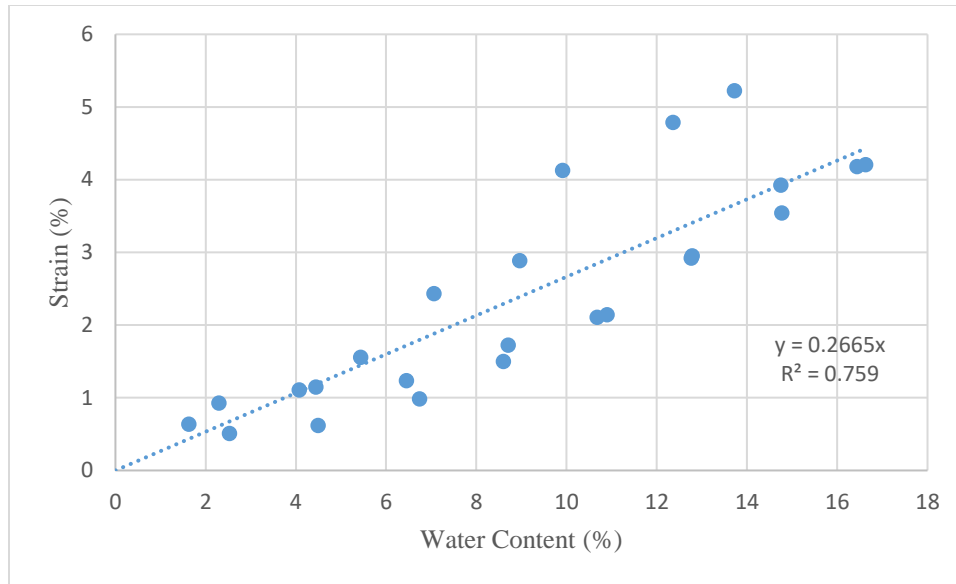
Figure 5.26 Hydric constant derivation for 2.0% fiber treated soil

These figures display varying uncertainty in the linear relationship used to obtain the hydric constant. The 0.5% fiber content relationship in particular showed significant uncertainty. As a result, a sensitivity analysis was performed to examine how altering the hydric constant affects crack initiation and can be found in Section 5.6.3.

5.4.4. YOUNG'S MODULUS

For the untreated soil, the Young's modulus was considered to be a function water content based on experiments done in previous work on similar soil[65]. The experimental values for Young's modulus from previous[65] and current research created a piecewise function that can be seen below:

$$E = \min(30000\theta^{-5.26}, 32.375) \, MPa \qquad \text{Equation 5-2}$$

In this study, it was assumed that the fibers did not affect the Young's modulus. Experimental data showed that Young's modulus is not increased due to addition of fibers[66], while other research[67]

indicate that both the type and volumetric content of fibers only slightly affect Young's modulus of cohesive soil. Results obtained in this study (Figure 5.20) indicate that the 0.5 % of volumetric fiber content does not affect Young's modulus of kaolinite, while the results of 2% are flawed. Thus, the same relationship between the Young's modulus and water content was used (Equation 5-2) for the fiber-reinforced clay samples. The relationship between the Young's modulus and water content for the untreated soil can be seen in Figure 5.27.

.
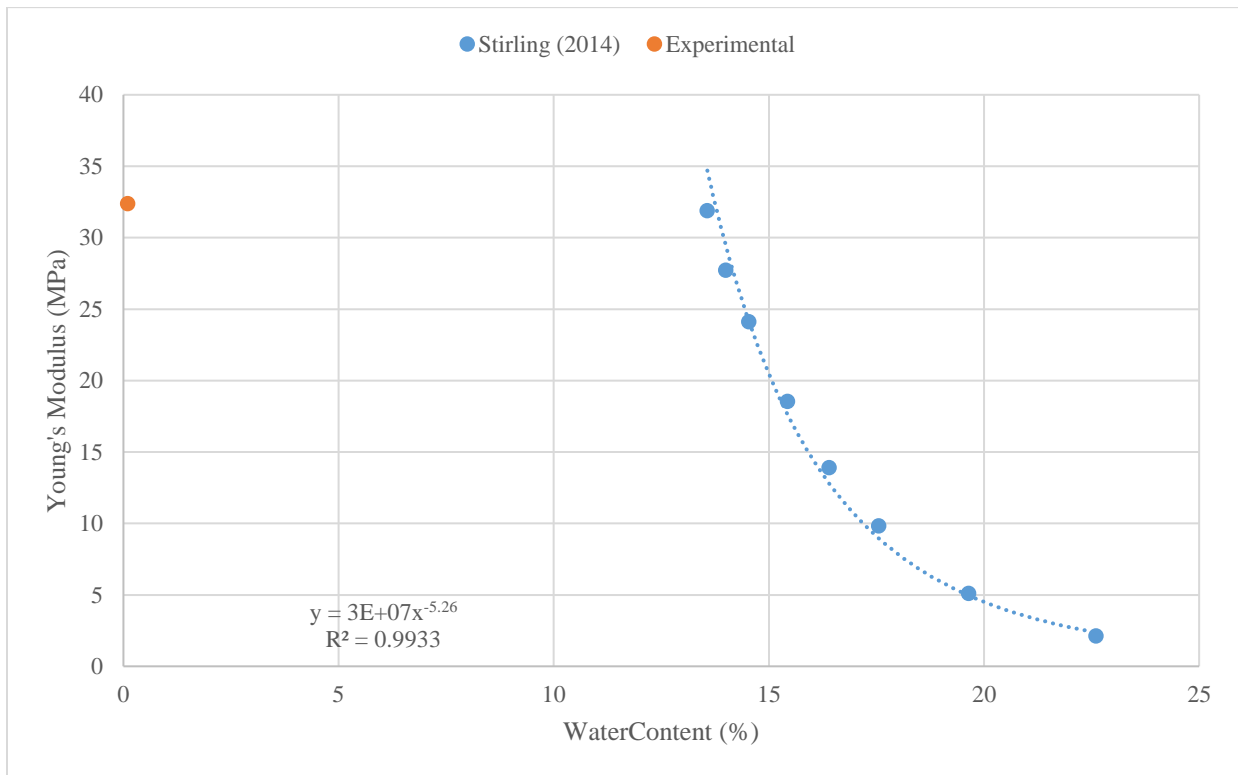
Figure 5.27 Young's Modulus determination for untreated soil with other data used for regression[65]

The Young's modulus for the xanthan gum aided specimens was altered by increasing the values in Figure 5.27 by 1.896, i.e., by the factor that Young's modulus was increased on the dry

unconfined compression test by adding xanthan gum. The relationship for the xanthan gum-improved specimens is given by:

$$E = \min(56880\theta^{-5.26}, 61.378)\ MPa$$

Equation 5-3

The graph of Young's modulus for the xanthan gum-treated soil can be seen in Figure 5.28.
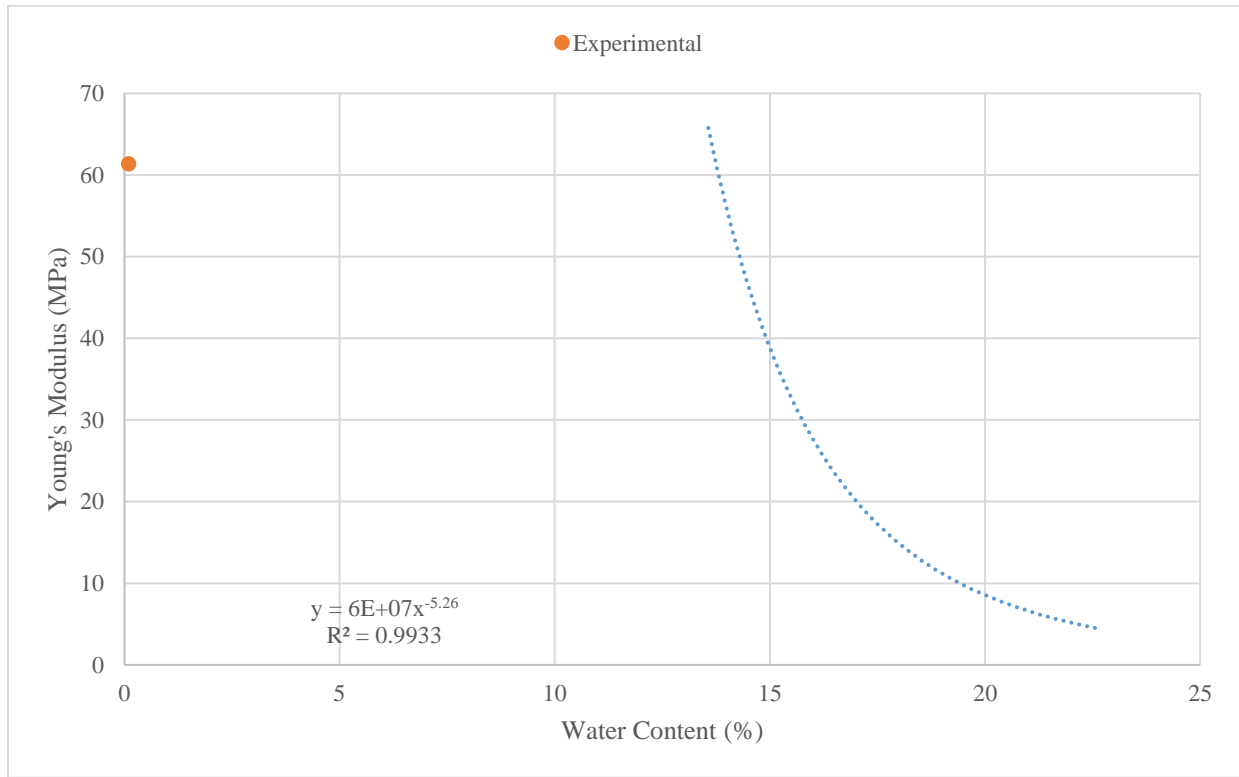
Figure 5.28 Young's Modulus determination for xanthan gum treated soil

5.4.5 TENSILE STRENGTH

The tensile strength of soil significantly depends on the water content[65], soil improvement type and amount. The relationship between the tensile strength and water content of the untreated soil was determined based on results of tensile tests on similar clays at higher water contents[65] and

106

the experimental values for tensile strength based on the results from the splitting tensile test done in this research for lower water contents. Fitting the data produced a relationship between water content and tensile strength (σ_t):

$$\sigma_t = 165.28e^{-.086\theta}$$

Equation 5-4

This relationship is based on the trend found in Figure 5.29.
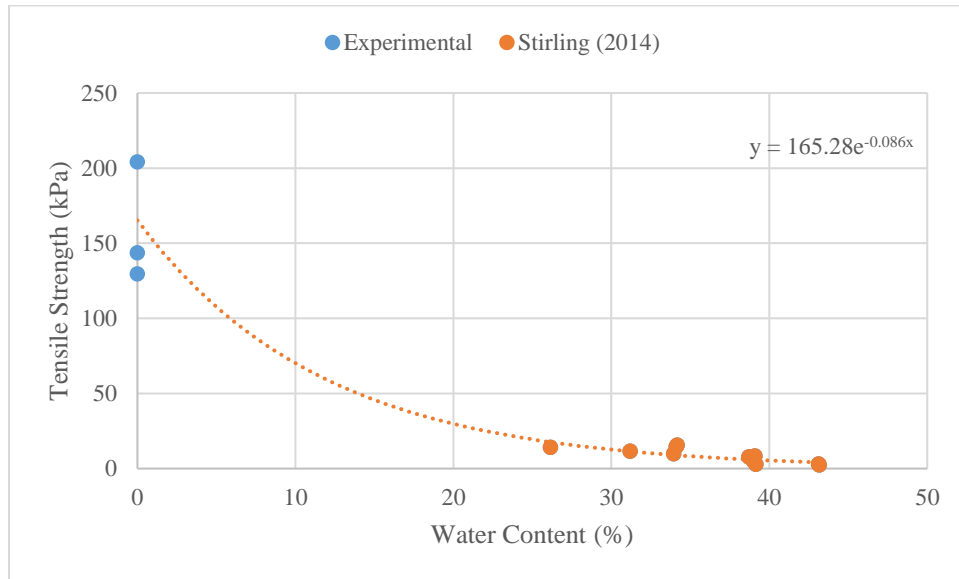
Figure 5.29 Tensile strength determination for untreated soil with other data for regression[65]

For the soils improved with fibers, it has been shown that there is a linear relationship between fiber content and tensile strength based on dry density[68]. As can be seen in Figure 5.30, for a dry density of 1.4 g/cm^3, the tensile strength of the fiber-aided soil increases in tensile strength at a rate of 1.632 kPa per additional percent of fiber content.
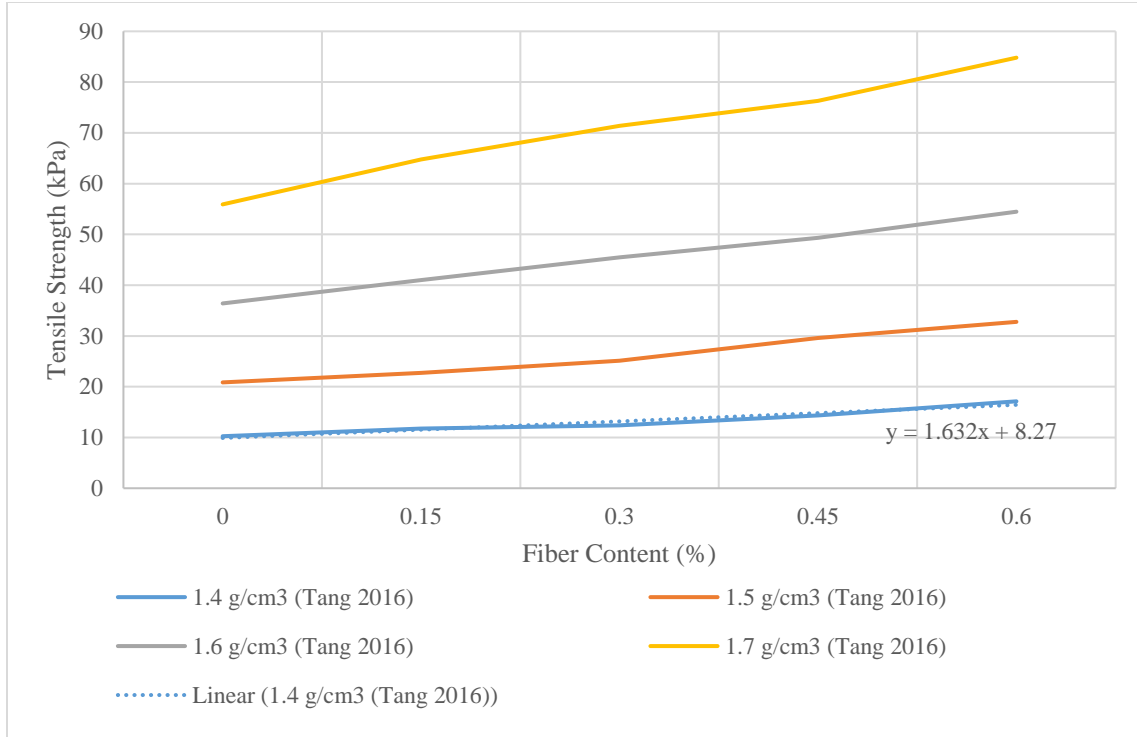
Figure 5.30 Tensile strength determination for fiber treated soil with other data used for regression[68]

For the purposes of this research, the y-intercept for this relationship was considered to be the tensile strength for the untreated soil obtained in Figure 5.29. This further produces the relationship between the water content, fiber content (F), and tensile strength ($\sigma_{t,f}$):

$$\sigma_{t,f} = 269.74 F e^{-.086\theta}$$

Equation 5-5

where F is the fiber content as a percentage.

For the soils amended with xanthan gum, a similar approach to addressing Young's modulus for specimens treated with xanthan gum was taken. The tensile strength for the xanthan gum-improved specimens was altered by increasing the values in Figure 5.31 by 2.08, i.e., the factor that tensile strength was increased on the dry splitting tensile test by adding xanthan gum.

The relationship between the tensile strength (σ_{tx}) and water content for the xanthan gum-improved specimens can be found in the equation below:

$$\sigma_{tx} = 347.84e^{-.086\theta}$$

Equation 5-6

The graph of tensile strength versus water content for the xanthan gum-treated soil can be seen in Figure 5.31.
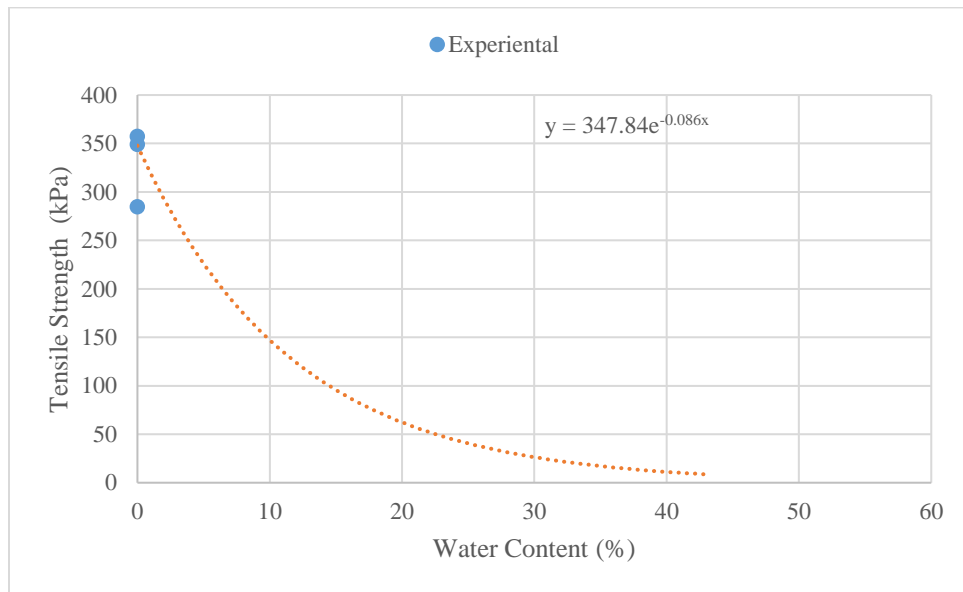
Figure 5.31 Tensile Strength determination for xanthan gum treated soil

5.4.6 INTERFACE SHEAR STRENGTH

The interface shear strength between the soil and plastic mold was assumed to be constant for all soil improvement techniques except xanthan gum. The interface shear strength was determined by shearing the soil specimen across a steel contact plane. Little research has been done on the interface shear strength between plastic and soil. As a result, steel was used as a substitute due to its relatively high smoothness. The interface shear strength for a similar clay as a function of water content in clays has been demonstrated to take the form of [65]:

$$\tau = 3.15 + \frac{-2.85}{1 + .062\theta^{7.5}}$$

<div align="right">Equation 5-7</div>

Due to the nature of xanthan gum, a different approach was required for the interface shear strength determination. The elevated temperatures during the experiment have led to xanthan gum melting, drying, and subsequently adhering to the base of the mold. Other research has shown that adding 0.5% xanthan gum to cohesive soil increases shear strength to approximately 30 kPa or nearly 10 times the level measured in the untreated soil[69]. To account for the additional xanthan gum content, a linear relationship was assumed and increased further by a factor of 2.

5.4.7 INTERFACE ADHESION

The adhesion at interfaces between two materials is strongly affected by the type of the adjoining materials. In this study, the interface adhesion was determined to be a function of the interface shear strength, which is similar to the approach when determining the adhesion to sheet walls considering soil type and wall type during deep foundations design[70]. For this clay and mold wall type, the interface adhesion between the clay and vertical mold wall was obtained by reducing the interface shear strength by a factor of four[70]. The same approach and factor were used for all specimens treated by fibers as well. Once more, the behavior of the xanthan gum amended soil was treated in a different manner. The walls had even greater exposure to the heat source, as they were directly heated, which led to even higher bonding on the walls. Other research has shown that adding 0.25% xanthan gum to cohesive soil increases adhesion strength to nearly 20 times the level measured in the untreated soil[69]. To account for the additional xanthan gum content, a linear relationship was assumed and increased further by a factor of 4. Therefore, the interface adhesion was increased by a factor of 80 over the adhesion of the untreated soil rather than reducing it.

5.5. HYDROMECHANICAL MODEL RESULTS

5.5.1 HYDRAULIC MODEL RESULTS

With the process described in Chapter 4 and coded into MATLAB, both hydraulic and mechanical results were obtained for each improvement technique. Figure 5.32 depicts the suction along the depth of the soil layer, with the time step representing each 30-minute increment shown. As can be seen in Figure 5.32, the magnitude of the suction experienced in the clay specimen increases with each time step while decreasing as depth increases. For instance, the suction at the soil's surface changed by -9 kPa during six hours, while the change in suction at the bottom of the layer was only -.96 kPa.
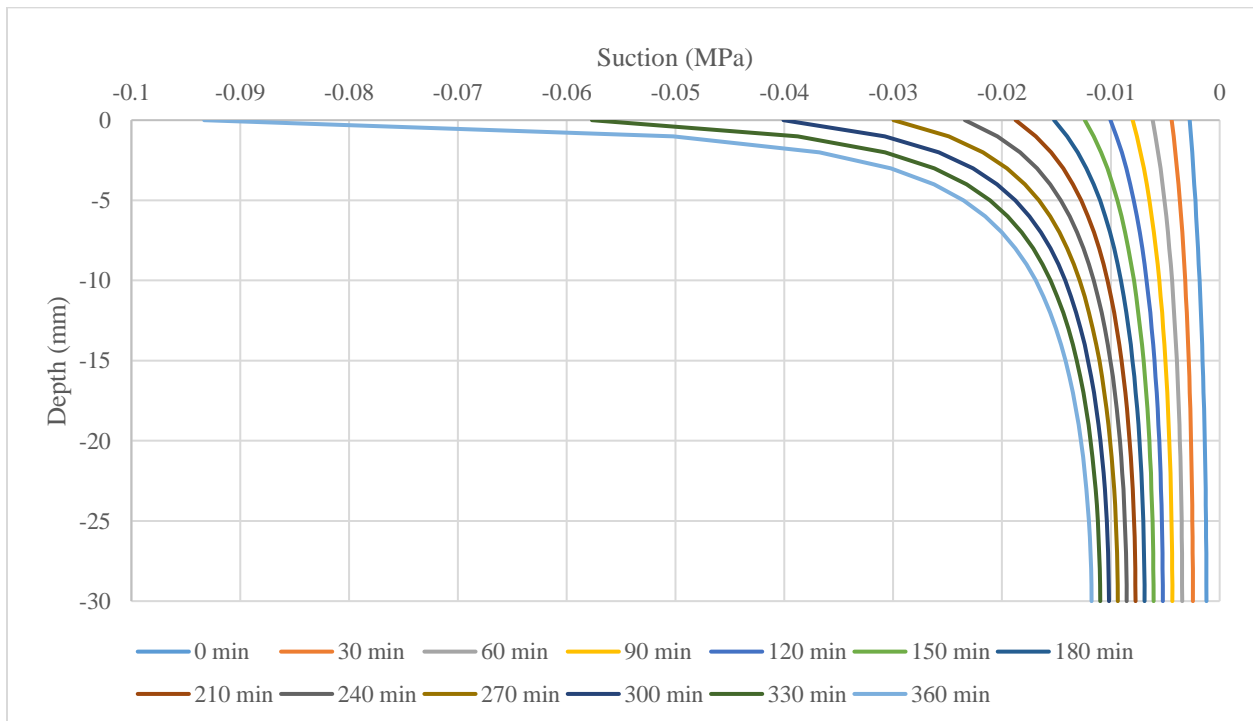
Figure 5.32 Suction as function of depth and time in hydromechanical model

Creating a water content field across the depth of the clay layer for each time step was the most valuable result calculated by the hydraulic model due to water content being an input in the

model coupling process. As such, the gravimetric water content along the depth of the soil layer was plotted, with the time step representing each 30-minute increment shown. As can be seen in Figure 5.33, the magnitude of the water content existing in the clay specimen decreases with each time step while increasing as depth increases. The water content at the soil's surface changed by -.33 during six hours, while the change in water content at the bottom of the layer was only -.1. The observed trend is expected as the water could only evaporate the clay specimen through the top soil surface, making the water content at that point the lowest at all times. This also reflects the suction behavior because unsaturated soil mechanics dictates that a decrease in water content increases the soil suction.
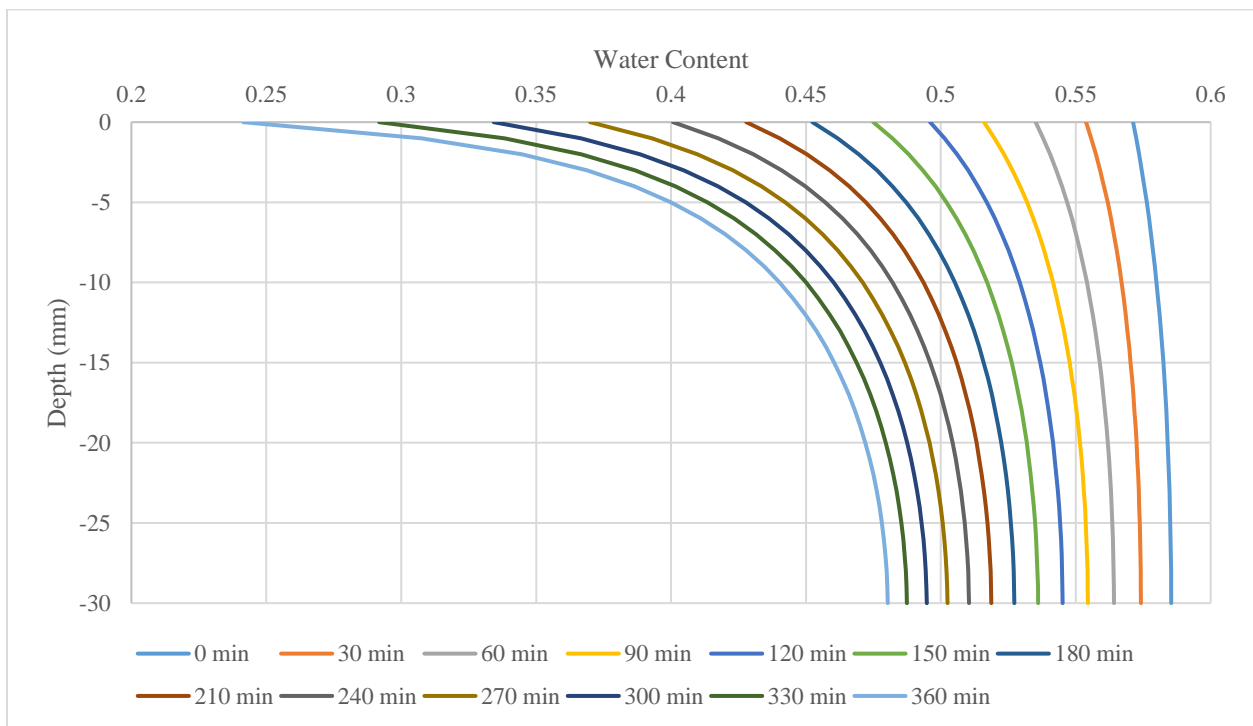
Figure 5.33 Water Content as function of depth and time in hydromechanical model

112

5.5.2 MECHANICAL MODEL RESULTS

After the hydraulic model was executed, the water content at each time and depth was input into the mechanical model for each soil improvement technique. Doing this allowed for the stresses at each point in the model's profile to be calculated during the six-hour time period. The obtained data was then compared to the soil's material and interface properties to determine the onset of desiccation cracking at different points in time, depth, and radial distance. Based on the stress formulation in Section 4.4, the stresses produced at the center of the soil would always be equal to or greater than at any other point in the clay profile. As a result, this position in the soil layer was considered to be the critical one. Figure 5.34 shows how the stresses and governing material and interface properties progressed with time for the untreated soil at the center of the soil surface. At the center of the soil specimen, radial and hoop stress are identical and therefore overlaid in the figure.
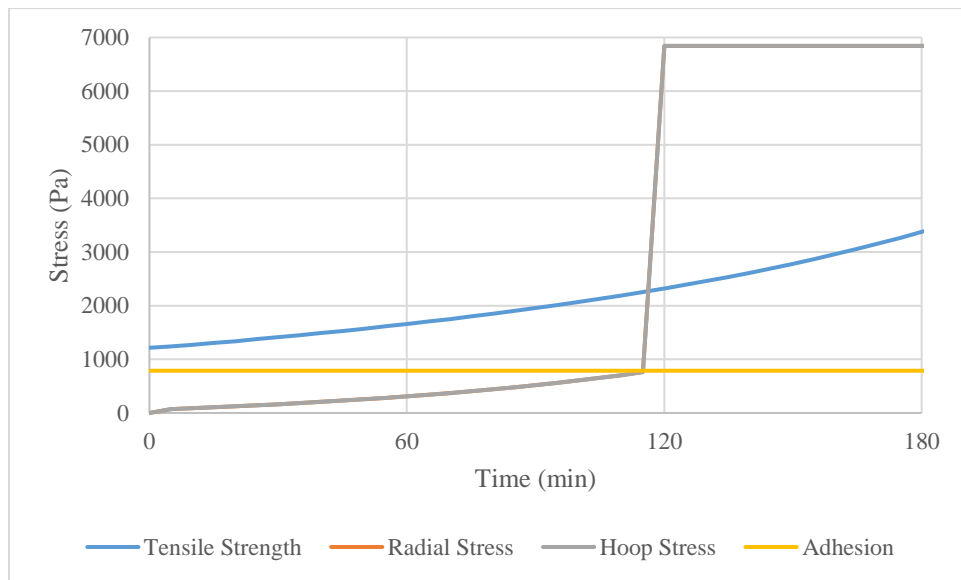
Figure 5.34 Stress progression at center of untreated soil surface over time

Furthermore, it can be seen from Figure 5.34that at the 115-minute mark, the pre-wall crack radial stress reaches the adhesion value. This means that the edge crack has formed, and therefore the specimen has detached from the wall. At this point, the radial and hoop stress calculations switch to the post-wall crack formulations, resulting in an immediate jump in hoop and radial stress. This jump increases the stresses to such a degree that the tensile strength of the soil has also been surpassed, meaning that desiccation cracking will initiate.

The stress distribution at the time of crack initiation across the depth of the center of the clay layer has been plotted in Figure 5.35. The plot shows that the tensile strength and adhesion are only surpassed by the stresses experienced in the soil at the very top of the clay layer. Again, the radial and hoop stress are identical at the center of the specimen and overlaid in the figure
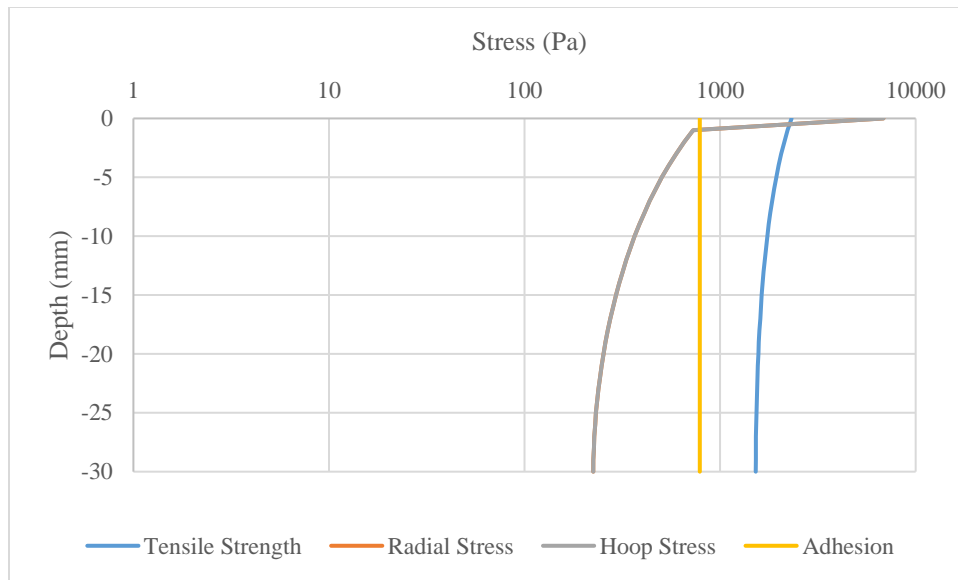
Figure 5.35 Stress distribution at the time of crack initiation at the center of the untreated soil layer

The soil treated with 0.5% fiber content behaves in a similar way to the plain soil, with desiccation cracking behavior occurring 5 minutes earlier, shown in Figure 5.36. This means that

the added tensile strength from the addition of the recycled carpet fibers did not overcome the jump when switching stress formulations. In fact, the increase in the hydric constant, and subsequently, the shrinkage strain caused the stress to exceed the adhesion at an earlier stage.
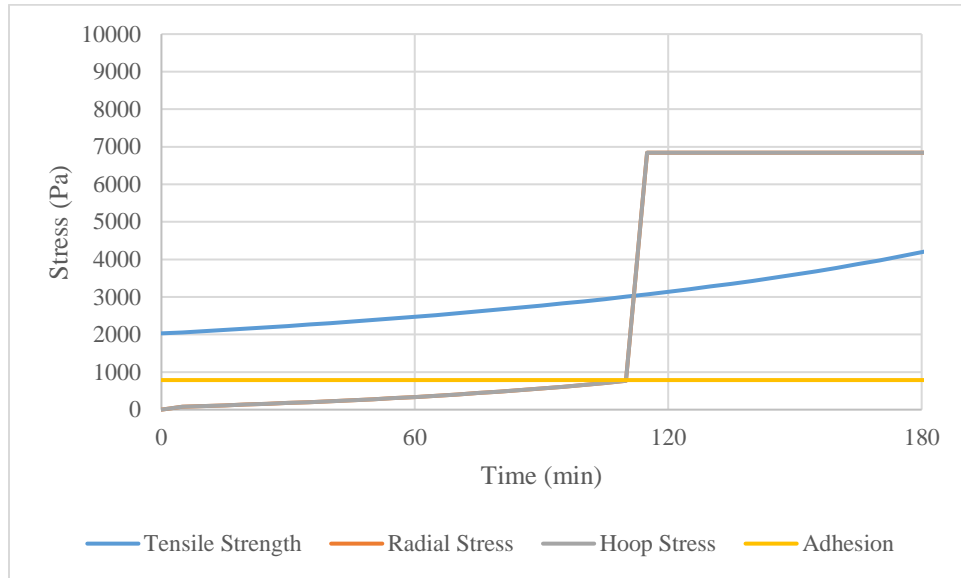
Figure 5.36 Stress progression at center of 0.5% fiber soil surface over time

This behavior produces a stress-depth curve nearly identical to that of the plain soil at the time of crack initiation (Figure 5.37). The main difference displayed is the tensile strength curve is shifted right to account for the fiber introduction.
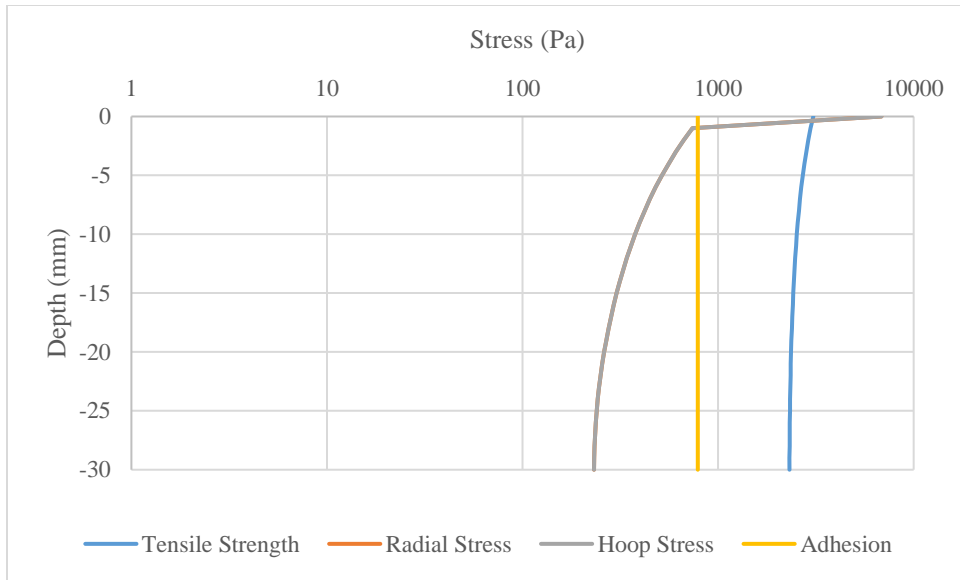
Figure 5.37 Stress distribution at the time of crack initiation at the center of the 0.5% fiber soil

The soil treated with 2% fiber content deviates in its behavior when compared to the previous two examples, as shown in Figure 5.38. The added tensile strength from the addition of the recycled carpet fibers vastly overwhelms the jump when switching stress formulations. As a result, the effect of the increase in the hydric constant is dwarfed by the increase in tensile strength, meaning that the soil will pull away from the mold wall, but cracks will not form.
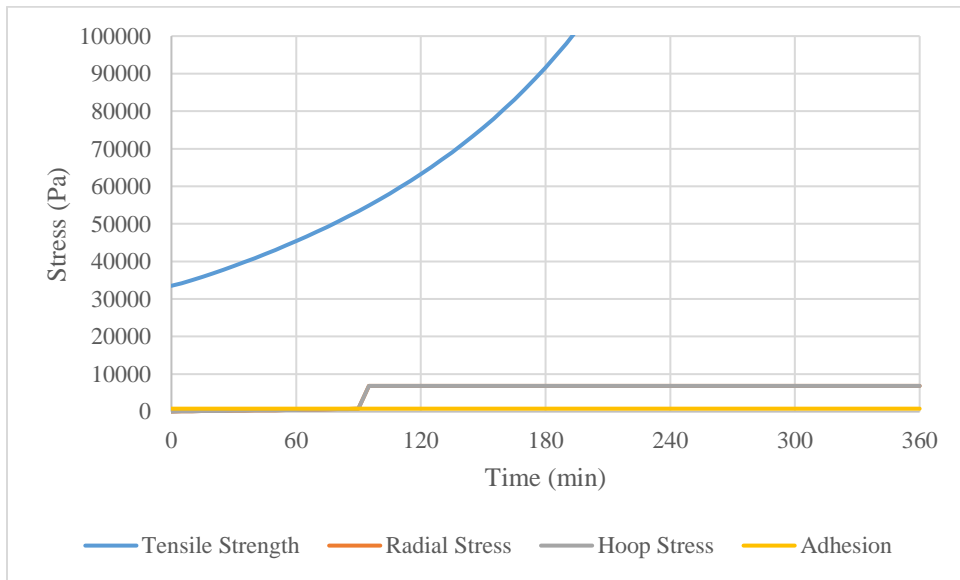
Figure 5.38 Stress progression at center of 2% fiber soil surface over time

This previously described behavior also affects the depth-stress plot shown in Figure 5.39. The tensile strength is shifted far to the right, greatly exceeding the stresses developed in the clay model.
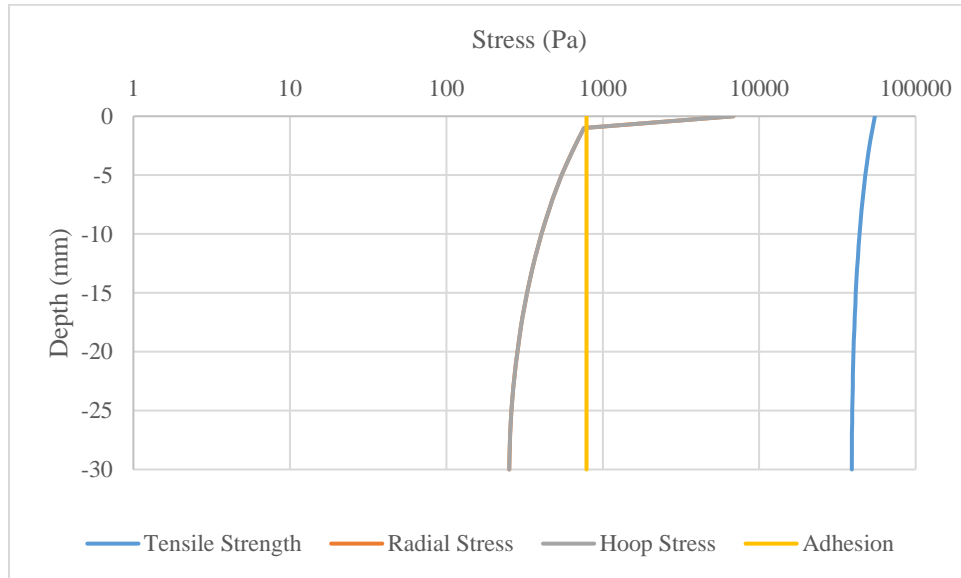
Figure 5.39 Stress distribution at the time of crack initiation at the center of the 2% fiber soil

The behavior of the soil improved by xanthan gum strayed even farther from the behavior from the other samples (Figure 5.40). Whereas all the other improvement methods broke their bond with the vertical wall of the mold, the increased adhesion lead to the xanthan gum-aided model never producing a wall crack. However, unlike the other specimens, the stresses from the pre-wall crack stress formulation exceeded the tensile strength towards the end of the time period, meaning that the desiccation cracking will occur without separation from the mold.
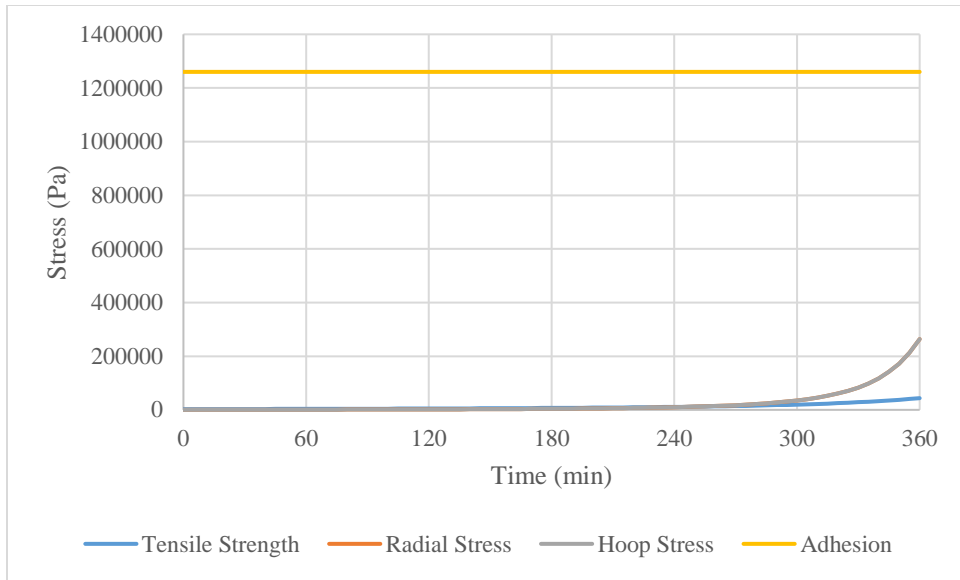
Figure 5.40 Stress progression at center of xanthan gum soil surface over time

The stress-depth plot for this model produced a plot similar to that of the 2% fiber content model (Figure 5.41). The main difference, however, is that the adhesion in this model is shifted far to the right, rather than the tensile strength.
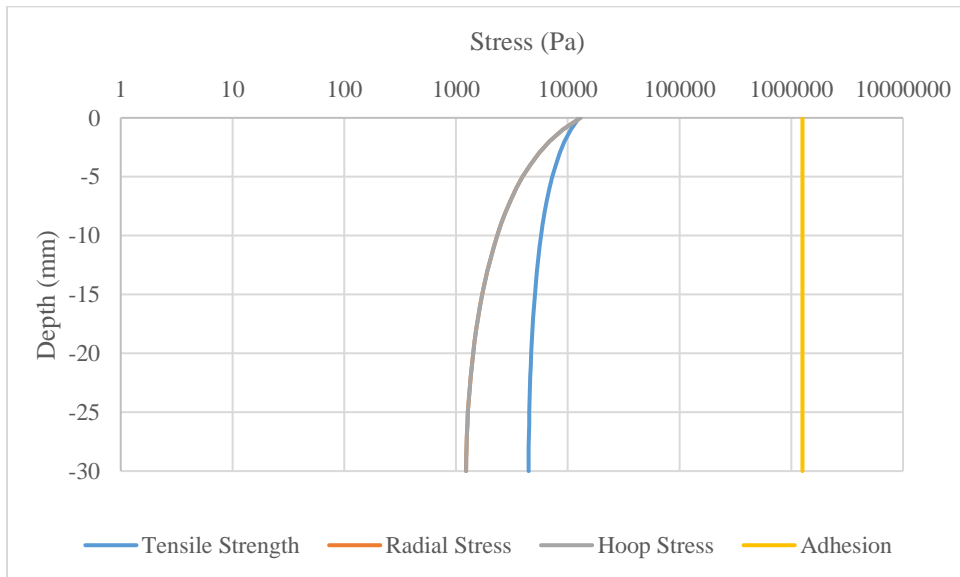
Figure 5.41 Stress distribution at the time of crack initiation at the center of the xanthan gum soil

In addition to the above stress plots, heat maps were generated of the clay profile at important times to observe the stress and displacement propagation throughout the whole clay layer, rather than just one point. Figure 5.42 displays the heat map for the hoop stress across the clay profile at the time of crack initiation for the untreated kaolin clay.
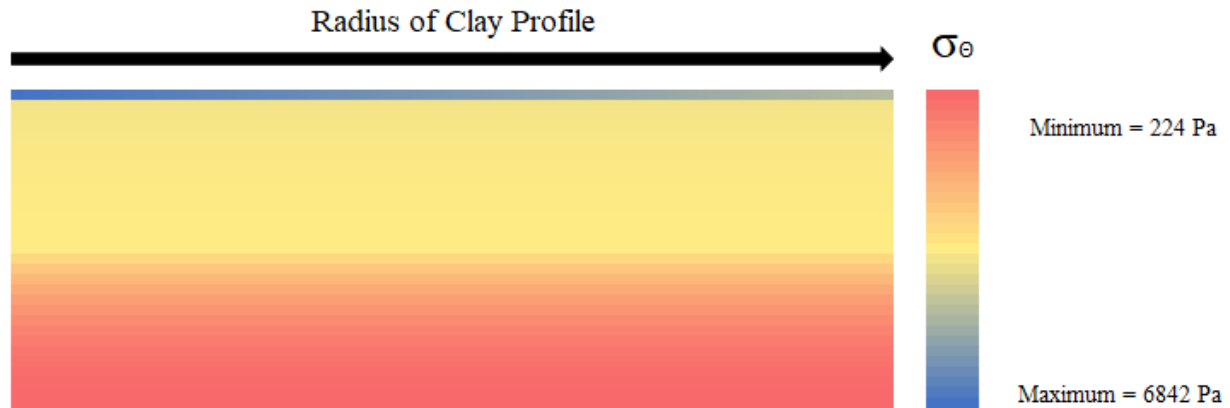
Figure 5.42 Hoop stress across the clay profile at the time of crack initiation for untreated soil

The stresses vary as a function of depth up until the very top section of clay and then begin to decrease as a function of radius. This is because as the stress formulation state switches from pre-wall crack to post-wall crack, the stress also switches from being predominately a function of time to a function of radial distance.

This trend of behavior continues for each of the fiber-aided soil models, albeit with increasing stress magnitudes. The stress profile at crack initiation for the xanthan gum model in Figure 5.43 displays the different pattern of stress propagation along the soil layer in comparison to Figure 5.42.
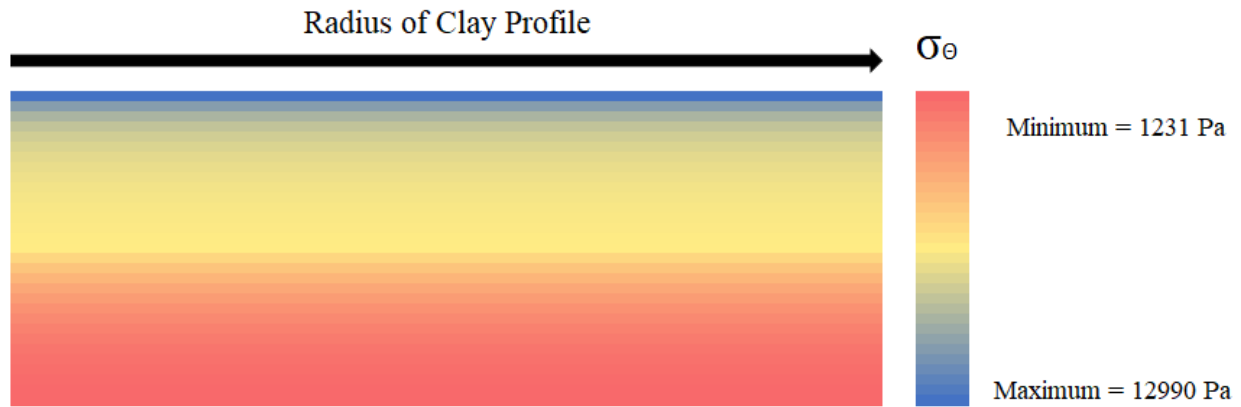
Figure 5.43 Hoop stress across the clay profile at the time of crack initiation for the xanthan gum

soil

On top of the stress propagation heat map, the radial displacement was also examined in this form. In Figure 5.44, the radial displacement for the untreated sample at the last time step shows that the greatest radial movement (5.08 mm) occurs on the outside of the clay specimen, in the top few layers. In fact, the majority of the figure shows no displacement occurring. Also, no displacement occurs at the center of the profile as all shrinkage occurs in the negative radial direction, and the center should remain immobile. Figure 5.44
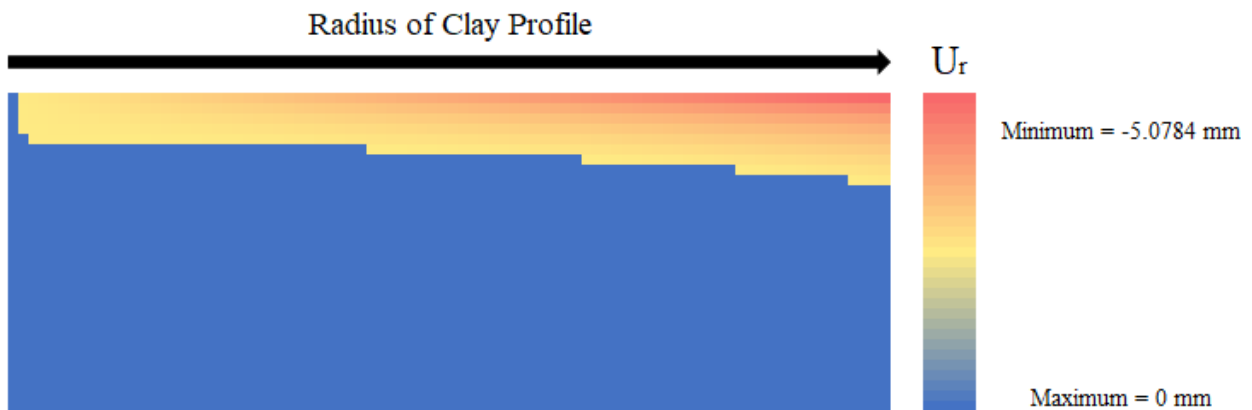
Figure 5.44 Displacement across the clay profile at the end of analysis for untreated soil

Figure 5.45 displays the displacement heat map for the 0.5% fiber content model. This simulation shows a slight increase in overall radial displacement (5.54 mm) and shrinkage, as well as the number of nodes where shrinkage occurs.

Radius of Clay Profile

U_r

Minimum = -5.542 mm

Maximum = 0 mm
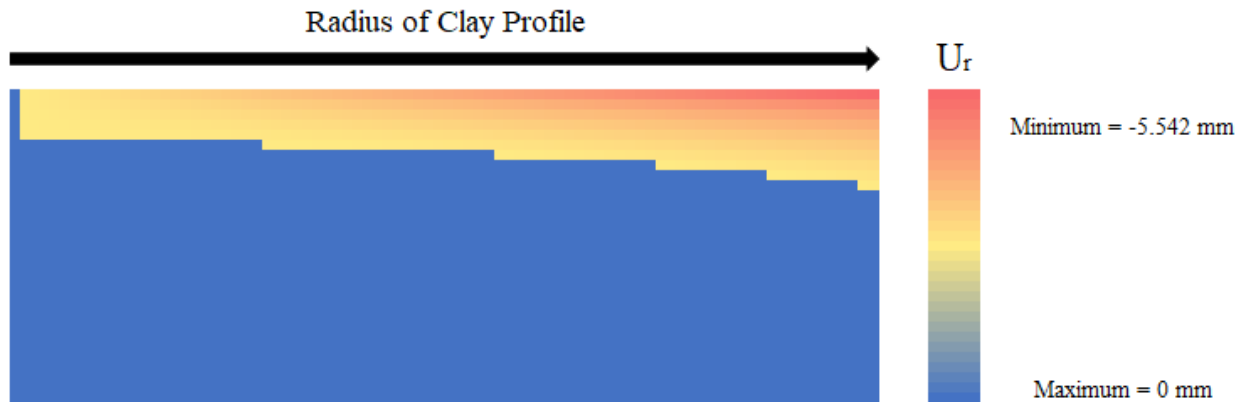
Figure 5.45 Displacement across the clay profile at the end of analysis for 0.5% fiber soil

Figure 5.46 maps the radial displacement within the soil layer for 2.0% fiber content model. It shows the greatest amount of shrinkage occurring in terms of magnitude with a maximum displacement of -7.678 mm in the radial direction. The fiber-reinforced soil model also possesses the highest number of nodes that experience movement.
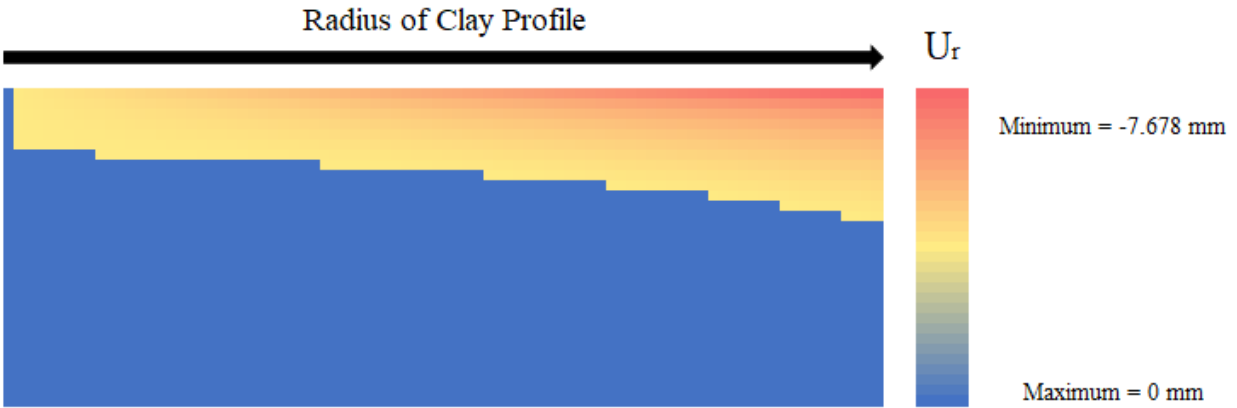
Figure 5.46 Displacement across the clay profile at the end of analysis for 2% fiber soil

Finally, Figure 5.47 displays the displacement within the soil profile for the xanthan gum-amended soil model. Because wall cracking never occurred, radial displacement always remained zero, yielding the displacement heat map below.
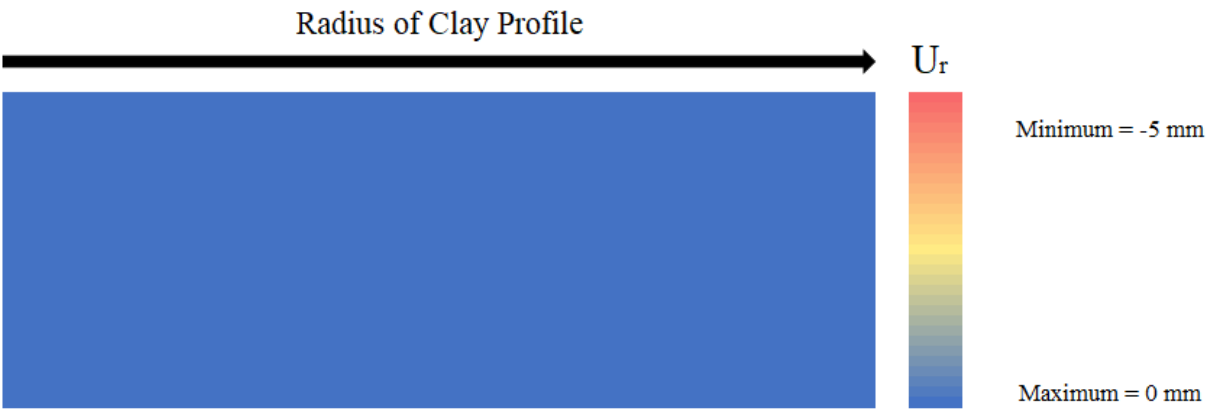
Figure 5.47 Displacement across the clay profile at the end of analysis for xanthan gum soil

5.5.3. COMPARISON TO EXPERIMENTAL CRACK INITIATION

In addition to the results from the previous section, the crack initiation data returned from the model was compared to the kaolin clay experimental results. While the models generally predict the crack and wall crack to occur simultaneously, this was not always the case for the

physical experiments. Also, while the model was able to be discretized into smaller time steps, the experimental results could only return values every 30 minutes. Figure 5.48 displays the internal crack time for each of the experiments (solid bar) as well as the model results (dashed bar). The model does fairly well at predicting the crack time for the untreated soil and the 0.5% specimens.

However, the gap between the model and experimental results is wider for the 2% fiber content and the xanthan gum specimens. For the 2% fiber content specimens, when cracking did occur, the maximum width that occurred was 1.4 mm and a maximum length of 29.4 mm. In addition, the cracks showed minor growth and were isolated, suggesting they were more products of imperfections in the soil surface rather than to soil failure.
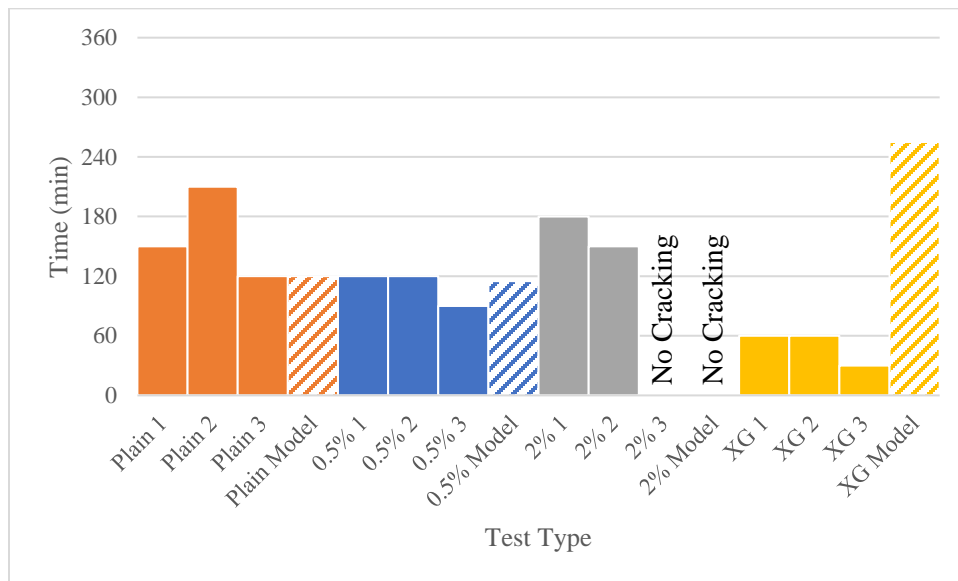
Figure 5.48 Internal crack time for each of the experiments and model results

Figure 5.49 displays the wall crack time for each of the experiments (solid bars) as well as the model results (dashed bars). With the exception of outliers, the model approximates when the clay will separate from the mold wall. While one specimen of untreated soil never detached from the mold, the model predicted the exact time at which the other two specimens would break away.

In addition, the model predicts that the xanthan gum-aided samples would never separate from the wall, which was the case for every tested specimen.
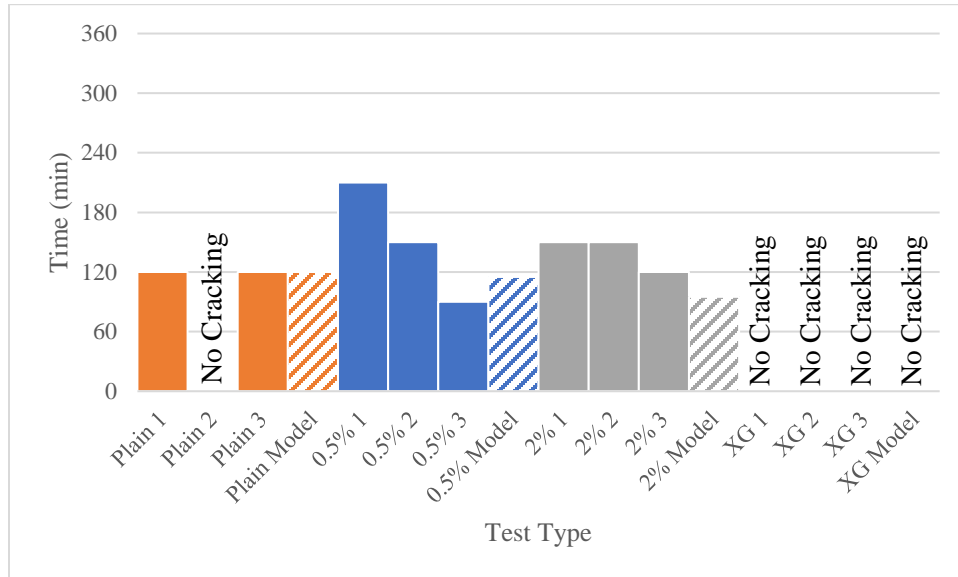
Figure 5.49 Wall crack time for each of the experiments and model results

Figure 5.50 displays water content at crack initiation for each of the experiments as well as the model results. This figure shows that the model is even more accurate in this predictive measurement than predicting the time of crack initiation for the untreated soil and the 0.5% fiber soil, though slightly underestimating the time at which crack formation will occur. This is most likely because the model cannot take soil imperfections into account which can expedite crack commencement in the physical experiments. Again, the model performs worse with the 2% fiber content specimens and the xanthan gum specimen. The reasoning for this deviation remains the same, however.
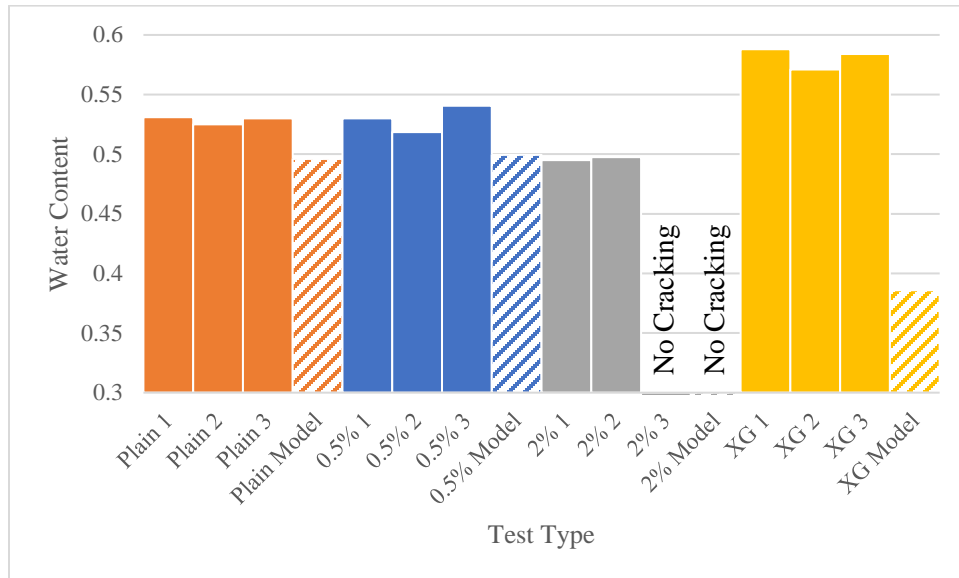
Figure 5.50 Internal crack water content for each of the experiments and model results

Figure 5.51 displays the wall crack water content at wall crack initiation for each of the experiments (solid bars) as well as the model results (dashed bars). Once again, the model predicts at which water content will the clay separate from the vertical mold wall, establishing a strong relationship between the experimental and mathematical data. Except for the untreated specimen that did not separate from the wall (Plain 2), the model provides a reasonable estimate for the water content at which this will occur. Going further, the 2% fiber content-aided soil provided a particularly strong prediction of water contact at crack origination.
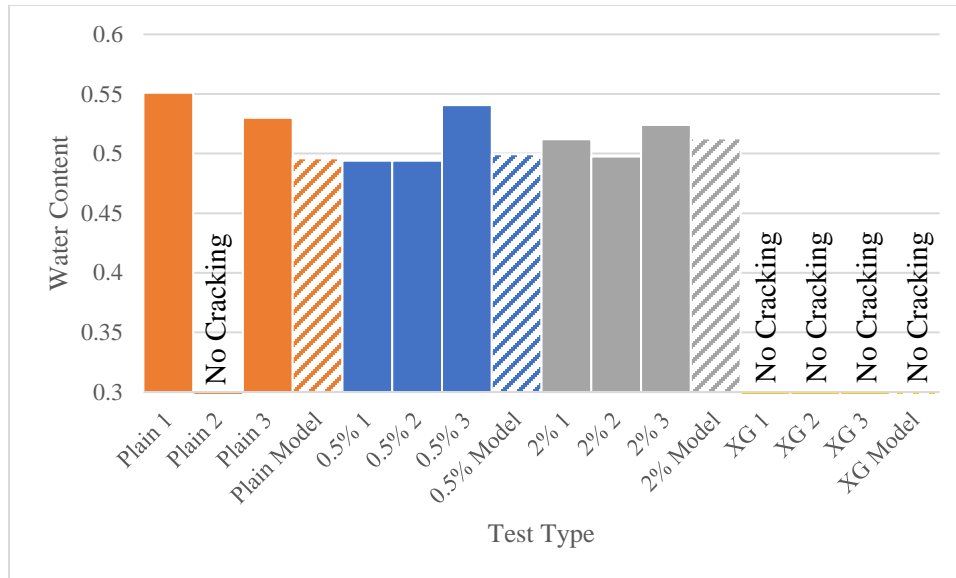
Figure 5.51 Water content at wall crack initiation for each of the experiments and model results

5.5.4. SENSITIVITY ANALYSIS

A sensitivity analysis was performed on several of the material properties in order to determine their effect on the overall model behavior. The sensitivity analysis was completed by running the untreated soil model and increasing the selected parameter by 20% and 50% and then decreasing the same parameters by the same amount. Their effect on the hoop stress was then plotted along with the adhesion and tensile stress as functions of time. The analysis allowed for a comparison of crack initiation time as well as stress magnitude.

The first parameter that was tested as part of the sensitivity analysis was the hydric constant used as part of the model coupling process. Figure 5.52 shows that as the hydric constant increased, the slope of the hoop stress in the pre-wall crack state increased at a greater rate. This increase in the hoop stress led to the time of crack initiation decreasing significantly. On the other hand, by decreasing the hydric constant, the slope of the hoop stress before separating from the wall is

decreased, postponing desiccation crack time at a greater rate than it was accelerated for an increased hydric constant.
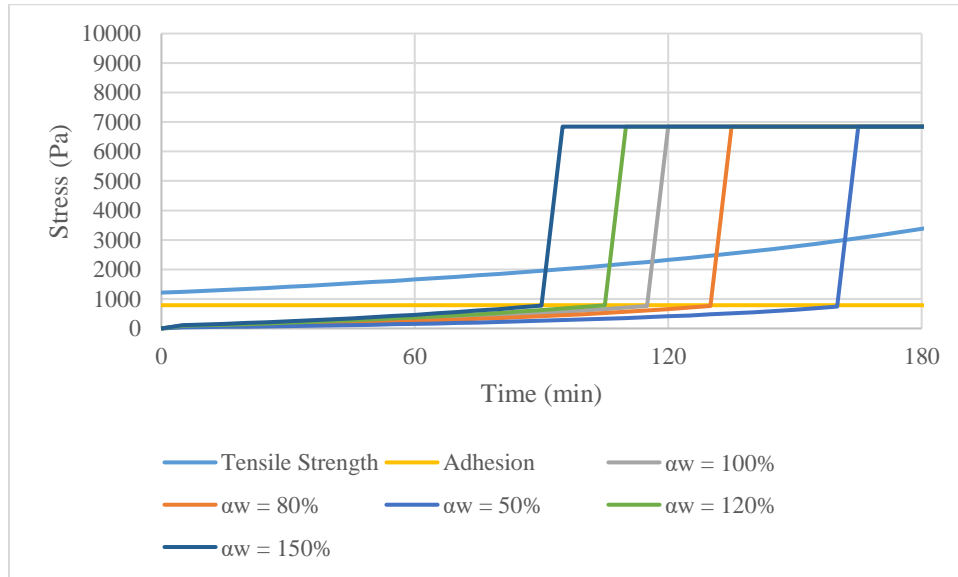
Figure 5.52 Hydric constant sensitivity analysis on crack initiation time

The next parameter that was examined as part of the sensitivity analysis was Young's Modulus. In terms of stress, Young's Modulus only appears in Equation 4-45 and Equation 4-46 or the pre-wall crack stress calculation. And because it shares the same relationship with each stress as the shrinkage strain, Figure 5.53 is identical to Figure 5.52.
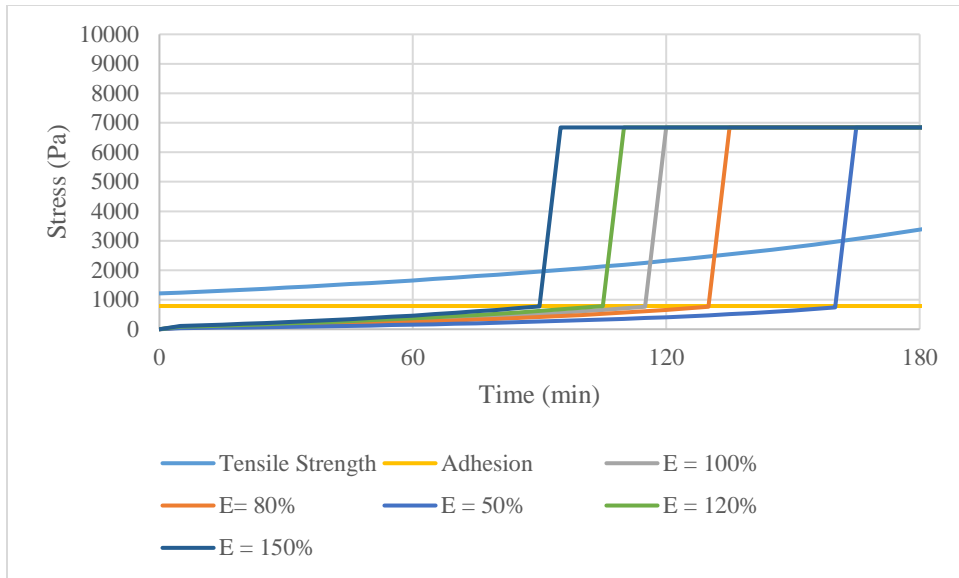
Figure 5.53 Young's Modulus sensitivity analysis on crack initiation time

Despite this, Young's modulus also appears in Equation 4-49 or the radial displacement formula. Figure 5.54 shows how altering Young's modulus affects radial displacement as a function of time. As seen in Figure 5.53, an increase in Young's modulus accelerates wall crack initiation, which leads to radial displacement occurring at an earlier time. However, Figure 5.54 shows that the rate of radial displacement decreases as Young's Modulus is increased. In fact, there appears to be a cross over point near the end of the model's duration, where the decreased Young's modulus will begin to result in a larger displacement.
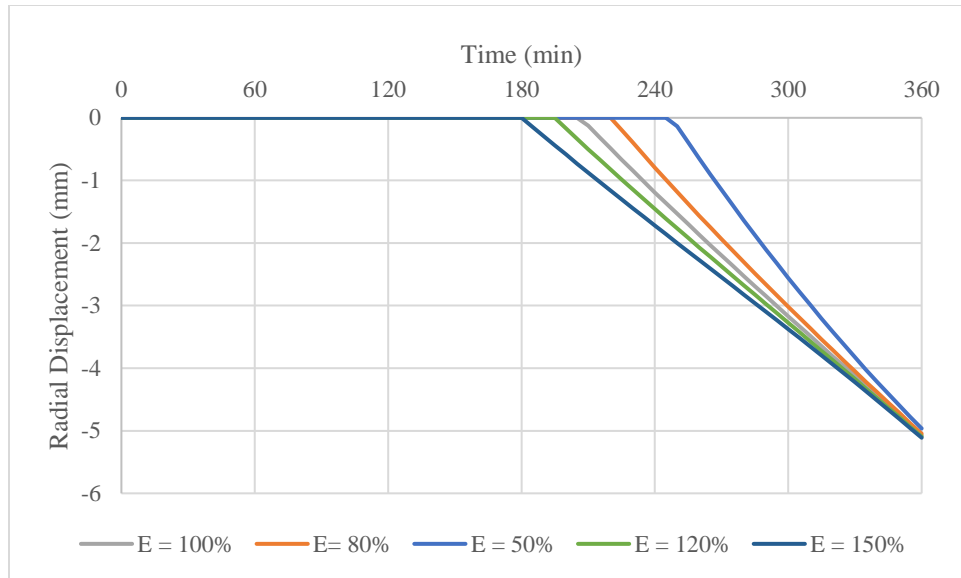
Figure 5.54 Young's Modulus sensitivity analysis on radial displacement

The final parameter that was inspected as part of the sensitivity analysis was the interface shear strength. Because the interface shear strength affected both the post wall crack stress and adhesion, each value was plotted for each of the shear stress alterations in Figure 5.55. By decreasing the adhesion due to the decrease in the interface shear stress, clay separation from the mold occurred at an earlier time. The opposite occurred when increasing adhesion due to an increase in interface shear stress, as the wall crack happened at a later time. After the wall crack, the changes in shear stress acted proportionally with the hoop stress, with the greatest hoop stress occurring with a 50% increase in shear stress and the minimum hoop stress accompanying the minimum interface shear stress.
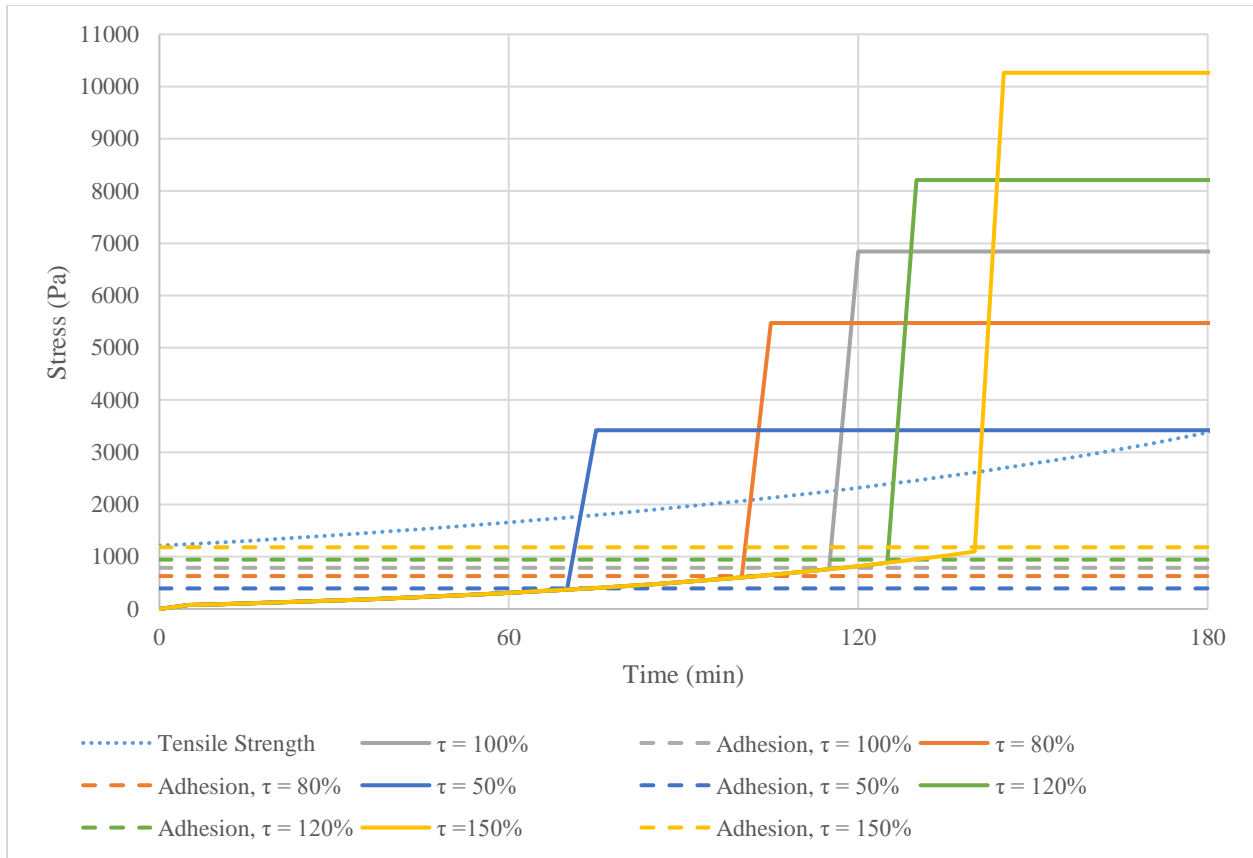
Figure 5.55 Interface shear strength sensitivity analysis on stress development

5.5.6. MODEL LIMITATIONS

The predictive hydromechanical model has several limitations. First, the one-way coupling is used to couple moisture transfer and soil deformation. In one-way coupling, the change in the moisture content is converted into shrinkage strains to be utilized as an input for the in the mechanical problem. This results in displacement and stresses that are different to those obtained by simulating dry conditions. However, the hydrological parameters are assumed to be independent of strain. The corresponding results from the mechanical model are not input into the hydraulic model and therefore model cracking behavior is only until the time of initial crack formation. In two-way coupling, the moisture change is used to determine the shrinkage strain,

and in turn desiccation cracking (and possibly other parameters such as stress and dilation) are then used to calculate updated hydrological conductivity for the next model iteration[71]. One-way coupling is usually sufficient if the hydrological parameters are not expected to have a large impact on soil mechanical behavior.

Second, the mechanical crack behavior is only valid through the moment of initial crack initiation. This is because the energy associated with the desiccation crack formation as well as the increased avenue of evaporation via cracks were not taken into consideration. The analytical solution described in the Section 4.4 treats the desiccation cracking as a purely tensile failure problem, without taking into account the development of partially penetrating cracks, and the subsequent crack propagation. Thus, the analytical model may be used to predict the hoop and radial stresses that develop in the clay layer for a given reduction in the moisture content as long as they do not exceed the tensile strength of the soil.

CHAPTER 6 – CONCLUSION

6.1 INTRODUCTION

A brief overview of the research conducted in this thesis can be found in Section 6.2. The main overall observations and conclusions from this research are presented in Section 6.3. Recommendations made based on the findings in this project for future research are given in Chapter 6.4.

6.2 RESEARCH SUMMARY

This study was undertaken in order to investigate novel eco-friendly soil improvement techniques and their effect on the desiccation cracking behavior of cohesive soils. With current soil improvement techniques for desiccation cracking consisting mostly of cement, eco-friendly options are of great importance and necessity. The investigation was completed by conducting physical experiments and then analyzing the results of those tests using image analysis software. In addition, the data from the physical tests were then compared to the results from a hydromechanical model.

The two types of cohesive soils that were studied throughout this investigation were residual Piedmont soil and pure white kaolin clay. Four eco-friendly soil improvement techniques were tested, including fly ash, recycled carpet fibers, bioplastic, and xanthan gum. Both recycled carpet fibers and fly ash were considered sustainable materials under the idea that repurposed industrial waste is a sustainable material. Three types of desiccation tests were performed. The first test was a room temperature test at 20°C on the Piedmont soil utilizing the fly ash, carpet fibers, and bioplastic. The next test was an accelerated test on the same materials at 105°C that included a rewetting cycle. The final test was performed on the kaolin clay at a temperature of 30°C using the recycled carpet fibers and xanthan gum as improvement methods.

The quantitative analysis of the desiccation test was completed using two different image processing techniques. The first was an original code powered by MATLAB's image analysis software before performing image matrix operations in a VBA program. The MATLAB image processing technique was used on the tests on the Piedmont soil. The second technique was through the commercially available program GOM Correlate and was used on the samples from the kaolin desiccation tests. A comparative analysis of the soil improvement techniques was completed using a combination of crack geometry parameters.

A predictive hydromechanical model was created in order to further analyze the cracking behavior of the soil. Using Richard's equation and van Genuchten model, the water content across the depth of the soil layer for a given number of time steps was modeled. The hydraulic portion of the model was then coupled to a mechanical model where the water contents were converted into shrinkage strains and subsequently into a field of stresses along time, depth, and radial distance. The stresses were then used to predict cracking behavior for each of the specimens tested in the kaolin clay desiccation tests.

6.3 RESEARCH CONCLUSIONS

From the tests that were completed in this study, adding 2% fiber content was the most effective soil improvement technique. Even when cracking did occur, they were the smallest of the cracks that occurred in both length and width. The cracks that formed in the specimens aided with 2% fiber content did not propagate or form large crack networks. Instead, crack growth leveled out and were isolated incidents. This suggests that the cracking in these samples was a result of imperfections in the soil surface rather than stresses exceeding the unaltered tensile strength of the kaolin clay.

The xanthan gum-aided samples were the most difficult to model as the behavior of the xanthan gum in the sample was not entirely a function of water content. Based on the results of the splitting tensile test on the completely dried xanthan gum specimens, the tensile strength should have been increased. However, these specimens cracked at a lower stress level than the untreated soil samples. As a result, the hydromechanical model severely over-estimated the cracking time and water content for these samples. In addition, the cracks did not deepen as the water was removed from the soil. While the cracks in the other untreated specimens would eventually grow to reach the bottom of the mold, the cracks in the samples with xanthan gum would reach a certain depth and then stop. This behavior suggests there is a time element to maximizing the strengthening behavior of the xanthan gum.

Following this line of thinking, xanthan gum has been shown to strengthen kaolin clay when completely dry and unrestrained, most notably in the unconfined compression test and splitting tensile test. This suggests that the soil preparation for the xanthan gum-aided specimens in the desiccation tests was not optimized. The benefits of xanthan gum were not harnessed in the controlled preparation environment that was necessary for a comparative analysis for soil improvement techniques.

In terms of analyzing cracking behavior, the model was effective in explaining crack pattern behavior for different soil improvement techniques. The radial direction of the cracks in the samples where wall cracking occurred can be explained by the hoop stress always exceeding the radial stress in that situation. As a result, cracking occurred in the direction perpendicular to maximum stress, leading to the common crack pattern of cracks initiating centrally before radiating to the edge of the specimen. On the other hand, the samples treated with xanthan gum displayed a far more varied crack pattern, correlating to the stress conditions in the pre-wall crack stage, with hoop stress and radial stress being equal in all lateral positions.

The model tended to underestimate the water content at crack initiation compared to the water content at crack initiation measured experimentally. For the untreated and 0.5% fiber content specimens, the underestimation was approximately 3-4%. This can be explained by the modeling

predicting cracking to occur based solely on tensile strength versus stress, whereas natural cracking behavior is a function of soil surface conditions as well as stress conditions. The imperfect soil surface conditions could not be modeled. It is likely that the existence of soil surface imperfections leads to crack initiation occurring at greater water contents in the tested specimens.

6.4 RECOMMENDATIONS FOR FUTURE RESEARCH

Based on the results and observations in this research, it is clear that recycled carpet fibers are the most effective sustainable soil improvement technique for slowing desiccation cracking. However, the findings in this research suggest several topics that are worthy of future research. These topics include:

- Evaluation of the scalability of recycled carpet fibers and the relationship between fiber length, specimen size,

- Evaluation of xanthan gum as an improvement technique individually where soil preparation can be optimized,

- Examination of the long-term viability of the improvement techniques,

- Examination the impact of temperature fluctuations on improvement techniques, and overall desiccation,

- Improvement of the hydromechanical model so that crack behavior after the initial crack can be evaluated, and

- Creation of an extended finite element or discrete element model for desiccation cracking in improved soils.

REFERENCES

1. Peron H, Hueckel T, Laloui L, Hu LB. Fundamentals of desiccation cracking of fine-grained soils: experimental characterisation and mechanisms identification. *Can Geotech J*. 2009;46(10):1177-1201. doi:10.1139/T09-054

2. Shah VS. DETECTION OF MICROCRACKS IN CONCRETE CURED AT ELEVATED TEMPERATURE. :73.

3. Jayanthi PNV, Singh DN. Utilization of Sustainable Materials for Soil Stabilization: State-of-the-Art. *Adv Civ Eng Mater*. 2016;5(1):20150013. doi:10.1520/ACEM20150013

4. Campbell B, Khachatryan H, Behe B, Dennis J, Hall C. Consumer Perceptions of Eco-friendly and Sustainable Terms. *Agric Resour Econ Rev*. 2015;44(1):21-34. doi:10.1017/S1068280500004603

5. Hirobe S, Oguni K. Modeling and numerical investigations for hierarchical pattern formation in desiccation cracking. *Phys Nonlinear Phenom*. 2017;359:29-38. doi:10.1016/j.physd.2017.08.002

6. Rodríguez R, Sánchez M, Ledesma A, Lloret A. Experimental and numerical analysis of desiccation of a mining waste. *Can Geotech J*. 2007;44(6):644-658. doi:10.1139/t07-016

7. Cordero JA, Useche G, Prat PC, Ledesma A, Santamarina JC. Soil desiccation cracks as a suction–contraction process. *Géotechnique Lett*. 2017;7(4):279-285. doi:10.1680/jgele.17.00070

8. Costa S, Kodikara J, Shannon B. Salient factors controlling desiccation cracking of clay in laboratory experiments. *Géotechnique*. 2013;63(1):18-29. doi:10.1680/geot.9.P.105

9. Kodikara J. K., Choi X. A Simplified Analytical Model for Desiccation Cracking of Clay Layers in Laboratory Tests. *Unsaturated Soils 2006*.:2558-2569. doi:10.1061/40802(189)218

10. Shin H, Santamarina JC. Desiccation cracks in saturated fine-grained soils: particle-level phenomena and effective-stress analysis. *Géotechnique*. 2011;61(11):961-972. doi:10.1680/geot.8.P.012

11. Peron H, Laloui L, Hueckel T, Hu LB. Desiccation cracking of soils. *Rev Eur Génie Civ*. 2009;13(7-8):869-888. doi:10.3166/ejece.13.869-888

12. Chaduvula U, Viswanadham BVS, Kodikara J. A study on desiccation cracking behavior of polyester fiber-reinforced expansive clay. *Appl Clay Sci*. 2017;142:163-172. doi:10.1016/j.clay.2017.02.008

13. Sanchez M, Atique A, Kim S, Romero E, Zielinski M. Exploring desiccation cracks in soils using a 2D profile laser device. *Acta Geotech*. 2013;8(6):583-596. doi:10.1007/s11440-013-0272-1

14. Suits LD, Sheahan TC, Lakshmikantha MR, Prat PC, Ledesma A. Image Analysis for the Quantification of a Developing Crack Network on a Drying Soil. *Geotech Test J*. 2009;32(6):102216. doi:10.1520/GTJ102216

15. Peron H, Laloui L, Hueckel T, Hu LB. Desiccation cracking of soils. *Eur J Environ Civ Eng*. 2009;13(7-8):869-888. doi:10.1080/19648189.2009.9693159

16. Arena A, Delle Piane C, Sarout J. A new computational approach to cracks quantification from 2D image analysis: Application to micro-cracks description in rocks. *Comput Geosci*. 2014;66:106-120. doi:10.1016/j.cageo.2014.01.007

17. Shokri N, Zhou P, Keshmiri A. Patterns of Desiccation Cracks in Saline Bentonite Layers. *Transp Porous Media*. 2015;110(2):333-344. doi:10.1007/s11242-015-0521-x

18. Zielinski M, Sánchez M, Romero E, Atique A. Precise observation of soil surface curling. *Geoderma*. 2014;226-227:85-93. doi:10.1016/j.geoderma.2014.02.005

19. Shah MV, Pandya HJ, Shukla AD. Influence of Chemical Additives on Shrinkage and Swelling Characteristics of Bentonite Clay. *Procedia Eng*. 2017;189:932-937. doi:10.1016/j.proeng.2017.05.144

20. Consoli NC, Bittar Marin EJ, Quiñónez Samaniego RA, Heineck KS, Johann ADR. Use of Sustainable Binders in Soil Stabilization. *J Mater Civ Eng*. 2019;31(2):06018023. doi:10.1061/(ASCE)MT.1943-5533.0002571

21. Wei, Li, Han, et al. Experimental Research on Deformation Characteristics of Using Silty Clay Modified Oil Shale Ash and Fly Ash as the Subgrade Material after Freeze-Thaw Cycles. *Sustainability*. 2019;11(18):5141. doi:10.3390/su11185141

22. Kamon M, Nontananandh S. Combining Industrial Wastes with Lime for Soil Stabilization. *J Geotech Eng*. 1991;117(1):1-17. doi:10.1061/(ASCE)0733-9410(1991)117:1(1)

23. Wild S, Kinuthia JM, Robinson RB, Humphreys I. Effects of ground granulated blast furnace slag (GGBS) on the strength and swelling properties of lime-stabilized kaolinite in the presence of sulphates. *Clay Miner*. 1996;31(3):423-433. doi:10.1180/claymin.1996.031.3.12

24. Kalkan E. Influence of silica fume on the desiccation cracks of compacted clayey soils. *Appl Clay Sci*. 2009;43(3-4):296-302. doi:10.1016/j.clay.2008.09.002

25. Zumrawi MME, Mahjoub AMM, Alnour IM. Effect of Some Chloride Salts on Swelling Properties of Expansive Soil. 2016;6(2):8.

26. Mirzababaei M, Miraftab M, Mohamed M, McMahon P. Impact of Carpet Waste Fibre Addition on Swelling Properties of Compacted Clays. *Geotech Geol Eng*. 2013;31(1):173-182. doi:10.1007/s10706-012-9578-2

27. Ghiassian H, Poorebrahim G, Gray DH. Soil Reinforcement with Recycled Carpet Wastes. *Waste Manag Res*. 2004;22(2):108-114. doi:10.1177/0734242X04043938

28. Shahnazari H, Ghiassian H, Noorzad A, Shafiee A, Tabarsa AR, Jamshidi R. Shear Modulus of Silty Sand Reinforced by Carpet Waste Strips. 2009;11(3):10.

29. Chaduvula U, Manogaran I, Viswanadham BVS, Kodikara J. Some Studies on Desiccation Cracking of Fiber-Reinforced Expansive Clay Subjected to Drying and Wetting Cycles. In: *PanAm Unsaturated Soils 2017*. Dallas, Texas: American Society of Civil Engineers; 2018:361-370. doi:10.1061/9780784481707.036

30. Pastor J, Tomás R, Cano M, Riquelme A, Gutiérrez E. Evaluation of the Improvement Effect of Limestone Powder Waste in the Stabilization of Swelling Clayey Soil. *Sustainability*. 2019;11(3):679. doi:10.3390/su11030679

31. Hidalgo C, Carvajal G, Muñoz F. Laboratory Evaluation of Finely Milled Brick Debris as a Soil Stabilizer. *Sustainability*. 2019;11(4):967. doi:10.3390/su11040967

32. Chang I, Im J, Prasidhi AK, Cho G-C. Effects of Xanthan gum biopolymer on soil strengthening. *Constr Build Mater*. 2015;74:65-72. doi:10.1016/j.conbuildmat.2014.10.026

33. Soldo A, Miletic M. Study on Shear Strength of Xanthan Gum-Amended Soil. *Sustainability*. 2019;11:6142. doi:10.3390/su11216142

34. Soldo A, Miletić M, Auad ML. Biopolymers as a sustainable solution for the enhancement of soil mechanical properties. *Sci Rep*. 2020;10(1):1-13. doi:10.1038/s41598-019-57135-x

35. Chen Rui, Zhang Lianyang, Budhu Muniram. Biopolymer Stabilization of Mine Tailings. *J Geotech Geoenvironmental Eng*. 2013;139(10):1802-1807. doi:10.1061/(ASCE)GT.1943-5606.0000902

36. Das SK, Mahamaya M, Panda I, Swain K. Stabilization of Pond Ash using Biopolymer. *Procedia Earth Planet Sci*. 2015;11:254-259. doi:10.1016/j.proeps.2015.06.033

37. Al-alaily HS, Hassan AAA, Hussein AA. Use of extended finite element method and statistical analysis for modelling the corrosion-induced cracking in reinforced concrete containing metakaolin. *Can J Civ Eng*. 2018;45(3):167-178. doi:10.1139/cjce-2017-0298

38. Ling J, Tao Z, Qian J, Fu W. Investigation the influences of geotextile on reducing the thermal reflective cracking using XFEM. *Int J Pavement Eng*. 2018;19(5):391-398. doi:10.1080/10298436.2017.1402598

39. Liu P. Extended finite element method for strong discontinuity analysis of strain localization of non-associative plasticity materials. *Int J Solids Struct*. 2015;72:174-189. doi:10.1016/j.ijsolstr.2015.07.021

40. Sánchez M, Manzoli OL, Guimarães LJN. Modeling 3-D desiccation soil crack networks using a mesh fragmentation technique. *Comput Geotech*. 2014;62:27-39. doi:10.1016/j.compgeo.2014.06.009

41. Remmers J, Deborst R, Needleman A. The simulation of dynamic crack propagation using the cohesive segments method. *J Mech Phys Solids*. 2008;56(1):70-92. doi:10.1016/j.jmps.2007.08.003

42. Amarasiri AL, Kodikara JK, Costa S. Numerical modelling of desiccation cracking. *Int J Numer Anal Methods Geomech*. 2011;35(1):82-96. doi:10.1002/nag.894

43. Sima J, Jiang M, Zhou C. Numerical simulation of desiccation cracking in a thin clay layer using 3D discrete element modeling. *Comput Geotech*. 2014;56:168-180. doi:10.1016/j.compgeo.2013.12.003

44. Amarasiri AL, Kodikara JK. Numerical Modeling of Desiccation Cracking Using the Cohesive Crack Method. *Int J Geomech*. 2013;13(3):213-221. doi:10.1061/(ASCE)GM.1943-5622.0000192

45. Guo Y, Han C, Yu X (Bill). Laboratory characterization and discrete element modeling of shrinkage and cracking in clay layer. *Can Geotech J*. 2018;55(5):680-688. doi:10.1139/cgj-2016-0674

46. El Youssoufi MS, Delenne J-Y, Radjai F. Self-stresses and crack formation by particle swelling in cohesive granular media. *Phys Rev E*. 2005;71(5):051307. doi:10.1103/PhysRevE.71.051307

47. Gui Y, Zhao G-F. Modelling of laboratory soil desiccation cracking using DLSM with a two-phase bond model. *Comput Geotech*. 2015;69:578-587. doi:10.1016/j.compgeo.2015.07.001

48. Gui YL, Zhao ZY, Kodikara J, Bui HH, Yang SQ. Numerical modelling of laboratory soil desiccation cracking using UDEC with a mix-mode cohesive fracture model. *Eng Geol*. 2016;202:14-23. doi:10.1016/j.enggeo.2015.12.028

49. Tang C-S, Cui Y-J, Shi B, Tang A-M, Liu C. Desiccation and cracking behaviour of clay layer from slurry state under wetting–drying cycles. *Geoderma*. 2011;166(1):111-118. doi:10.1016/j.geoderma.2011.07.018

50. Abu-Hejleh A. Naser, Znidarčić Dobroslav. Desiccation Theory for Soft Cohesive Soils. *J Geotech Eng*. 1995;121(6):493-502. doi:10.1061/(ASCE)0733-9410(1995)121:6(493)

51. Konrad JM, Ayad R. A idealized framework for the analysis of cohesive soils undergoing desiccation. In: ; 1997. doi:10.1139/t97-015

52. KAOLIN | CAMEO Chemicals | NOAA. https://cameochemicals.noaa.gov/chemical/25036. Accessed April 9, 2020.

53. Benoît J, Lutenegger AJ, eds. *National Geotechnical Experimentation Sites*. Reston, VA: American Society of Civil Engineers; 2000. doi:10.1061/9780784404843

54. D18 Committee. *Test Methods for Liquid Limit, Plastic Limit, and Plasticity Index of Soils*. ASTM International doi:10.1520/D4318-17E01

55. GOM Correlate | GOM. https://www.gom.com/3d-software/gom-correlate.html. Accessed March 12, 2020.

56. JZUS - Journal of Zhejiang University SCIENCE. http://www.jzus.zju.edu.cn/article.php?doi=10.1631/jzus.A1200274. Accessed March 21, 2020.

57. Image Processing Toolbox. https://www.mathworks.com/products/image.html. Accessed April 6, 2020.

58. Richards LA. CAPILLARY CONDUCTION OF LIQUIDS THROUGH POROUS MEDIUMS. *Physics*. 1931;1(5):318-333. doi:10.1063/1.1745010

59. Van Genuchten M. A Closed-form Equation for Predicting the Hydraulic Conductivity of Unsaturated Soils1. *Soil Sci Soc Am J*. 1980;44. doi:10.2136/sssaj1980.03615995004400050002x

60. Hills RG, Porro I, Hudson DB, Wierenga PJ. Modeling one-dimensional infiltration into very dry soils: 1. Model development and evaluation. *Water Resour Res*. 1989;25(6):1259-1269. doi:10.1029/WR025i006p01259

61. TIMOSHENKO. *Theory of Elasticity*. Mcgraw Hill Education; 2010.

62. Wu J, Yuan J, Ng CWW. Theoretical and experimental study of initial cracking mechanism of an expansive soil due to moisture-change. *J Cent South Univ*. 2012;19(5):1437-1446. doi:10.1007/s11771-012-1160-9

63. Tripathy S, Tadza MYM, Thomas HR. Soil-water characteristic curves of clays. *Can Geotech J*. 2014;51(8):869-883. doi:10.1139/cgj-2013-0089

64. Baille W, Tripathy S, Schanz T. Effective Stress in Clays of Various Mineralogy. *Vadose Zone J*. 2014;13(5). doi:10.2136/vzj2013.06.0112

65. Stirling R. Multiphase Modelling of desiccation cracking in compacted soils. May 2014.

66. Fatahi B, Khabbaz H, Fatahi B. Mechanical characteristics of soft clay treated with fibre and cement. *Geosynth Int*. 2012;19(3):252-262. doi:10.1680/gein.12.00012

67. Jiang P, Mao T, Li N, Jia L, Zhang F, Wang W. Characterization of Short-Term Strength Properties of Fiber/Cement-Modified Slurry. Advances in Civil Engineering. doi:https://doi.org/10.1155/2019/3789403

68. Tang C-S, Wang D-Y, Cui Y-J, Shi B, Li J. Tensile Strength of Fiber-Reinforced Soil. *J Mater Civ Eng*. 2016;28(7):04016031. doi:10.1061/(ASCE)MT.1943-5533.0001546

69. Chen C, Wu L, Perdjon M, Huang X, Peng Y. The drying effect on xanthan gum biopolymer treated sandy soil shear strength. *Constr Build Mater*. 2019;197:271-279. doi:10.1016/j.conbuildmat.2018.11.120

70. Adhesion Coefficient | NAVFAC DM 7.2 | GEO5 | Online Help. https://www.finesoftware.eu/help/geo5/en/adhesion-coefficient-01/. Accessed March 5, 2020.

71. Salimzadeh S, Paluszny A, Nick HM, Zimmerman RW. A three-dimensional coupled thermo-hydro-mechanical model for deformable fractured geothermal systems. *Geothermics*. 2018;71:212-224. doi:10.1016/j.geothermics.2017.09.012

APPENDIX A - PUBLISHED WORKS

Article

Sustainable Improvement of the Crack Resistance of Cohesive Soils

Michael Z. Izzo [1] **and Marta Miletić** [2,*]

[1]   Department of Civil Engineering, Auburn University, Auburn, AL 36849, USA; mzi0006@auburn.edu
[2]   Department of Civil, Construction, and Environmental Engineering, San Diego State University,
      5500 Campanile Dr, San Diego, CA 92182, USA
*   Correspondence: mmiletic@sdsu.edu

check for updates

Abstract: Desiccation cracking of cohesive soils is the development of cracks on the soil surface as a result of a reduction in the soil moisture content. The decrease in soil surface area owing to the desiccation of cohesive soils has an undesirable impact on the mechanical, hydrological, thermal, and physico-chemical properties. Many efforts have been made to improve the desiccation crack resistance of cohesive soils, but the current solutions raise a number of environmental issues, increasing the demand for sustainable soil improvement alternatives. Therefore, the main objective of this study is to investigate novel eco-friendly soil improvement techniques, such as recycled carpet fibers and a gelatin-based bioplastic, and their effect on desiccation cracking in cohesive soils. The improvement of soil crack resistance was studied by conducting desiccation cracking tests on plain and improved soils. In addition, image processing was conducted to quantitatively describe the effect of soil improvement type on the geometrical characteristics of crack patterns. Each soil improvement technique enhanced the soil strength and reduced cracking at room temperature, at an elevated temperature, and when subjecting to cyclic wetting and drying. The addition of bioplastics proved to be the most effective solution, thus demonstrating a viable option to advance future sustainable engineering practices.

Keywords: sustainable materials; ground improvement; image analysis; desiccation cracking

1. Introduction

Desiccation cracking is the development of cracks at the soil surface and throughout the depth of a cohesive soil layer as a result of soil shrinkage due to the reduction of the water content through solar radiation or vegetation absorption. The desiccation of cohesive soils leads to an undesirable impact on the mechanical, hydrological, thermal, and physico-chemical soil properties. For instance, desiccation cracking can lead to decreased soil strength which in turn can cause uneven settlement and catastrophic failures in structures of all types. In addition, this type of soil cracking results in a dramatic increase in the permeability of clayey soils. The increase in soil permeability is particularly problematic when the clay is used as a liner for both landfills and hazardous waste storage [1]. Therefore, the prevention of desiccation cracking is of significant importance to safety, structural, and environmental issues.

Due to the lack of an accepted American Society for Testing and Materials (ASTM) standard, desiccation tests have been conducted in a variety of ways with different boundary conditions, specimen geometry, and properties measured [1–5]. By utilizing a bar of clay seated on a grooved plate, the cracks only propagate in that same direction, creating a series of parallel cracks that can be easily analyzed for aperture and spacing [3]. More realistic two-dimensional (2D) cracking patterns can be obtained as a result of a complete horizontal constraint, allowing for crack intersections to be studied [1]. Therefore, it can be deduced that the geometry of the crack pattern depends strongly on the nature of the boundary

conditions and the sample geometry [3]. A parameter called the crack distribution frequency has been developed to evaluate the change in the area of a sample relative to a sample's original surface area [5]. A similar measurement, the crack intensity factor, has also been developed to analyze the ratio of the area of the cracks to the total specimen area [2]. In addition to the surface crack analysis, the crack depth can be analyzed using either manual means or more advanced image analysis techniques.

Image analysis has proven to be an incredible tool to quantitatively analyze crack characteristics in natural and humanmade geomaterials. To this end, several experimental test methods have been suggested and developed to assess the desiccation crack initiation and propagation within the different geomaterials. These include an analysis of images acquired with a scanning electron microscope (SEM) [6,7], a 2D profile laser [4,8] and different digital image acquisition systems [1,2,5]. A SEM has been extensively used to analyze micro-cracking in concrete and rocks [6] and to evaluate the effect of sodium chloride on the cracking of bentonite clay samples [7]. Despite the power of this technique, the main SEM drawback is its destructive nature. In particular, the specimen needs to be cut into thin slices and the sample faces need to be polished to make cracks and material constituents visible before taking high-resolution 2D images. Furthermore, due to the destructive and complex specimen preparation, the gradual propagation of a single crack cannot be studied. The 2D laser profile imaging has been successfully utilized in studying the propagation and geometry of desiccation cracking in clay soils [4] and the soil curling as a result of soil dehydration [8]. While 2D profile lasers are powerful tools to study desiccation cracking, their initial high price creates a barrier to entry for the academic and industry communities. All of these shortcomings are resolved by utilizing a user-friendly inexpensive digital image acquisition system to analyze the cracking behavior of clay soils.

To resolve safety, structural, and environmental issues caused by desiccation cracking, chemical additives, such as cement and lime, are used as binding agents to increase a clay's strength and resistance to cracking [9]. However, the current solutions have negative implications on the environment such as CO_2 emissions, the prevention of the vegetation growth, and the contamination of groundwater among others [7]. To rectify this, several research studies have been conducted in order to determine the viability of different sustainable soil-strengthening additives. The soil additives are considered sustainable if they have originated and have been refined from the industrial waste which remains toxic and hazardous to the environment when left unattended [10]. While this repurposing does not eliminate all negative side effects of the material as a waste product, it does prevent the negative effects of the use of alternative solutions [10]. The most commonly used sustainable soil additives are fly ash from thermal power plants [10–12], furnace slag from the steel industry [13,14], silica fume from the silicon and ferrosilicon industry [2,7,15,16], and carpet waste [17–19].

Chloride salts, such as ammonium chloride (NH_4Cl) and ferric chloride ($FeCl_3$), have demonstrated the ability to stabilize the volume of clays with high swelling potential [15]. The cations in the compounds reduce the swelling of montmorillonite minerals by replacing the interlayer metallic cations [16]. Furthermore, bentonite samples treated with sodium chloride (NaCl) developed cracks with greater lengths, but the overall crack density was significantly lower [7]. This was due to the effect of salt on the bentonite colloidal interactions that alter the double layer and particle association in a clay slurry [7]. Kalkan [15] used silica fume waste material as a sustainable alternative, and it was shown to significantly reduce desiccation cracking in clay liner systems.

The different types of fibers have also been examined as potential solutions to desiccation cracking [2,7,20]. Recycled carpet fibers have been lightly investigated as a potential soil improvement technique, with most studies being focused on the improvement of the strength properties of granular soil [18,19]. More recently, they have been examined as a potential method to reduce the swelling properties of cohesive soils [17]. The recycled carpet fibers were shown to decrease swelling pressure, with a 1% fiber content providing the most significant pressure drop [17]. Other unsustainable, fiber reinforcements have been shown to cause a significant reduction of desiccation cracking in expanding clay, with crack width decreasing by 50% [20]. Polypropylene fiber reinforcement has been proven to prevent tension crack growth in soils and stabilize soils against shrinking by increasing the soil's tensile

strength [7]. In addition, polypropylene fibers have been utilized to reinforce clay liners, leading the liners to be more rigid in compression and more ductile in tension [11]. The soils treated with fibers have also been shown to perform better than unreinforced soils when exposed to wetting and drying cycles [20].

Other forms of industrial waste have been examined as potential soil improvement techniques [11,12,21,22]. Fly ash has shown the ability to reduce plastic strain in clay soils when exposed to freeze-thaw cycles [12]. In addition, fly ash has been shown to increase compressive strength and produce similar behavioral trends to Portland cement [11]. The use of limestone waste has been shown to reduce the swelling properties of soil, producing a more compact microstructure when examined using SEM imaging [21]. Milled brick debris has also been shown to improve the compressive strength of soils when tested using the unconfined compression test [22].

This study seeks to investigate novel eco-friendly soil improvement techniques and their effect on the desiccation cracking behavior of soils. Three sustainable soil improvement techniques were tested, including fly ash, recycled carpet fibers, and bioplastic. Both recycled carpet fibers and fly ash were considered sustainable materials under the idea that repurposed industrial waste is a sustainable material. Numerous studies have been conducted investigating the effects eco-friendly additives have on soil strength and swelling properties, yet their effect on the crack resistance of cohesive soils has been largely under-investigated. To date, neither recycled carpet fibers nor bioplastics have been examined as a potential solution to desiccation cracking and their effectiveness is presented in this research. This is also the first study to compare these techniques at two different temperatures and to subject them to cyclic wetting and drying. Consequently, a comparative analysis of the mentioned improvement techniques' effectiveness has not been completed. A qualitative analysis was conducted by analyzing the geometric characteristics of cracking patterns in the plain and improved soil samples. The quantitative analysis was completed using an original code powered by MATLAB's image analysis software before performing image matrix operations in a Visual Basic for Applications (VBA) program. The utilized image analysis process is simple and inexpensive due to the widespread public familiarity and access of both VBA and MATLAB. A comparative analysis of the soil improvement techniques was completed using the area reduction factor (ARF), average crack width (w_{avg}) and maximum crack width (w_{max}) of the treated and non-treated cohesive soil samples.

2. Materials and Methods

2.1. Materials

2.1.1. Base Soil

The base soil material used for experimentation was residual Piedmont soil that had been sieved through the No. 40 sieve (0.425 mm). Piedmont soils have the reputation of not being particularly well categorized by the Unified Soil Classification System (USCS) [23]. The soil behaves almost as a hybrid soil type, exhibiting characteristics of the fine-grained silt in undrained conditions and the coarse-grained soil silty sand in drained conditions when loading is applied [23]. Figure 1 depicts the grain size distribution curve for the base soil. The soil was tested for its Atterberg Limits in accordance with ASTM D4318 [24] and the liquid limit and plasticity Index were determined to be 49 and 20, respectively. Therefore, according to the USCS, the fine particles are classified as silt with low plasticity. The overall classification of residual Piedmont soil that was used in this study was well-graded sand with silt (SW-SM).
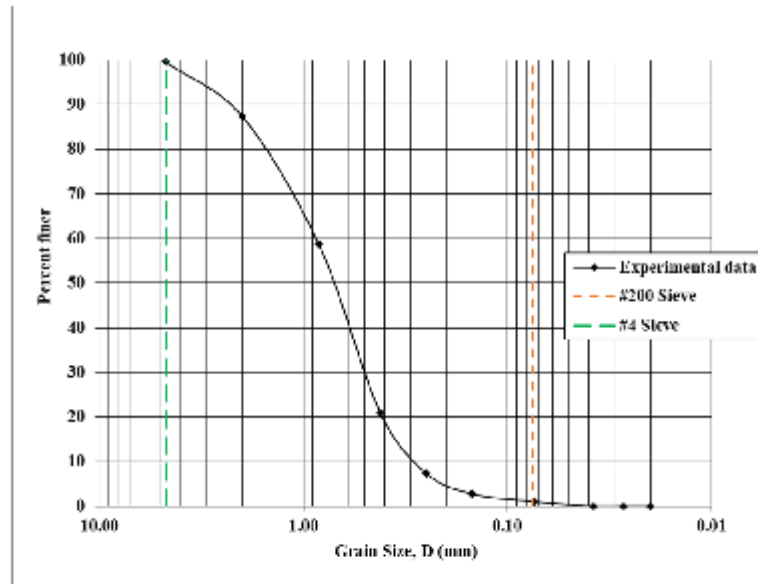
Figure 1. Grain size distribution curve of the base soil used in this study.

2.1.2. Soil Improvement Types

In this study, the three additives investigated as strengthening agents were fly ash, recycled polyester carpet fibers, and bioplastic, as well as a fly ash-fiber combination. The first tested improvement technique was Class C fly ash. This is the light weight waste produced by burning pulverized coal. It has cementitious qualities and is often used as an additive during the concrete mixing procedure. The fly ash addition was 15% based on the dry weight of the soil.

The next soil improvement technique was introducing recycled polyester carpet fibers to the soil samples. The polyester fibers were short straight fibers manufactured by Beaulieu of America, USA, and had a length of 50 mm and a diameter of 0.07 mm (aspect ratio of 714). The density of the polyester fibers was 1.38 g/cm³ (20 °C), and the volumetric fiber content was one per cent.

A combination of the Class C fly ash and the carpet fibers was also tested as an improvement technique. The base material and fly ash were mixed first, where the fly ash addition was 10% based on the dry weight of the soil. After the initial dry mixture was complete, polyester fiber was added until the sample contained 0.5% fibers by volume. All the addition rates of fly ash and carpet fibers were determined by a critical and extensive review of the existing literature, and preliminary laboratory mix design testing.

The final soil improvement technique analyzed was a gelatin-based bioplastic. The gelatin-based bioplastic concentration was 8%. To achieve this, for every 500 g of base material used, 44 g of water, 30 g of vinegar, 7.2 g of gelatin, and three grams of glycerin were mixed together. To prepare the gelatin-based bioplastic, the water was boiled on a hot plate, with the gelatin being slowly added to prevent clumping. The vinegar and glycerin were then subsequently slowly mixed into the final blend. After thoroughly mixing all of the components, bioplastic was added to the base material sample soil and mixed again, until the homogenous soil-bioplastic mixture was achieved.

2.2. Methods

2.2.1. Desiccation Test

The desiccation crack test was performed on improved and non-improved soil specimens. The purpose of the desiccation test was to study the cracking behavior of a soil sample as the sample reduces the moisture content and dehydrates. The samples were prepared by first mixing all the dry components (base soil, fly ash, fibers) together for a few minutes and then water was added to raise the water content to the desired level of 25%. The bioplastic-treated sample was prepared in the manner described in the materials section. Once thoroughly mixed, the soil specimens were manually placed into the cylindrically-shaped, lubricated stainless-steel molds and lightly smoothed to have a uniform clay thickness of 20 mm. The inner diameter of the mold was 230 mm.

In order to study the temperature effect on the desiccation crack cracking and soil-improvement type, two different types of desiccation tests were performed: standard and accelerated. During the standard test, the sample was allowed to dry at constant room temperature (20 °C) and humidity (80%) for 24 straight hours. Each soil sample was tested under the same conditions. The samples were consistently monitored for the first eight hours and then a final check was performed at the 24-h mark. For the accelerated test, the samples were heated in the oven at 105°C for two hours before rewetting the sample and completing the process for another two hours. Every fifteen minutes, the soil sample was carefully removed for image acquisition and then immediately replaced in the oven. After two hours, water was slowly poured over the sample until the initial water content was reached. The sample was then placed into the oven and allowed to dry for another two hours, with continued monitoring and image acquisition every 15 min.

2.2.2. Image Acquisition and Processing

The digital images of the soil samples were taken at fixed time increments using a stand held at a constant position for image consistency and uniformity. The camera was placed on a stand 46 cm tall that was fixed over the center of the clay sample. The image acquisition time frame increments were 15 and 120 min for the standard test and accelerated tests, respectively. For each image, the number of cracks in the specimen with a length of at least one centimeter was counted and recorded.

The digital image acquisition was followed by image processing to identify each constitutive component (cracks, fibers, and soil matrix) and, finally, a quantitative analysis of the crack geometric properties within the sample. In order to do so, the original MATLAB code was developed in this study. The image processing program consisted of six major steps to achieve the desired crack parameters.

The first step, image conversion, converted the original digital image (Figure 2a) first into a grayscale image and then further still into a binary image (Figure 2b). The second step was segmentation which isolated the clay surface and removed blemishes from the indentations in the clay surface (Figure 2c). The image was then given real dimensions by converting a known distance in the image to a pixel distance, giving the image data context. The surface area of each specimen was collected and the initial area ($Area_i$) for each specimen was stored and compared to each subsequent image. The change in the area at each stage ($\Delta Area$) in comparison with the initial area ($Area_i$) was used to determine the ARF:

$$ARF = \frac{\Delta Area}{Area_i} \tag{1}$$

To accurately analyze the crack parameters, the binary image of the crack needed to be isolated such that the desiccation crack was the only black portion of the image remaining (Figure 2d). This final image was analyzed using a VBA code to return values for the maximum crack width (w_{max}) and the average crack width (w_{avg}).

A-6
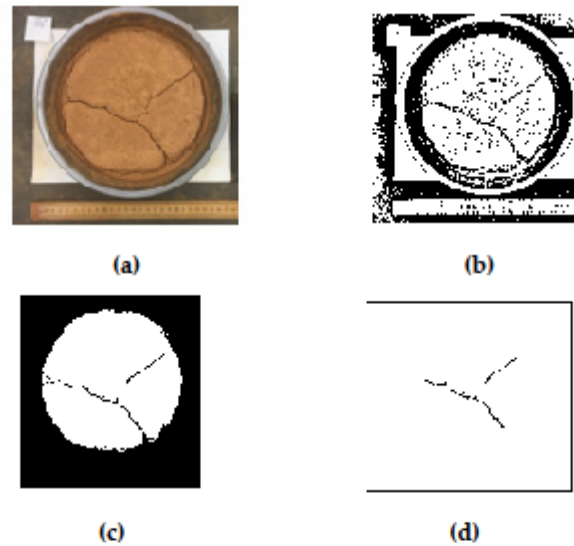
Figure 2. Image processing: (a) original sample photo; (b) original binary image; (c) clay surface binary image; (d) isolated crack binary image.

3. Results

Using the data obtained from the image analysis, the performance of each soil improvement technique was examined. The final crack count, w_{avg}, and w_{max} were recorded at each time frame during the accelerated desiccation test. In general, the cracks developed rapidly, with the samples often going from no cracks to a fully-realized crack network in one photocycle (15 min time frame). The development of the desiccation cracking throughout the first drying cycle of the accelerated test can be seen in Figure 3. The figure shows that the cracking pattern of the base soil sample propagated in a three-pronged, letter Y-like shape (Figures 3 and 4). However, the specimens with the ash and fibers sometimes deviated from this shape. Once the samples with the added fiber cracked in the second cycle, they took on a more circular manner like the letter C with smaller segments radiating out to the edges (Figure 5). This was most likely due to the transverse isotropic fiber distribution as a result of the clay mixing process. As the clay was mixed in a circular motion, many of the fibers became orientated in the same pattern. Consequentially, the cracks formed parallel to the fiber alignment because of the lack of reinforcement oriented perpendicular to the crack. The fly ash samples tended to have a more lopsided shape and propagated in a more clustered manner.

For the standard desiccation test, only the *ARF* results were recorded for each chronologic digital image due to crack propagation not occurring at room temperatures during the first eight hours of the testing process. The final crack count, w_{avg}, and w_{max} were recorded at the 24-hour mark.

The crack count was recorded in order to quantitatively analyze the crack network morphology. The results from the standard desiccation test can be seen in Figure 6. The figure shows that aside from adding the gelatin-based bioplastic, the soil additives did not materially affect the total number of crack segments after 24 h of drying at room temperature. Both samples that included fly ash developed an additional crack segment over the untreated soil.
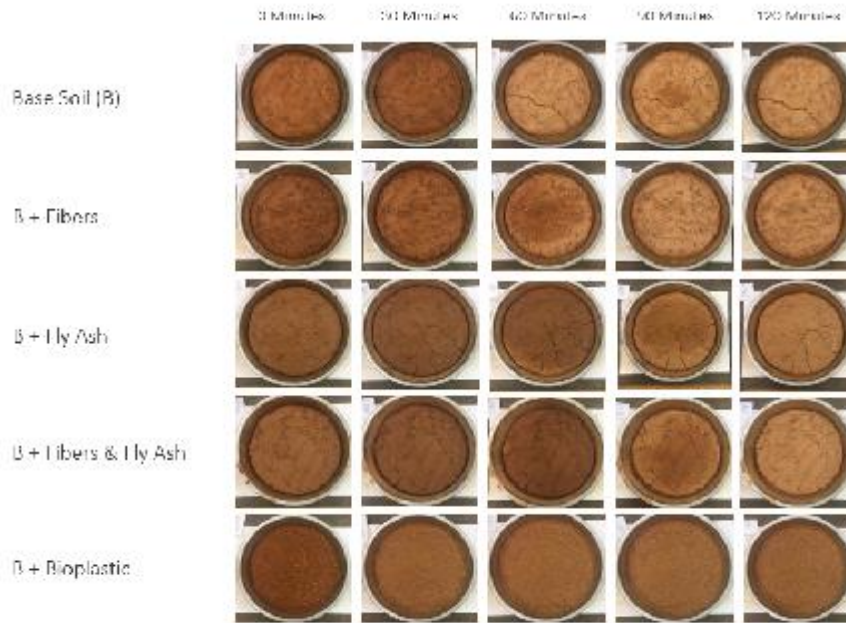
Figure 3. Desiccation crack test results for accelerated test after two hours of drying.

Figure 4. Desiccation crack test results for accelerated test for base soil.

Figure 5. Accelerated test final crack distribution for fiber-aided soil.

A-8
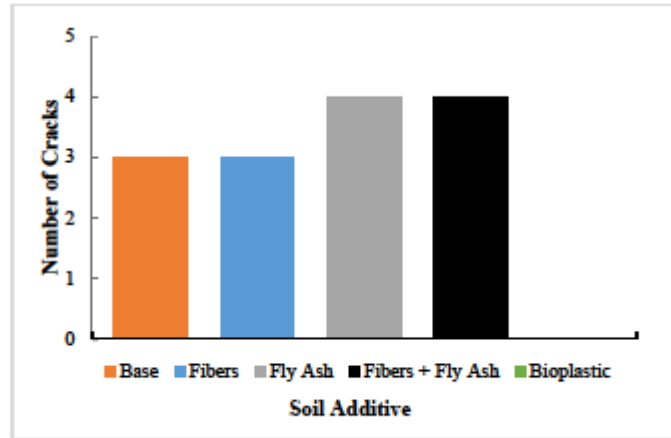
Figure 6. Number of cracks developed in standard desiccation test after 24 h at room temperature.

The crack count data for the accelerated desiccation test can be seen in Figure 7. The figure shows that in the first drying cycle (Figure 7a), no cracks developed in the samples mixed with the bioplastic and with the carpet fibers only. In the samples where cracks did develop, they generally appeared between the 15- and 30-min marks. After the rewetting process (Figure 7b), the bioplastic-improved soil sample was the only sample that did not develop any desiccation cracks. Each of the other additives developed more cracks than the base soil at the end of the second drying cycle. After rewetting, the timing of crack formation varied to a much greater degree with the plain soil cracking after 15 min, the fiber-aided soil cracking after 30 min, the fly ash sample developing cracks at the 45-minute mark, and the hybrid additive preventing cracking up until 75 min after rewetting occurred.
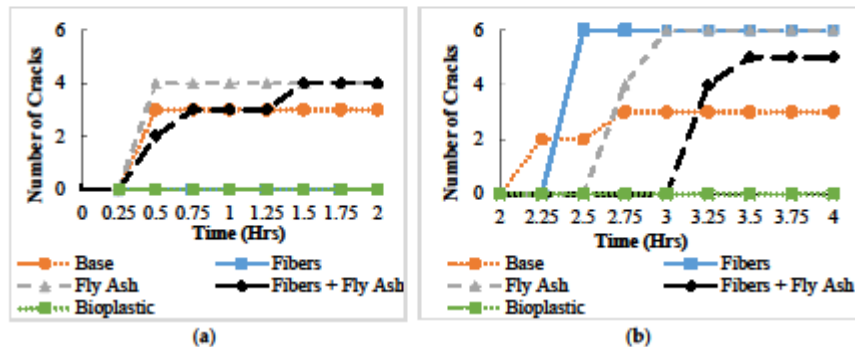
Figure 7. Development of the desiccation cracks in the accelerated test (a) first drying cycle; (b) second drying cycle.

The w_{avg} was calculated so that each soil improvement method's ability in solely reducing crack growth could be examined. The effect of the different soil improvement type on the w_{avg} for the standard desiccation test can be seen in Figure 8. The average crack width after 24 h for the base soil was found to be 1.59 mm. The sample with fly ash showed almost no improvement over the plain specimen. The samples improved with only carpet fibers and the carpet fibers-fly ash combination developed

cracks with smaller average widths of approximately 0.9 mm at the end of testing. The sample with the bioplastic had no average crack width as it did not develop cracks during the standard desiccation test.
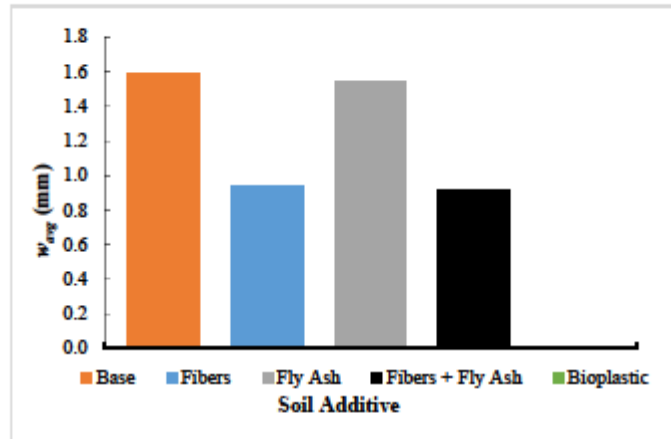
Figure 8. Average crack width of soils under standard desiccation test at 24-hour mark.

The effect of different soil improvement types on the w_{avg} for the accelerated desiccation test is depicted in Figure 9. The average crack width at the end of the wetting and drying process for the base soil was found to be 1.54 mm (Figure 9b). The samples with fly ash and carpet fibers showed almost no improvement in comparison with the non-treated soil. The samples with carpet fibers-fly ash combination developed cracks with smaller average widths at the termination point. The sample with the bioplastic did not develop cracks during the test and therefore had no average crack width. It is worth noting that the crack width after rewetting was assumed to be zero. Though some soil damage can be observed, the full depth cracks were not present at the time. In addition, in some time periods, the average crack width was shown to decrease. This was not due to the cracks shrinking, but as a result of the image processing software reading darker, wet spots in the soil near the cracks as parts of the actual crack. As the soil dried out more, the wet spots disappeared, causing the cracks to appear to be narrowing.

Figure 9. The effect of the soil improvement type on the development of the average crack width, w_{avg} in the accelerated test: (a) first drying cycle; (b) second drying cycle.

The effect of the different soil improvement types on the maximum crack width, w_{max} for the standard desiccation test can be seen in Figure 10. The reasons for finding the maximum crack width in each sample were twofold. First, the wider cracks have a greater potential to cause structural damage, meaning the maximum crack width represents the greatest potential for failure. Second, it provides context for the average crack results. For example, the fly ash sample possessed a w_{avg} similar to that of the untreated soil, however, the w_{max} of the fly ash was approximately 2 mm greater than the base soil. This suggests that the fly ash most likely had a segment with an abnormally large crack with the remainder of the cracks being narrower than the cracks in the base soil. The maximum crack width at the end of the test for the base soil was found to be 4.11 mm. The sample with fly ash developed a crack system with a wider maximum crack width than the base clay (6.32 mm). The samples with just carpet fibers and the carpet fibers plus fly ash developed cracks with significantly smaller maximum widths of approximately 2.08 mm and 2.38 mm, respectively, at the end of testing. Again, the sample treated with the gelatin-based bioplastic never cracked during the desiccation test.

Figure 10. The effect of different soil improvement types on the maximum crack width, w_{max} at the 24-h mark.

The maximum crack widths over both drying cycles for each soil improvement type are shown in Figure 11. Each of the additives reduced the maximum crack width at the end of the testing process in comparison to the base soil but to varying degrees. Again, the sample with the gelatin-based bioplastic exhibited no changes and no cracking occurred. The samples with each of the fly ash only and the recycled carpet fiber showed approximately the same level of maximum crack width reduction, while the sample with the combined additives provided further crack reduction. In the second cycle, the plain soil's maximum crack width exhibited the same soil drying phenomenon that affected the average crack width results and led to the appearance of crack narrowing.
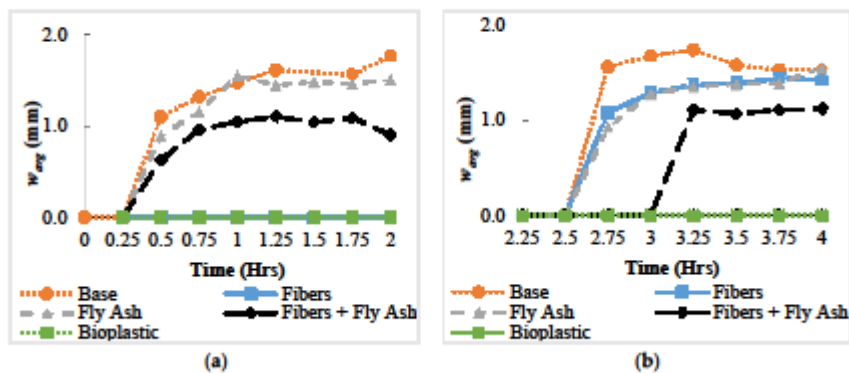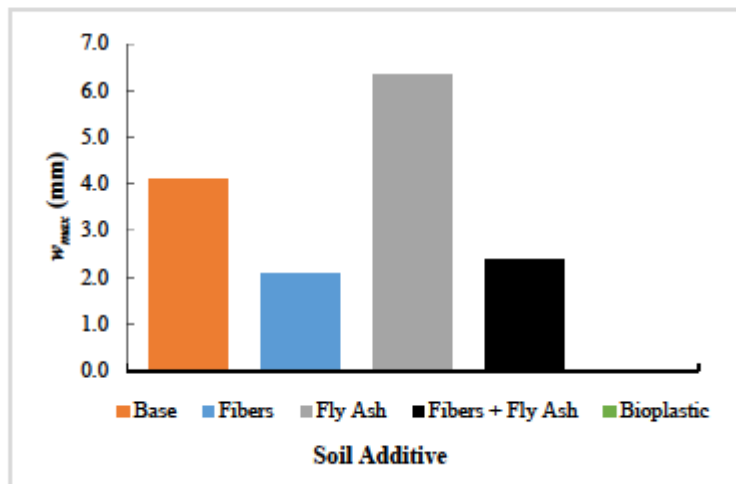
Figure 11. The effect of the soil improvement type on the development of the maximum crack width, w_{max} in the accelerated test: (a) first drying cycle; (b) second drying cycle.
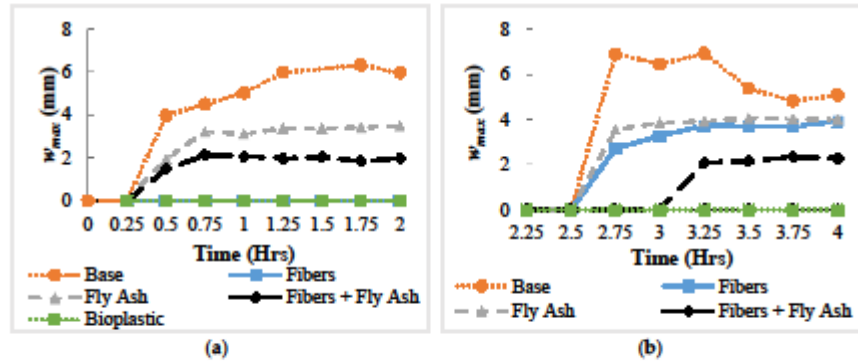
The *ARF* parameter was introduced to quantitatively measure the effectiveness of each soil improvement technique in reducing desiccation cracking as well as the overall soil shrinkage. The efficacy of the respective additives for the standard desiccation test can be seen in Figure 12. The figure shows that the base material exhibits the greatest *ARF* and the bioplastic exhibits virtually no shrinkage and did not crack after 24 h. Even though no cracks developed in any specimens until the 24-h mark, the samples still had *ARF* values due to lateral shrinkage of the samples before cracking. By analyzing the images, it was determined that the variations in the short-term were caused by discoloration in the clay surface as a result of uneven drying.
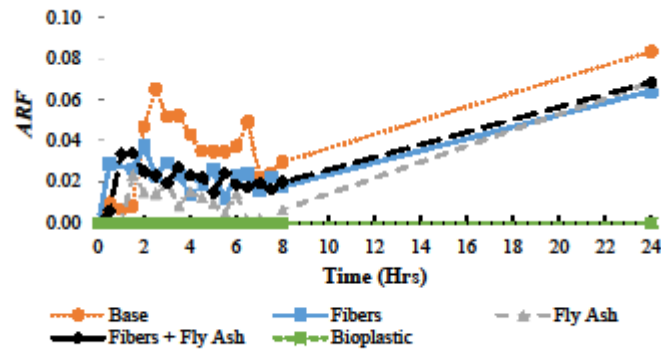
Figure 12. The effect of the different soil improvement type on the development of the *ARF* in the standard desiccation test.

For the accelerated desiccation test, the results from before and after the rewetting process were analyzed. The ARF data for both the initial drying cycle and the drying cycle after rewetting are displayed in Figure 13 a and b, respectively. The results showed that the samples including the fly ash provided little improvement when exposed to higher temperatures. Again, the sample mixed with the gelatin-based bioplastics showed no change in the surface area even when exposed to higher temperatures.
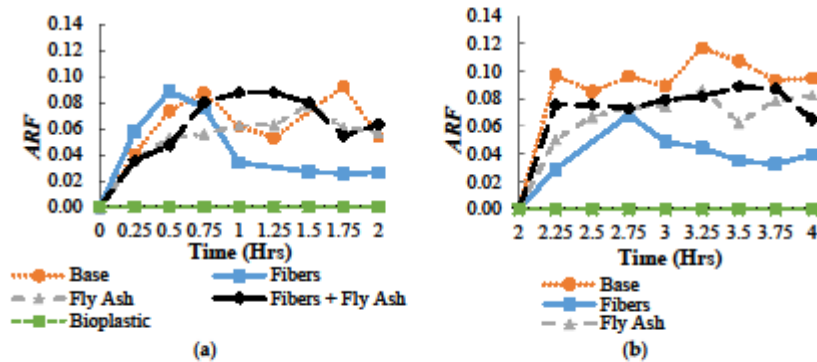
Figure 13. The effect of the soil improvement type on the *ARF* in the accelerated test: (a) first drying cycle; (b) second drying cycle.

4. Conclusions

The main aim of this research is the development of novel, eco-friendly soil improvement techniques and the investigation of their effect on the desiccation cracking behavior. In particular, three different sustainable soil improvement types were investigated, namely, fibers, bioplastics, and fly ash, along with a fly ash-fiber hybrid. The effect on the cohesive soils' crack resistance from the addition of a bioplastic and recycled carpet fibers were examined for the first time. In addition, the effectiveness of the techniques for crack resistance were examined at different temperatures and when subjected to cyclic wetting and drying for the first time.

A qualitative analysis was conducted by analyzing the geometric characteristics of the cracking patterns in the plain and sustainably improved soil samples. It was completed using an original code powered by MATLAB's image analysis software before performing image matrix operations in VBA program. MATLAB's image processing software proved to be a powerful tool in quantifying the 2D cracking behavior of the clay soils. By converting photos of the clay samples into representative matrices, each sample's crack geometry could be quickly and accurately attained. This is a vast improvement over the time consuming, expensive, and mostly inaccurate manual methods that have been employed to measure cracking behavior.

The *ARF* provided a comparative measurement that incorporated surface area change due to cracking as well as global shrinkage of the clay samples. The average crack width and maximum crack width data further described the crack geometry and each improvement techniques' effectiveness in reducing the scope of desiccation cracking. The bioplastic proved to be the most effective technique, completely preventing cracking and surface area reduction at room temperature, elevated temperatures and when subjected to a wetting and drying cycle. The fly ash treatment was able to reduce the width of the cracks when subjected to increased temperature but supplied little improvement over the untreated soil in terms of the total surface area reduction. Conversely, when dried slowly at room temperature, the same treatment technique yielded wider cracks than the base soil, but did show a 25% improvement in terms of *ARF*. The fiber-reinforced samples showed a sustained decrease in the crack size in each scenario, except for when the sample was being dried a second time after the rewetting process. At that point, the fiber-reinforced soil showed little improvement in minimizing the crack size, but still reduced *ARF* by 60%. The sample treated by the fiber-fly ash combination significantly decreased the size of cracks in all scenarios. However, this treatment showed little improvement over the base soil when subjected to a higher temperature with regards to the *ARF*. In addition, the combination fared worse than the soil treated solely by fibers. The behavior of the fly ash treated samples and the combined sample suggests that fly ash loses its effectiveness when subjected to higher temperatures.

A-13

The results included in this paper are part of a larger research project examining the viability of novel sustainable soil improvement techniques. Moving forward, more research into sustainable desiccation crack reduction is warranted. Based on the success in this investigation, other recycled fibers should be studied to determine their viability. Due to the bioplastic's overwhelming performance as a crack propagation reducer, biopolymers that behave similarly to the bioplastic, such as guar gum and xanthan gum, should be closely examined as potential solutions to desiccation cracking.

Author Contributions: Conceptualization, M.M. and M.Z.I.; methodology, M.Z.I.; software, M.Z.I.; validation, M.M. and M.Z.I.; writing—original draft preparation, M.Z.I.; writing—review and editing, M.M.; supervision, M.M.

References

1. Laloui, L.; Peron, H.; Hueckel, T.; Hu, L.B. Desiccation Cracking of Soil. *Eur. J. Environ. Civ. Eng.* **2009**, *13*, 869–888.
2. Chaduvula, U.; Viswanadham, B.; Kodikara, J. A study on desiccation cracking behavior of polyester fiber-reinforced expansive clay. *Appl. Clay Sci.* **2017**, *142*, 163–172. [CrossRef]
3. Peron, H.; Hueckel, T.; Laloui, L.; Hu, L.B. Fundamentals of desiccation cracking of fine-grained soils: Experimental characterisation and mechanisms identification. *Can. Geotech. J.* **2009**, *46*, 1177–1201. [CrossRef]
4. Sánchez, M.; Atique, A.; Kim, S.; Romero, E.; Zielinski, M. Exploring desiccation cracks in soils using a 2D profile laser device. *Acta Geotech.* **2013**, *8*, 583–596. [CrossRef]
5. Suits, L.D.; Sheahan, T.C.; Lakshmikantha, M.R.; Prat, P.C.; Ledesma, A. Image Analysis for the Quantification of a Developing Crack Network on a Drying Soil. *Geotech. Test. J.* **2009**, *32*, 102216. [CrossRef]
6. Arena, A.; Piane, C.D.; Sarout, J. A new computational approach to cracks quantification from 2D image analysis: Application to micro-cracks description in rocks. *Comput. Geosci.* **2014**, *66*, 106–120. [CrossRef]
7. Shokri, N.; Zhou, P.; Keshmiri, A. Patterns of Desiccation Cracks in Saline Bentonite Layers. *Transp. Porous Media* **2015**, *110*, 333–344. [CrossRef]
8. Zielinski, M.; Sánchez, M.; Romero, E.; Atique, A. Precise observation of soil surface curling. *Geoderma* **2014**, *226*, 85–93. [CrossRef]
9. Shah, M.; Pandya, H.; Shukla, A. Influence of Chemical Additives on Shrinkage and Swelling Characteristics of Bentonite Clay. *Procedia Eng.* **2017**, *189*, 932–937. [CrossRef]
10. Jayanthi, P.N.V.; Singh, D.N. Utilization of Sustainable Materials for Soil Stabilization: State-of-the-Art. *Adv. Civ. Eng. Mater.* **2016**, *5*, 20150013. [CrossRef]
11. Consoli, N.C.; Marin, E.J.B.; Samaniego, R.A.Q.; Heineck, K.S.; Johann, A.D.R. Use of Sustainable Binders in Soil Stabilization. *J. Mater. Civ. Eng.* **2019**, *31*, 06018023. [CrossRef]
12. Wei, H.; Li, Q.; Han, L.; Han, S.; Wang, F.; Zhang, Y.; Chen, Z. Experimental Research on Deformation Characteristics of Using Silty Clay Modified Oil Shale Ash and Fly Ash as the Subgrade Material after Freeze-Thaw Cycles. *Sustainability* **2019**, *11*, 5141. [CrossRef]
13. Kamon, M.; Nontananandh, S. Combining Industrial Wastes with Lime for Soil Stabilization. *J. Geotech. Eng.* **1991**, *117*, 1–17. [CrossRef]
14. Wild, S.; Kinuthia, J.M.; Robinson, R.B.; Humphreys, I. Effects of ground granulated blast furnace slag (GGBS) on the strength and swelling properties of lime-stabilized kaolinite in the presence of sulphates. *Clay Miner.* **1996**, *31*, 423–433. [CrossRef]
15. Kalkan, E. Influence of silica fume on the desiccation cracks of compacted clayey soils. *Appl. Clay Sci.* **2009**, *43*, 296–302. [CrossRef]
16. Zumrawi, M.M.E.; Mahjoub, A.M.M.; Alnour, I.M. Effect of Some Chloride Salts on Swelling Properties of Expansive Soil. *Univ. Khartoum Eng. J.* **2016**, *6*, 35–41.
17. Mirzababaei, M.; Miraftab, M.; Mohamed, M.; McMahon, P. Impact of Carpet Waste Fibre Addition on Swelling Properties of Compacted Clays. *Geotech. Geol. Eng.* **2012**, *31*, 173–182. [CrossRef]

18. Ghiassian, H.; Poorebrahim, G.; Gray, D.H. Soil reinforcement with recycled carpet wastes. *Waste Manag. Res.* **2004**, *22*, 108–114. [CrossRef]

19. Shahnazari, H.; Ghiassian, H.; Noorzad, A.; Shafiee, A.; Tabarsa, A.R.; Jamshidi, R. Shear modulus of silty sand reinforced by carpet waste strips. *J. Seismol. Earthq. Eng.* **2009**, *11*, 133–142.

20. Chaduvula, U.; Manogaran, L.; Viswanadham, B.V.S.; Kodikara, J. Some Studies on Desiccation Cracking of Fiber-Reinforced Expansive Clay Subjected to Drying and Wetting Cycles. *PanAm Unsaturated Soils 2017* **2018**, *GSP 303*, 361–370.

21. Pastor, J.L.; Tomás, R.; Cano, M.; Riquelme, A.; Gutiérrez, E. Evaluation of the Improvement Effect of Limestone Powder Waste in the Stabilization of Swelling Clayey Soil. *Sustainability* **2019**, *11*, 679. [CrossRef]

22. Hidalgo, C.; Carvajal, G.; Muñoz, F. Laboratory Evaluation of Finely Milled Brick Debris as a Soil Stabilizer. *Sustainability* **2019**, *11*, 967. [CrossRef]

23. Mayne, P.W.; Brown, D.; Vinson, J.; Schneider, J.A.; Finke, K.A. Site Characterization of Piedmont Residual Soils at the NGES, Opelika, Alabama. *Natl. Geotech. Exp. Sites* **2000**, *GSP 93*, 160–185.

24. *ASTM D4318-00 Standard Test Methods for Liquid Limit, Plastic Limit, and Plasticity Index of Soils*; Annual Book of ASTM Standards, ASTM International: West Conshohocken, PA, USA, 2003; pp. 482–593.

APPENDIX B - MATLAB CODES

B.1 HYDRAULIC MODEL

```
m = 31;
p=m-1;
L = 3; % [cm]
qa = -.0925; % [cm/h] From Flux Calcs
hb = -0.0001; % [cm] From Measured Values
dz = L/p; % space increment [cm]
dt = 1.0/12; % time increment [h]
endtime = 6; % [h]
% Assign initial values for pressure head and water content
h = hb*ones(m,1);
thetainit = Reten(h);
% Vector of times at which pressure heads will be saved. The elements of
% "times" must be multiples of dt.
times = (1/12)*(0:72);
% Preallocate column vectors for h* and the coefficients a-sub-i, b-sub-i
hstar = NaN(m,1);
a = NaN(m,1);
b = NaN(m,1);
% Preallocate matrices for saving results at the times in "times"
headresults = NaN(m,length(times));
thetaresults = NaN(m,length(times));
masserr = NaN(1,length(times));
% Create square matrix A and column vector B with zero entries
A = zeros(m);
B = zeros(m,1);
z = dz*(1:m)'-dz/2; % Column vector of depths
t = 0; % Set time for first pass through while loop
M = 1; % Initialize counter
fluxsum = 0; % Initialize variable used for summing flux at z=L
% Begin stepping in time
while (t-endtime) <= sqrt(eps)
for j = 1:2
if j==1
% Create vectors of K and C values for first step
K = Cond(h);
C = SpecCap(h);
else
% Create vectors of K and C values for second step
K = 0.5*(Cond(h)+ Cond(hstar));
C = 0.5*(SpecCap(h)+ SpecCap(hstar));
end
% Calculate coefficients a-sub-i and b-sub-i
a(2:m) = dt*(K(1:m-1) + K(2:m))./(2*dz^2*C(2:m));
b(1:m-1) = dt*(K(1:m-1) + K(2:m))./(2*dz^2*C(1:m-1));
b(m) = dt*K(m)/(dz^2*C(m));
% Solve system of m linear equations
A(1,1) = 2 + b(1);
A(1,2) = -b(1);
B(1) = (2-b(1))*h(1) + b(1)*h(2) - 2*dz*b(1) + 2*dt*qa/(dz*C(1));
for i = 2:m-1
A(i,i-1) = -a(i);
A(i,i) = 2 + a(i) + b(i);
A(i,i+1) = -b(i);
```

```matlab
B(i) = (2-a(i)- b(i))*h(i) + a(i)*h(i-1) + b(i)*h(i+1)...
+ 2*dz*(a(i)-b(i));
end
A(m,m-1) = -a(m);
A(m,m) = 2 + a(m);
B(m) = (2-a(m))*h(m) + a(m)*h(m-1) + 2*dz*(a(m)-b(m));
if j==1
hstar = A\B;
else
h = A\B;
end
end
% Summation for calculation of mass balance error
fluxsum = fluxsum + K(m);
% Commands executed at times specified in the vector "times"
if any(abs(times-t) <= sqrt(eps))
% Write h and theta results to "headresults" and "thetaresults"
headresults(:,M) = h;
thetaresults(:,M) = Reten(h);
% Mass balance calculations
calcmass = dz*(sum(thetainit-thetaresults(:,M)));
truemass = dt*fluxsum - qa*t;
masserr(M) = 100*abs((truemass-calcmass)/truemass);
M = M + 1; % Increment counter
end
t = t + dt; % Increment time for next pass through while loop
end
thetaresults=thetaresults/1.3;%convert to gravimetric water content
```

B.1.1 HYDRAULIC CONDUCTIVITY SUBMODEL
```matlab
function Result = Cond(h)
% Function for calculating a vector of hydraulic conducitivities [cm/hr]
% from a vector of pressure heads [cm]. The conductivity function is from
% Eq. [9] of van Genuchten (1980).
Ksat = (10^-5)*3600; % [cm/hr]
alpha = 0.008478; % [1/cm]
ThetaSat = 0.77;
ThetaRes = 0;
n = 1.422686;
m = 1 - 1/n;
ah = abs(alpha*h);
Result = Ksat * (1 - ah.^(n-1).*(1+ah.^n).^(-m)).^2./(1+ah.^n).^(m/2);
```

B.1.2 WATER CONTENT SUBMODEL
```matlab
function Result = Reten(h)
%m = 1 - 1/n;
alpha = 0.008478; % [1/cm]
ThetaSat = 0.77;
ThetaRes = 0;
n = 1.422686;
m = 1 - 1/n;
Result = ThetaRes + (ThetaSat-ThetaRes)./(1 + abs(alpha*h).^n).^m;
```


B.1.3 SPECIFIC WATER CAPACITY SUBMODEL
```matlab
function Result = SpecCap(h)
```

```
% Function for calculating a vector of specific water capacities [1/cm]
% from a vector of pressure heads [cm]. The specific capacity function was
% obtained by differentiating the water retention function in Eq. [2] and
% [3] of van Genuchten (1980).
alpha = 0.008478; % [1/cm]
ThetaSat = 0.77;
ThetaRes = 0;
n = 1.422686;
m = 1 - 1/n;
ah = abs(alpha*h);
Result = n*m*alpha*( ThetaSat-ThetaRes)*ah.^(n-1)./(1 + ah.^n).^(m+1);
```

B.2 UNTREATED SOIL MECHANICAL MODEL

```
w=thetaresults;%Create Water Content Matrix
r0=85; %Total radius in mm
rit=r0+1;
v=.3; %Poisson Ratio
n=numel(times);%Set number of water content values
h0 = L*10+1; % depth in mm
EdgeBreaktime=0;
CrackBreaktime=0;
d = 30; %sample depth in mm
wcrit=0;
wedge=0;
alpha = .1774; % hydric constant
for i = 1:n %Time Iterations
    for r = 1:rit %Radius Iterations
        for h = 1:h0 %Depth Iterations
            sigma_t(h,i)=1000*165.28*exp(-8.6*w(h,i)); % Tensile Strength of
Soil
            tau(h,i)=1000*(3.15+(-2.85/(1+(.062*(100*w(h,i))^7.5)))); % Shear
strength of Soil
            Adhesion(h,i)=tau(h,i)*0.25;% Clay-Mold Wall Adhesion
            wi=w(30,1);
            E(h,i) = 30000000*(10^6) * ((100*w(h,i))^-5.26);%Young's Modulus
Calculations (Pa)
            if i == 1
                e_shrink(h,i) = 0;
            else
                e_shrink(h,i) = alpha *( wi-w(h,i)); % Shrinkage Strain
Calculation
            end
            sigma_r(h,r,i) = abs((E(h,i)/(1-v))*e_shrink(h,i)); %radial
stress Calculation (Pa)
            if sigma_r(h,r,i) > Adhesion(h,i) % Check wall Crack
                if EdgeBreaktime == 0
                    EdgeBreaktime=(i-1)*5
                    ei=i;
                end
                if wedge==0
                    wedge= w(h,i)
                    sedge=suction(i)
                end
                sigma_r(h,r,i) = tau(h,i)*(2+v)*((r0)-((r-1)))/(3*d); %radial
stress Calculation (Pa)
```

```
                sigma_theta(h,r,i) = (tau(h,i) * (((2+v)*(r0))- ((1+ v)*((r-
1)))))/(3*d); %Angular stress Calculation (Pa)
                Ur(h,r,i) = min(0, ((sigma_theta(h,r,i)*((r-1))*(1-
v)/(E(h,i)))-((r-1)*e_shrink(h,i))));% Displacement in mm Calculation
            else
                sigma_theta(h,r,i)=sigma_r(h,r,i); %Angular stress
Calculation (Pa)
                Ur(h,r,i)=0;% Displacement Calculation (mm)
            end
            if sigma_theta(h,r,i)> sigma_t(h,i) % Check if Cracking Occurs
                if wcrit==0
                    wcrit= w(h,i)
                    scrit=suction(i)
                end
                if CrackBreaktime == 0
                    CrackBreaktime=(i-1)*5
                    ci=i;
                end
                Depth = h-1;
            end
        end
    end
end
```

B.3 0.5% FIBER MECHANICAL MODEL

```
w=thetaresults;%Create Water Content Matrix
r0=85; %Total radius in mm
rit=r0+1;
v=.3; %Poisson Ratio
n=numel(times);%Set number of water content values
h0 = L*10+1; % depth in mm
EdgeBreaktime=0;
CrackBreaktime=0;
d = 30; %sample depth in mm
wcrit=0;
wedge=0;
alpha = .1934; % hydric constant
Fiber_Content=.5;
for i = 1:n %Time Iterations
    for r = 1:rit %Radius Iterations
        for h = 1:h0 %Depth Iterations
            sigma_t(h,i)=1000*165.28*exp(-8.6*w(h,i)); % Tensile Strength of
Soil
            sigma_t(h,i)=Fiber_Content*1632+sigma_t(h,i);
            tau(h,i)=1000*(3.15+(-2.85/(1+(.062*(100*w(h,i))^7.5)))); % Shear
strength of Soil
            Adhesion(h,i)=tau(h,i)*0.25;% Clay-Mold Wall Adhesion
            wi=w(30,1);
            E(h,i) = 30000000*(10^6) * ((100*w(h,i))^-5.26); %Young's Modulus
Calculations (Pa)
            if i == 1
                e_shrink(h,i) = 0;
            else
                e_shrink(h,i) = alpha *( wi-w(h,i)); % Shrinkage Strain
Calculation
            end
```

```
                sigma_r(h,r,i) = abs((E(h,i)/(1-v))*e_shrink(h,i)); %radial
stress Calculation (Pa)
            if sigma_r(h,r,i) > Adhesion(h,i) % Check wall Crack
                if EdgeBreaktime == 0
                    EdgeBreaktime=(i-1)*5
                    ei=i;
                end
                if wedge==0
                    wedge= w(h,i)
                    sedge=suction(i)
                end
                sigma_r(h,r,i) = tau(h,i)*(2+v)*((r0)-((r-1)))/(3*d); %radial
stress Calculation (Pa)
                sigma_theta(h,r,i) = (tau(h,i) * (((2+v)*(r0))- ((1+ v)*((r-
1))))))/(3*d); %Angular stress Calculation (Pa)
                Ur(h,r,i) = min(0, ((sigma_theta(h,r,i)*((r-1))*(1-
v)/(E(h,i)))-((r-1)*e_shrink(h,i))));% Displacement in mm Calculation
            else
                sigma_theta(h,r,i)=sigma_r(h,r,i); %Angular stress
Calculation (Pa)
                Ur(h,r,i)=0;% Displacement Calculation (mm)
            end
            if sigma_theta(h,r,i)> sigma_t(h,i) % Check if Cracking Occurs
                if wcrit==0
                    wcrit= w(h,i)
                    scrit=suction(i)
                end
                if CrackBreaktime == 0
                    CrackBreaktime=(i-1)*5
                    ci=i;
                end
                Depth = h;
            end
        end
    end
end
```

B.4 2% FIBER SOIL MECHANICAL MODEL

```
w=thetaresults;%Create Water Content Matrix
r0=85; %Total radius in mm
rit=r0+1;
v=.3; %Poisson Ratio
n=numel(times);%Set number of water content values
h0 = L*10+1; % depth in mm
EdgeBreaktime=0;
CrackBreaktime=0;
d = 30; %sample depth in mm
wcrit=0;
wedge=0;
Fiber_Content=.5;
alpha = .2665; % hydric constant
for i = 1:n %Time Iterations
    for r = 1:rit %Radius Iterations
        for h = 1:h0 %Depth Iterations
            sigma_t(h,i)=1000*4446*exp(-8.6*w(h,i)); % Tensile Strength of
Soil
```

```matlab
            sigma_t(h,i)=Fiber_Content*1*1632+sigma_t(h,i);
            tau(h,i)=1000*(3.15+(-2.85/(1+(.062*(100*w(h,i))^7.5)))); % Shear
strength of Soil
            Adhesion(h,i)=tau(h,i)*0.25; % Clay-Mold Wall Adhesion
            wi=w(30,1);
            E(h,i) = 30000000*(10^6) * ((100*w(h,i))^-5.26); %Young's Modulus
Calculations (Pa)
            if i == 1
                e_shrink(h,i) = 0;
            else
                e_shrink(h,i) = alpha *( wi-w(h,i)); % Shrinkage Strain
Calculation
            end
            sigma_r(h,r,i) = abs((E(h,i)/(1-v))*e_shrink(h,i)); %radial
stress Calculation (Pa)
            if sigma_r(h,r,i) > Adhesion(h,i) % Check wall Crack
                if EdgeBreaktime == 0
                    EdgeBreaktime=(i-1)*5
                    ei=i;
                end
                if wedge==0
                    wedge= w(h,i)
                    sedge=suction(i)
                end
                sigma_r(h,r,i) = tau(h,i)*(2+v)*((r0)-((r-1)))/(3*d); %radial
stress Calculation (Pa)
                sigma_theta(h,r,i) = (tau(h,i) * (((2+v)*(r0))- ((1+ v)*((r-
1))))))/(3*d); %Angular stress Calculation (Pa)
                Ur(h,r,i) = min(0, ((sigma_theta(h,r,i)*((r-1))*(1-
v)/(E(h,i)))-((r-1)*e_shrink(h,i)))); % Displacement in mm Calculation
            else
                sigma_theta(h,r,i)=sigma_r(h,r,i); %Angular stress
Calculation (Pa)
                Ur(h,r,i)=0; % Displacement Calculation (mm)
            end
            if sigma_theta(h,r,i)> sigma_t(h,i) % Check if Cracking Occurs
                if wcrit==0
                    wcrit= w(h,i)
                    scrit=suction(i)
                end
                if CrackBreaktime == 0
                    CrackBreaktime=(i-1)*5
                    ci=i;
                end
            end
        end
    end
end
```

B.5 XANTHAN GUM SOIL MECHANICAL MODEL

```matlab
w=thetaresults; %Create Water Content Matrix
r0=85; %Total radius in mm
rit=r0+1;
v=.3; %Poisson Ratio
n=numel(times); %Set number of water content values
h0 = L*10+1; % depth in mm
```

```
EdgeBreaktime=0;
CrackBreaktime=0;
d = 30; %sample depth in mm
wcrit=0;
wedge=0;
alpha = .1774; % hydric constant
for i = 1:n %Time Iterations
    for r = 1:rit %Radius Iterations
        for h = 1:h0 %Depth Iterations
            sigma_t(h,i)=1000*347.84*exp(-8.6*w(h,i)); % Tensile Strength of
Soil
            tau(h,i)=20000*(3.15+(-2.85/(1+(.062*((100*w(h,i))^7.5))))));%
Shear strength of Soil
            Adhesion(h,i)=tau(h,i)*20;% Clay-Mold Wall Adhesion
            wi=w(30,1);
            E(h,i) = 56880000*(10^6) * ((100*w(h,i))^-5.26);%Young's Modulus
Calculations (Pa)
            if i == 1
                e_shrink(h,i) = 0;
            else
                e_shrink(h,i) = alpha *( wi-w(h,i)); % Shrinkage Strain
Calculation
            end
            sigma_r(h,r,i) = abs((E(h,i)/(1-v))*e_shrink(h,i)); %radial
stress Calculation (Pa)
            if sigma_r(h,r,i) > Adhesion(h,i) % Check wall Crack
                if EdgeBreaktime == 0
                    EdgeBreaktime=(i-1)*5
                    ei=i;
                end
                if wedge==0
                    wedge= w(h,i)
                    sedge=suction(i)
                end
                sigma_r(h,r,i) = tau(h,i)*(2+v)*((r0)-((r-1)))/(3*d); %radial
stress Calculation (Pa)
                sigma_theta(h,r,i) = (tau(h,i) * (((2+v)*(r0))- ((1+ v)*((r-
1))))))/(3*d); %Angular stress Calculation (Pa)
                Ur(h,r,i) = min(0, ((sigma_theta(h,r,i)*((r-1))*(1-
v)/(E(h,i)))-((r-1)*e_shrink(h,i))));% Displacement in mm Calculation
            else
                sigma_theta(h,r,i)=sigma_r(h,r,i); %Angular stress
Calculation (Pa)
                Ur(h,r,i)=0;% Displacement Calculation (mm)
            end
            if sigma_theta(h,r,i)> sigma_t(h,i) % Check if Cracking Occurs
                if wcrit==0
                    wcrit= w(h,i)
                    scrit=suction(i)
                end
                if CrackBreaktime == 0
                    CrackBreaktime=(i-1)*5
                    ci=i;
                end
                Depth = h;
            end
        end
    end
```

```
        end
    end
```

APPENDIX C – DETAILED HYDRAULIC MODELING

$$(2 + b_1^*)h_1^* - b_1^* h_2^* = (2 - b_1^*)h_1^n + b_1^* h_2^n - 2\Delta z b_1^* + \left(\frac{2\Delta t q_a}{\Delta z C_1^n}\right)$$

Equation C-1

$$-a_i^* h_{i-1}^* + (2 + b_i^* + a_i^*)h_i^* - b_i^* h_{i+1}^* = (2 - a_i^* - b_i^*)h_i^n + a_i^* h_{i-1}^n + b_i^* h_{i+1}^n - 2\Delta z(a_i^* - b_i^*)$$

$$i = 2,3, \ldots, m-1$$

Equation C-2

$$-a_i^* h_{m-1}^* + (2 + a_m^*)h_m^* = (2 - a_m^*)h_m^n + a_m^* h_{m-1}^n + 2\Delta z(a_m^* - b_m^*)$$

Equation C-3

$$(2 + b_1^{n+1})h_1^{n+1} - b_1^{n+1}h_2^{n+1} = (2 - b_1^{n+1})h_1^n + b_1^{n+1}h_2^n - 2\Delta z b_1^{n+1} + \left(\frac{2\Delta t q_a}{\Delta z C_1^{n+\frac{1}{2}}}\right)$$

<div align="right">Equation C-4</div>

$$-a_i^{n+1}h_{i-1}^{n+1} + (2 + b_i^{n+1} + a_i^{n+1})h_i^{n+1} - b_i^{n+1}h_{i+1}^{n+1}$$

$$= (2 - a_i^{n+1} - b_i^{n+1})h_i^n + a_i^{n+1}h_{i-1}^n + b_i^{n+1}h_{i+1}^n - 2\Delta z(a_i^{n+1} - b_i^{n+1})$$

$$i = 2,3, \dots, m - 1$$

<div align="right">Equation C-5</div>

$$-a_i^{n+1}h_{m-1}^{n+1} + (2 + a_m^{n+1})h_m^{n+1} = (2 - a_m^{n+1})h_m^n + a_m^{n+1}h_{m-1}^n + 2\Delta z(a_m^{n+1} - b_m^{n+1})$$

<div align="right">Equation C-6</div>

$$a_i^* = \frac{\Delta t(K_{i-1}^n + K_i^n)}{2(\Delta z)^2 C_i^n}; b_i^* = \frac{\Delta t(K_i^n + K_{i+1}^n)}{2(\Delta z)^2 C_i^n}$$

<div align="right">Equation C-7</div>

$$a_i^* = \frac{\Delta t(K_{i-1}^n + K_i^n)}{2(\Delta z)^2 C_i^n} ; i = 2,3, \dots, m$$

<div align="right">Equation C-8</div>

$$b_i^* = \frac{\Delta t(K_i^n + K_{i+1}^n)}{2(\Delta z)^2 C_i^n} ; i = 1,2, \dots, m-1$$

<div align="right">Equation C-9</div>

$$b_m^* = \frac{\Delta t(K_m^n)}{2(\Delta z)^2 C_m^n} ;$$

<div align="right">Equation C-10</div>

$$a_i^{n+1} = \frac{\Delta t(K_{i-1}^{n+\frac{1}{2}} + K_i^{n+\frac{1}{2}})}{2(\Delta z)^2 C_i^{n+\frac{1}{2}}} ; i = 2,3, \dots, m$$

<div align="right">Equation C-11</div>

$$b_i^{n+1} = \frac{\Delta t(K_i^{n+\frac{1}{2}} + K_{i+1}^{n+\frac{1}{2}})}{2(\Delta z)^2 C_i^{n+\frac{1}{2}}} ; i = 1,2, \dots, m-1$$

<div align="right">Equation C-12</div>

$$b_m^{n+1} = \frac{\Delta t (K_m^{n+\frac{1}{2}})}{2(\Delta z)^2 C_m^{n+\frac{1}{2}}}$$

Equation C-13

$$K_i^{n+\frac{1}{2}} = \frac{K_i^n + K_i^*}{2} ; C_i^{n+\frac{1}{2}} = \frac{C_i^n + C_i^*}{2}$$

Equation C-14